

# Zwitterionic Dendrimersomes: A Closer Xenobiotic Mimic of Cell Membranes

Anton Joseph, Anna M. Wagner, Manuela Garay-Sarmiento, Mina Aleksanyan, Tamás Haraszti, Dominik Söder, Vasil N. Georgiev, Rumiana Dimova, Virgil Percec, and Cesar Rodriguez-Emmenegger\*

Building functional mimics of cell membranes is an important task toward the development of synthetic cells. So far, lipid and amphiphilic block copolymers are the most widely used amphiphiles with the bilayers by the former lacking stability while membranes by the latter are typically characterized by very slow dynamics. Herein, a new type of Janus dendrimer containing a zwitterionic phosphocholine hydrophilic headgroup (JD<sup>PC</sup>) and a 3,5-substituted dihydrobenzoate-based hydrophobic dendron is introduced. JD<sup>PC</sup> self-assembles in water into zwitterionic dendrimersomes (z-DSs) that faithfully recapitulate the cell membrane in thickness, flexibility, and fluidity, while being resilient to harsh conditions and displaying faster pore closing dynamics in the event of membrane rupture. This enables the fabrication of hybrid DSs with components of natural membranes, including pore-forming peptides, structure-directing lipids, and glycans to create raft-like domains or onion vesicles. Moreover, z-DSs can be used to create active synthetic cells with life-like features that mimic vesicle fusion and motility as well as environmental sensing. Despite their fully synthetic nature, z-DSs are minimal cell mimics that can integrate and interact with living matter with the programmability to imitate life-like features and beyond.

## 1. Introduction

The goal of bottom-up synthetic biology is to design and build a fully synthetic protocell. This endeavor promises to produce minimal systems to probe biological questions, shed light on the origin of life and enable new biotechnologies beyond the limits of nature. Without the complexity and redundancies that are present in natural cells, these synthetic systems offer a more predictable and efficient mean.<sup>[1]</sup>

Arguably, one of the most important components of a cell is its membrane. In nature, the main structural components of cell membranes are phospholipids. They consist of a zwitterionic phosphocholine (PC) head group and a variety of saturated or partially unsaturated carbon chains as tails which are connected to a glycerol core. The phospholipids act as a matrix into which a substantial number of other types of lipids, cholesterol, proteins, and carbohydrates are embedded.<sup>[2]</sup>

A. Joseph, A. M. Wagner, M. Garay-Sarmiento, T. Haraszti, D. Söder, C. Rodriguez-Emmenegger  
DWI – Leibniz Institute for Interactive Materials  
Forckenbeckstraße 50, 52074 Aachen, Germany  
E-mail: rodriguez@dwI.rwth-aachen.de

A. Joseph, A. M. Wagner, T. Haraszti, D. Söder  
Institute of Technical and Macromolecular Chemistry  
RWTH Aachen University  
Worringerweg 2, 52074 Aachen, Germany

M. Garay-Sarmiento  
Chair of Biotechnology  
RWTH Aachen University  
Worringerweg 3, 52074 Aachen, Germany

M. Aleksanyan  
Institute for Chemistry and Biochemistry  
Freie Universität Berlin  
Takustraße 3, 14195 Berlin, Germany

M. Aleksanyan, V. N. Georgiev, R. Dimova  
Max Planck Institute of Colloids and Interfaces  
Science Park Golm  
14476 Potsdam, Germany

V. Percec  
Roy & Diana Vagelos Laboratories  
Department of Chemistry  
University of Pennsylvania  
Philadelphia, PA 19104323, USA

C. Rodriguez-Emmenegger  
Bioinspired Interactive Materials and Protocellular Systems  
Institute for Bioengineering of Catalonia (IBEC)  
The Barcelona Institute of Science and Technology (BIST)  
Carrer de Baldiri Reixac 10–12, 08028 Barcelona, Spain  
E-mail: crodriguez@ibecbarcelona.eu

C. Rodriguez-Emmenegger  
Institució Catalana de Recerca i Estudis Avançats (ICREA)  
Passeig Lluís Companys 23, 08028 Barcelona, Spain

 The ORCID identification number(s) for the author(s) of this article can be found under <https://doi.org/10.1002/adma.202206288>.

© 2022 The Authors. Advanced Materials published by Wiley-VCH GmbH. This is an open access article under the terms of the Creative Commons Attribution-NonCommercial License, which permits use, distribution and reproduction in any medium, provided the original work is properly cited and is not used for commercial purposes.

DOI: 10.1002/adma.202206288

The synergistic behavior of these components provides sites for reactions at the membrane surface and endows the cell with its numerous functions, such as sensing the environment, motion, or establishment of chemical potential differences for the maintenance of the out-of-equilibrium system that is life.<sup>[3]</sup>

Such advanced functions may be in reach by integrating natural receptors and functional molecules into synthetic biomembranes which faithfully mimic their native environment. First, their thickness must match one of natural membranes (4–6 nm) to allow for seamless integration of natural functional building blocks into the membrane.<sup>[4]</sup> These embedded functionalities must be able to rapidly diffuse and organize laterally inside the membrane to give rise to a multitude of multivalent interactions.<sup>[2a,5]</sup> This demands diffusion coefficients in the same order as in natural membranes ( $\approx 1 \mu\text{m}^2 \text{s}^{-1}$ ). On top of that, complex functions such as endo/exocytosis, division, extension of appendages demand membranes with extremely high flexibility and stability. Natural membranes achieve these seemingly antagonistic properties by combining phospholipid bilayers with bending rigidities of just a few tens of the thermal energy with structural components that enhance the molecular cohesion and overall stability.<sup>[6]</sup>

Vesicles assembled from (phospho)lipids, called liposomes, are the system of choice for synthetic biologists under the premise that these molecules are the majoritarian components of cell membranes. Indeed, they provide faithful mimicry of most properties except for stability. In single-component liposomes, the lack of certain molecules that enhance cohesion between the lipids significantly alters their physical properties and stability compared to natural cells. Moreover, biologically relevant lipids also lack chemical stability as their double bonds are prone to oxidation and their ester bonds prone to hydrolysis.<sup>[7]</sup> Without constant repair and replenishment as in cells, these degradation processes result in new molecules with variable physical properties and biological activity which hampers the liposome's overall properties, even at low oxidation levels.<sup>[8]</sup> Microscopically, this translates into worsening of the stability, aggregation, fusion, and leakage of encapsulated material.<sup>[7]</sup> These features complicate storage, handling and limit long-term observation of liposomes, especially under irradiation conditions during microscopy.

Polymersomes assembled from amphiphilic block copolymers represent a synthetic alternative to lipids. Their higher molecular weight and entanglement of the hydrophobic blocks drastically improve the stability of their membranes.<sup>[9]</sup> Moreover, modern controlled polymerizations give access to macromolecules with precise dispersity of each block and offer a vast synthetic space for macromolecular design to control the surface topology and reactivity of the polymersome.<sup>[10]</sup> However, the higher molecular weight inevitably leads to thicker, less flexible membranes with reduced or almost frozen dynamics.<sup>[9,11]</sup> This hampers the integration of natural building blocks such as lipids, peptides, or transmembrane proteins and affects all functions requiring membrane remodeling.<sup>[12]</sup>

Most of these caveats have been alleviated with the introduction of graft copolymers. Hydrophobic, flexible poly(dimethylsiloxane) (PDMS) backbones form the hydrophobic domains of the membrane from where poly(ethylene oxide) (PEO) side chains are sparingly grafted to generate

the hydrophilic periphery. Recent work has demonstrated the insertion of lipids, transmembrane proteins that are part of the respiratory cascade and of the SNARE system.<sup>[13]</sup> However, the complete mixing with lipids and PDMS-g-PEO was only observed for a limited range of compositions, and thus, resulted in phase separation and fission.<sup>[13c,14]</sup> These systems have been surpassed by ionic combisomes, biomimetic vesicles assembled from amphiphilic comb-polymers which demonstrated excellent mimicry of most biophysical properties and the ability to hijack complex cell membrane features.<sup>[15]</sup> However, the most advanced vesicle system is based on the self-assembly of amphiphilic Janus dendrimers (JDs) into dendrimersomes which provide a fully synthetic surrogate to lipids and glycolipids.<sup>[16]</sup> We have previously demonstrated that they can fully or partially mix with lipids, incorporate membrane proteins, carry nucleic acids, and form hybrids with natural cells to incorporate their periphery.<sup>[16a,17]</sup> Moreover, they have served as a platform to unravel how the complex 2D organization of glycans controls their reactivity and can be programmed to perform complex shape transformations akin to living cells.<sup>[18]</sup> However, the dendritic design of most JDs relied on oligo(ethylene glycol) or polyol groups as hydrophilic moieties. Such groups do not represent the periphery that natural cell membranes present to the outside and may alter the interactions of cells or natural proteins with the membrane.

In this work, we overcome this limitation by introducing a new type of zwitterionic JD that assembles into vesicles that combine the augmented properties of dendrimersomes with the PC periphery natively displayed in cells. The zwitterionic JD (JD<sup>PC</sup>) was built by appending a PC hydrophilic head group to a 3,5-didodecyl benzoate hydrophobic dendron. The latter dendron provides the appropriate balance in cohesive interactions to drive the assembly into membranes that closely mimic the thickness, lateral mobility, and flexibility of liposomes. Conversely, their molecular design addresses the weak points of phospholipids resulting in an enzymatic, thermal, and mechanical stability beyond their natural counterparts. Moreover, the zwitterionic periphery of JD<sup>PC</sup> provides stability in complex biological media such as blood plasma and compatibility with various cell lines. We show that the excellent level of biomimicry of JD<sup>PC</sup> enables the seamless integration of components of natural membranes, such as pore forming peptides, phospho-, and glycolipids as well as, structure-directing lipids to generate raft-like domains. Furthermore, the high flexibility of zwitterionic dendrimersomes (z-DSs) membranes allows to readily fuse them with liposomes which constitutes a route toward building hybrids. Finally, sensing and motility are enabled by functionalizing the z-DSs with specific enzymes. This report demonstrates the suitability of the z-DSs to serve as a platform to build active synthetic cells that imitate life and beyond.

## 2. Results and Discussion

### 2.1. Biomimetic z-DSs

We designed and synthesized a PC-based JD (JD<sup>PC</sup>) based on three considerations in our molecular design. First, the JD should structurally resemble lipids to ensure similar physical

behavior of the respective membrane. Initial reports of JDs were based on twin-twin structures, where two hydrophobic and two hydrophilic dendrons were connected to a core on opposite sites. However, we chose a single-single JD design bearing two hydrophobic chains since subsequent reports showed that such synthetically less demanding amphiphiles can also form stable and flexible DSs.<sup>[19]</sup>

Second, the hydrophobic dendron should provide additional mechanical stability to the membrane compared to lipids. We selected a dihydrobenzoate-based hydrophobic dendron since we hypothesize that  $\pi$ - $\pi$  interactions between the aromatic rings would provide an additional cohesive force and the concomitant improved stability. We incorporated a 3,5-substitution

pattern, because such DSs displayed two to six times higher energies at break compared to similar 3,4 or 3,4,5 substituted derivatives in previous micropipette aspiration experiments.<sup>[16a]</sup> The increased stability is a consequence of the more efficient interdigitation of alkyl chains in 3,5 substituted dendrons while maintaining a biomimetic thickness.<sup>[20]</sup>

Third, we chose a chain length of 12 carbon units mainly to avoid crystallization of the alkyl chains at room temperature in order to achieve flexible DSs and to yield membranes with biomimetic thickness.

We synthesized JD<sup>PC</sup> according to **Figure 1a**. We introduced the hydrophobic tails in a Williamson ether synthesis using methyl 3,5-dihydrobenzoate (**1a**) and didodecylbromide.

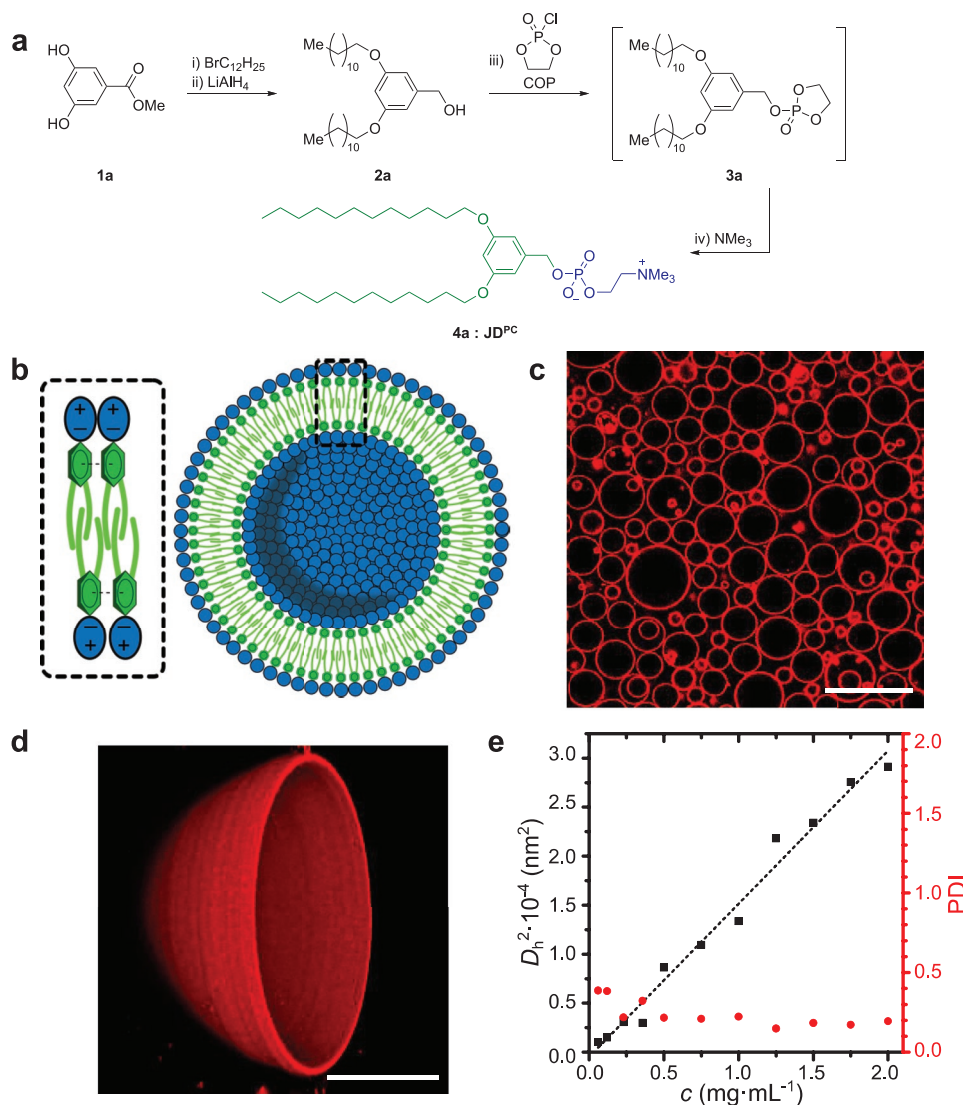


**Figure 1.** Self-assembly of JD<sup>PC</sup> into biomimetic dendrimersomes z-DSs. a) Synthetic route toward JD<sup>PC</sup>. b) Scheme of JD<sup>PC</sup> highlighting the additional cohesive  $\pi$ - $\pi$  interactions between the aromatic rings and interdigitation of the hydrophobic dendrons that drove the assembly into z-DS with improved stability. c) Giant unilamellar z-DSs assembled by electroformation method of JD<sup>PC</sup> in  $200 \times 10^{-3}$  M sucrose. The z-DSs were labeled with 0.5 mol% Nile red. Scale bar: 50  $\mu$ m. d) 3D reconstruction of 100 confocal scans showing a bisected z-DS labeled with Nile red (0.5 mol%). Scale bar: 10  $\mu$ m. e)  $D_h$  of z-DS prepared at different concentrations  $c$  by injection method and determined by DLS. The  $D_h^2$  scales linearly with the concentration and results in narrowly disperse vesicles. The polydispersity index (PDI), which measures the breadth of the distribution, was below 0.22 for all systems formed with concentrations higher than 0.4 mg mL<sup>-1</sup> (red axis).

Subsequent reduction by  $\text{LiAlH}_4$  afforded the respective benzylic alcohol **2a**. Following a phosphorylation, amination approach, we first utilized 2-chloro-2-oxo-1,3,2-dioxaphospholane (COP) to generate **3a**. The intermediate **3a** was used in an endocyclic ring-opening reaction by  $\text{NMe}_3$  to yield the desired  $\text{JD}^{\text{PC}}$  (**4a**). We also observed the formation of a cationic product ( $\text{JD}^{\text{cat}}$ ) which was likely formed by an exocyclic nucleophilic substitution of the cyclic phosphate by  $\text{NMe}_3$  (Figure S5, Supporting Information).  $\text{JD}^{\text{cat}}$  was removed by flash column chromatography and the desired  $\text{JD}^{\text{PC}}$  was isolated as a colorless waxy solid in 10% yield with respect to **1**. Thermal analysis by differential scanning calorimetry of an annealed  $\text{JD}^{\text{PC}}$  sample revealed a single transition at  $T_m = -14.3$  °C, well below room temperature (Figure S19, Supporting Information). This is a necessary requirement to form fluid and flexible membranes at room temperature.

We assembled  $\text{JD}^{\text{PC}}$  into z-DSs in various aqueous media using three different methods commonly employed for liposome and polymersome formation.<sup>[17b,21]</sup> We formed giant unilamellar z-DSs by thin-film hydration and electroformation. Both methods involve deposition of a thin film onto a substrate from a good solvent, followed by swelling and detachment of the bilayers in an aqueous medium. During electroformation the process is assisted by electrode wetting using a cyclic voltage. Both techniques produced mainly spherical unilamellar vesicles with a diameter of 15–45  $\mu\text{m}$  for the electroformation and 2–30  $\mu\text{m}$  for the thin film hydration method determined by using confocal laser scanning microscopy (CLSM) images (Figure 1c,d and Figure S20, Supporting Information for distribution of sizes). An improved vesicle yield was achieved when the assembly was carried out by electroformation in a sucrose solution. Moreover, less oligovesicular assemblies were observed for electroformation (Figure 1c). However, we found that the vesicle yields during electroformation are generally decreased when only water (no sugars, no salts) is used as a hydration medium. To study effects of vesicle size and investigate the behavior of a larger population of vesicles during our experiments, we further prepared small unilamellar DSs by the injection method. This method afforded vesicles with diameters of 40–170 nm by simply injecting an ethanolic solution of  $\text{JD}^{\text{PC}}$  into water or buffer and vortexing the resulting dispersion. Their hydrodynamic diameter ( $D_h$ ) could be controlled by the concentration of  $\text{JD}^{\text{PC}}$  ( $c_{\text{JD}^{\text{PC}}}$ ) in the resulting suspension. We found that the  $D_h$  scales with  $D_h \approx c_{\text{JD}^{\text{PC}}}^{1/2}$  as previously observed for other JDs (Figure 1e) while the polydispersity index (PDI) of their size remained low with  $\text{PDI} < 0.22$  for concentrations of at least 0.4 mg  $\text{mL}^{-1}$ .<sup>[19,20]</sup>

## 2.2. Biomimicry of z-DSs

Arguably, thickness, flexibility, and the ability to laterally organize components are the key physical properties that define the level of biomimicry of synthetic biomembranes. Giant and small unilamellar z-DSs displayed a thickness of 3.9 nm as determined by atomic force microscopy and cryo-TEM irrespective of the formation method (Figure 2a,b, Figures S21 and S22, Supporting Information). This thickness closely resembles the ones of liposomes and cell membranes ( $\approx 4$  nm).<sup>[22]</sup> We assessed

the flexibility by analyzing the membrane bending rigidity through fluctuation spectroscopy.<sup>[6b,23]</sup> For comparative studies we prepared liposomes from DLPC and the more commonly utilized POPC phospholipid having membrane thicknesses of 3.1 and 3.7 nm, respectively.<sup>[24]</sup> We chose DLPC due to a similar hydrophobic chain length compared to  $\text{JD}^{\text{PC}}$  (C12). POPC contains one saturated C16 chain and a C18 chain bearing one double bond. First, we assessed the angular fluctuation of radii of deflated vesicles as a qualitative observation of their flexibility. The thermal energy was sufficient to cause fluctuations across the whole membrane, which were close to the ones observed in liposomes as depicted in the angular distribution of radii (Figure S24, Supporting Information). On the other hand, polymersomes assembled from block copolymers of poly( $\text{BD}_{87}\text{-}b\text{-EO}_{72}$ ) displayed hardly any fluctuation at room temperature (Figure S24, Supporting Information). These qualitative observations are subjected to the degree of deflation of the specific vesicles investigated. To quantitatively characterize the bending modulus ( $\kappa$ ), which measures the resistance of the membrane to bend, we investigated the fluctuation spectra of giant vesicles using contour detection and Fourier analysis.<sup>[23a,c,25]</sup> Remarkably,  $\kappa$  for z-DSs were only 20  $k_B T$ , which is  $\approx 15\%$  and 65% lower than those of liposomes from DLPC and POPC, respectively. Such values indicate that z-DS membranes are highly flexible and can thereby support complex processes that require sculpturing of the membrane (Figure 2c). Similarly, the areal expansion coefficient ( $K_A$ ), which measures the resistance of the membrane to stretch, was 149  $\text{mN m}^{-1}$ , close to the one of POPC, 141  $\text{mN m}^{-1}$  (Figure S23, Supporting Information).

We estimated the lateral mobility of the membranes by measuring the diffusion coefficient ( $D$ ) of a fluorescently labeled lipid (Liss Rhod-PE) by fluorescence recovery after photobleaching of supported bilayers. z-DS membranes displayed a  $D$  of 2.4  $\mu\text{m}^2\text{-s}^{-1}$ , which is in the same range as the ones for the studied liposomes (Figure 2d) and 10 to 1000 times larger than those for some polymersomes.<sup>[26]</sup> The high  $D$  of z-DSs suggests that membrane components can rapidly spatially rearrange as in cell membranes.

Another key property of living cells is the ability to reseal their membrane in events of damage. In case the membrane is punctured, the amphiphiles are required to rapidly rearrange at the edges. The energy penalty for this rearrangement is reflected in the edge tension which drives pore-closing. The larger the edge tension, the faster the pore will close.<sup>[27]</sup> We investigated the pore closure dynamics of z-DSs with the electroporation technique (Figure 2e,f and Figure S25, Supporting Information).<sup>[28]</sup> Vesicles encapsulating a solution with differing conductivity compared to the outside medium were subjected to an electric pulse. The application of the field generates a transmembrane potential and a force normal to the membrane which opens a pore. From the dynamics of the closure of the pore, we determined the edge tension of liposome and z-DS membranes using a previously reported approach.<sup>[29]</sup> The pores generated in z-DSs closed significantly faster which is reflected in a higher edge tension of 61 pN compared to DLPC and POPC for which we obtained values of 13 and 39 pN, respectively. The higher drive for pore-closure in z-DSs might be the result of reduced interdigitation or  $\pi$ - $\pi$  interaction at the highly curved pore interface.

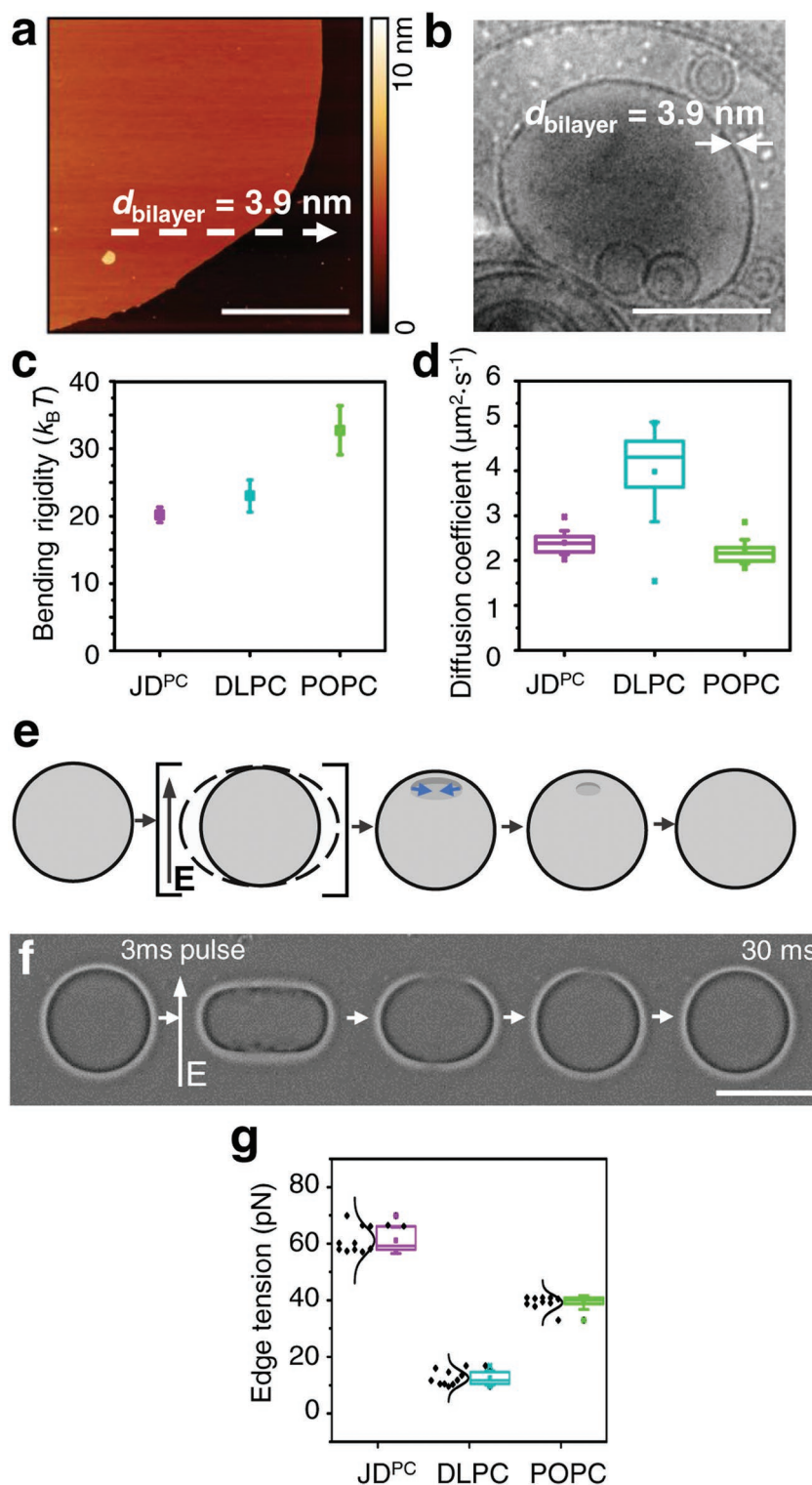


**Figure 2.** Physical characterization of z-DSs and comparison with DLPC and POPC liposomes. a) AFM height image of a deposited z-DS on mica. Height analysis along the white arrow yields a bilayer thickness of 3.9 nm. Scale bar: 4 μm. b) Cryo-TEM of a z-DS formed by the injection method. Contour analysis confirms the bilayer thickness of 3.9 nm. Scale bar: 200 nm. c) Bending rigidity determined by fluctuation analysis. Each point depicts the average value of six analyzed vesicles with the standard deviation. d) Diffusion coefficient calculated from fluorescence recovery after photobleaching (FRAP). e) Scheme of a vesicle undergoing electroperoration. An electric field is applied for 3 ms which deforms the vesicles and creates a pore. Pore formation (observed by the interrupted vesicle halo), and pore closing within 30 ms. Scale bar: 50 μm. f) Phase contrast images of the process of electroperation of z-DS showing vesicle deformation, pore formation (observed by the interrupted vesicle halo), and pore closing within 30 ms. Scale bar: 50 μm. g) Box plot and distribution of the edge tension. d,g) Each box of the boxplot was obtained from measurements on ten individual vesicles (25th–75th percentile of each data set). The median is a line and the average value is an open rectangle. The standard deviation is indicated by the whiskers while the outliers are displayed outside of the whiskers.

### 2.3. Stability of z-DSs

First, we examined the bench stability of JD<sup>PC</sup> and z-DSs after prolonged storage under lab conditions. Neither NMR nor analytical high performance liquid chromatography showed any difference in JD<sup>PC</sup> composition after 9 months of storage (Figure S14a–c, Supporting Information). Furthermore, no changes in the hydrodynamic diameter nor its distribution could be observed by dynamic light scattering of z-DSs after 3 months (Figure S14d, Supporting Information). Giant z-DSs prepared in  $10 \times 10^{-3}$  M HEPES buffer (pH 7.4) by thin-film

hydration remained intact after 18 months storage under lab conditions (Figure S15, Supporting Information). Remarkably, giant z-DSs encapsulating calcein retained their cargo despite storage for 12 months (Figure S16, Supporting Information). In a similar vein, z-DSs displayed a higher thermal stability than its liposomal counterparts (Figure 3b). Giant liposomes (POPC and DLPC) and z-DSs with encapsulated green fluorescent calcein were observed in CLSM before and after heating to 80 °C for 1 h. While z-DSs remained intact (Figure 3b), liposomes formed from DLPC or POPC underwent breakage and aggregation which led to quenching of the calcein by Co<sup>2+</sup> ions from

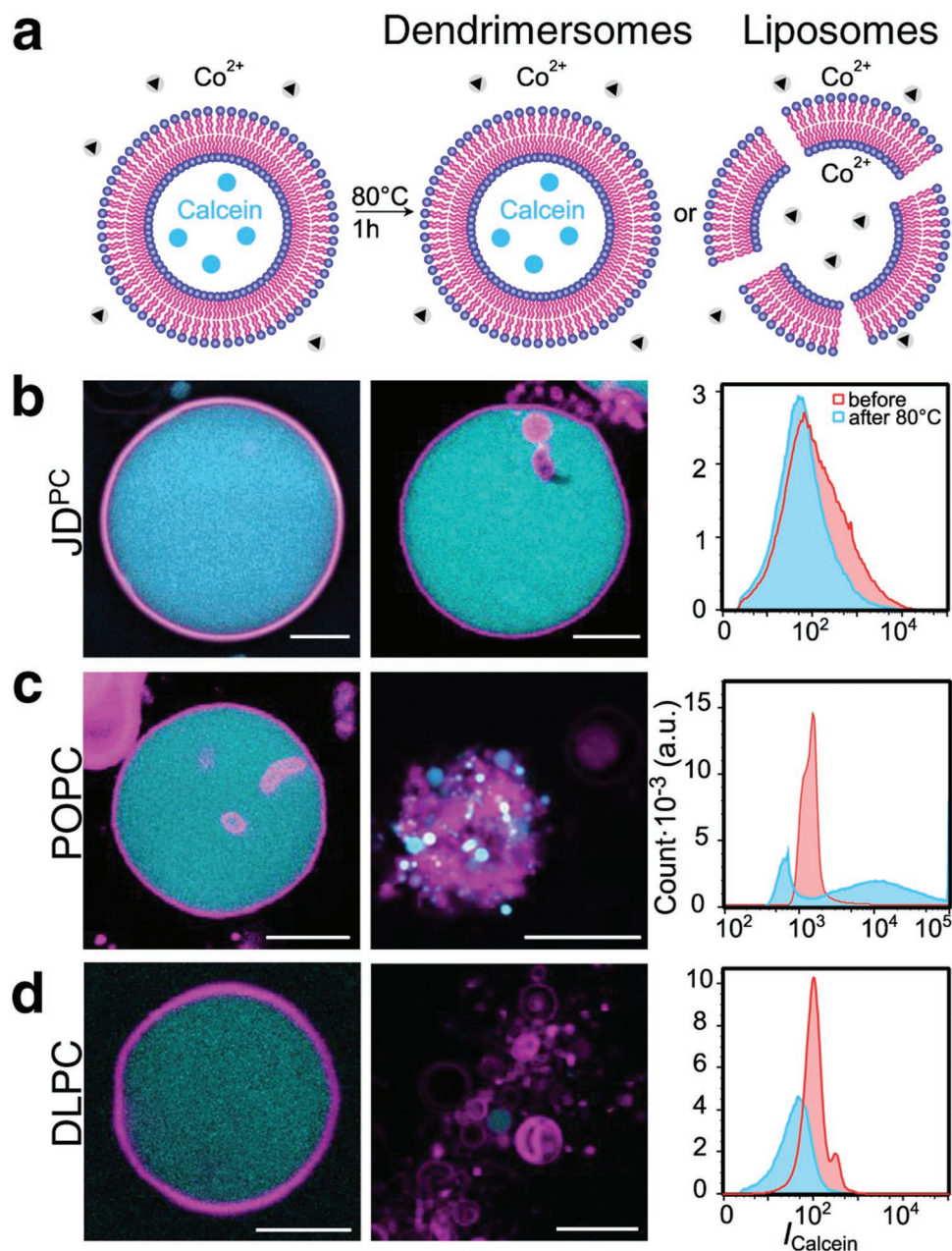


**Figure 3.** a) Scheme of the the experimental conditions for the analysis of the thermal stability of z-DSs and liposomes. The vesicles were formed in a calcein solution and the external calcein was quenched by the addition of Co<sup>2+</sup>. b–d) Calcein-filled vesicles were heated for 1 h at 80 °C and cooled down before analysis by CLSM and FACS: b) z-DS, c,d) liposomes from POPC and DLPC, respectively. Scale bars: 10 μm.

the outer solution (Figure 3c,d). These observations were confirmed by fluorescence-activated cell sorting (FACS) before and after heating. FACS allows to investigate a much larger population of vesicles in the sample compared to CLSM. We observed no significant shift in the histogram of green fluorescence before and after heating of z-DSs confirming that the vesicles remained intact demonstrating an excellent thermal stability. Conversely, the histograms of both liposomes indicated a high degree of degradation and possible aggregation in agreement with CLSM. The overall, higher thermal and chemical stability are well in line with the higher mechanical stability as determined by puncture AFM.<sup>[30]</sup>

The higher stability of z-DSs compared to liposomes is likely related to additional cohesive interactions stemming either from the hydrophobic dendrons or the highly hydrated zwitterionic PC. To elucidate the contributors to the enhanced stability of z-DSs we compared its resistance to high temperature with other classic dendrimersomes. We formed calcein-filled dendrimersomes from JDs having non-zwitterionic triethylene-glycol-substituted benzoates hydrophilic groups while having the same single-single (JD<sup>s-s</sup>) or a double (twin-twin, JD<sup>tw-tw</sup>) hydrophobic dendron. The thermal treatment at 80 °C for 1 h destabilized the JD<sup>s-s</sup> dendrimersomes, which now formed aggregates and drops (Figure S18, Supporting Information). On the other hand, the lumen of JD<sup>tw-tw</sup> dendrimersomes remained green fluorescent, indicating that they were stable. The comparable higher stability arises from the increased hydrophobic effect stemming from the presence of two hydrophobic dendrons in JD<sup>tw-tw</sup>. z-DSs displayed a high stability, comparable to those of JD<sup>tw-tw</sup> dendrimersomes despite being assembled from a single-single type dendrimer. This suggests that not only the hydrophobic didodecyl-substituted benzoates play a role in the enhanced stability but that additional cohesive interactions stemming from its PC group are at play.

Additionally, we examined the stability of calcein filled z-DSs under shear stress in a flow cell. They retained their cargo and remained intact even under shear stresses between  $\tau_w = 1.47$ – $2.45$  Pa, which are comparable to values of shear stresses in physiological conditions (Figure S17, Supporting Information).

## 2.4. Co-Assembly Studies

We assessed the ability of JD<sup>PC</sup> to form hybrid membranes with lipids by co-assembly with a fluorescently labeled 16:0 Liss Rhod-PE lipid in a lipid concentration range of 0.1–20 mol%. All lipid compositions yielded hybrid vesicles (Figure 4a, Figure S26, Supporting Information) without any observable phase separation in CLSM. We also examined the co-assembly with the glycolipid 16:0–18:1 DG glucose lipid (10 mol%), resulting in the preferential formation of onion-like hybrid vesicles (Figure 4b). The tendency to form onion structures is likely a result of attractive glycan–glycan interactions between glucose groups leading to a close association of the bilayers, similar to previously reported glycodendrimersomes.<sup>[31]</sup> We further studied the generation of raft-like microdomains by the co-assembly with lipids of varying saturated chain lengths between C12 and C18. Increasing the chain length increases the thermodynamic drive to generate more order phases. The

polarity-sensitive fluorescent probe Laurdan is commonly utilized to visualize domains with different degrees of ordering in hybrid vesicles via generalized polarization (GP) imaging.<sup>[32]</sup> GP values range between  $-1$  and  $+1$  where more positive values are obtained in more ordered domains. By mapping the GP values for each pixel of hybrid vesicle images (Figure 4c) we obtained the respective GP distributions (Figure 4d). The co-assembly with DLPC (C12) and DPPC (C16) resulted in homogeneous membranes with monomodal GP distributions indicating homogeneous mixing between JD<sup>PC</sup> and the lipids with no observable phase-separation. This is especially noteworthy in the case of DPPC hybrid vesicles, where the lipid's main phase transition temperature is significantly above room temperature. However, in hybrid vesicles of JD<sup>PC</sup> and DSPC (C18), the larger hydrophobic mismatch drove phase separation (Figure 4d). Distinct microphases were visible in CLSM which are reflected in the GP distributions where two peaks at GP =  $-0.4$  and GP =  $0.2$  stemming from the low and high ordered domains, as confirmed by analyzing each of the regions (Figure S27, Supporting Information). Interestingly, the majority of these hybrid vesicles were faceted where the flat faces are dominantly formed by more ordered green patches and curved regions between facets by less ordered blue patches stemming from DSPC-rich and JD<sup>PC</sup>-rich domains (Figure 4c,d, Figures S27 and S28, Supporting Information). Phase separation in binary liposomes of DLPC with DSPC and even DAPC (C20) has been reported, but to our knowledge, none of these systems displayed faceted vesicle.<sup>[33]</sup> Such a unique behavior may be explained by a more complete segregation between DSPC and JD<sup>PC</sup> enabling the crystallization of the long alkyl chains and the formation of facets.

Moreover, we studied the ability of z-DSs to integrate externally added pore-forming peptides. The addition of  $\alpha$ -hemolysin to a suspension of calcein-filled z-DS resulted in rapid quenching of the fluorescence by Co<sup>2+</sup> present in the external solution (Figure 4e). These results were confirmed by FACS where the peak position of green calcein fluorescence significantly shifted to lower intensities upon  $\alpha$ -hemolysin addition suggesting successful formation of a pore and the transport of Co<sup>2+</sup> ions into the vesicle lumen from the outer solution. The second peak, overlapping with the vesicle population before pore formation, is most likely related to multilayered vesicles where the calcein fluorescence is only quenched in between the outermost layers. The rapid formation of a functional pore without compromising the integrity of the z-DS indicates that  $\alpha$ -hemolysin could insert, match the membrane dimensions, diffuse, and form the heptameric pore that enabled the transport of ions across an otherwise Co<sup>2+</sup>-impermeable membrane. These results highlight the excellent biomimicry of z-DSs.

## 2.5. Interaction with Biological Media

To test the biocompatibility of z-DSs, we first studied interactions between proteins and z-DSs by observing the change of the hydrodynamic diameter of small z-DS in DLS (Figures S29b and S31, Supporting Information). z-DSs were mixed with bovine serum albumin (BSA) and lysozyme in buffer as models of anionic and cationic proteins, as well as with human blood

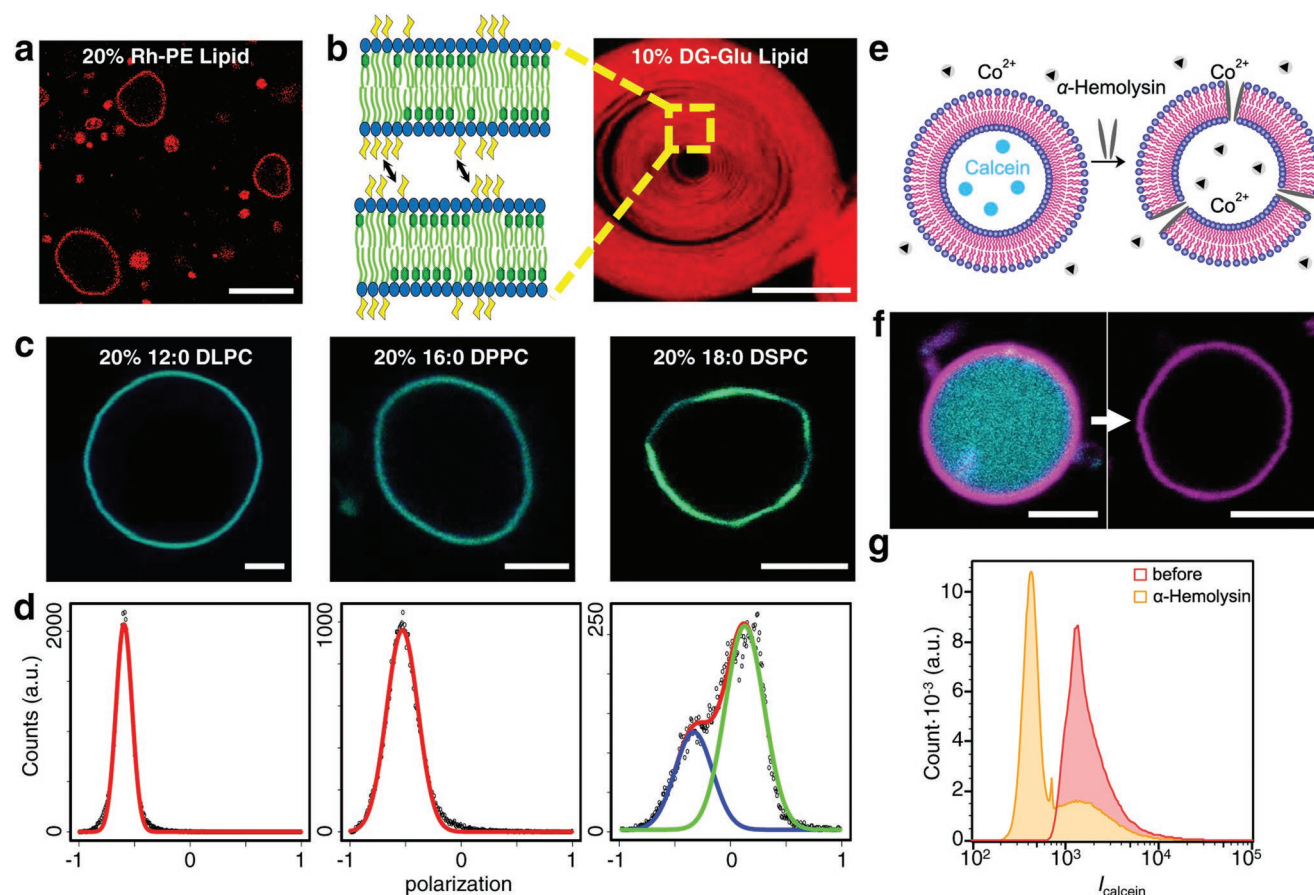


**Figure 4.** Co-assembly of z-DSs with structure-directing lipids and pore-forming peptides. a) Hybrid z-DS–lipid with 20 mol% of Liss Rhod-PE (red). Scale bar: 10  $\mu\text{m}$ . b) Co-assembly with 10 mol% DG-Glu lipid leads to the formation of onion vesicles resulting from glycan–glycan interactions between the bilayers. c) Co-assembly of JD<sup>PC</sup> with 20 mol% of lipids with varying hydrophobic chain length: DLPC (C12), DPPC (C16), and DSPC (C18). Vesicles were labeled with Laurdan as a polarity sensitive probe while the emission was detected at  $\lambda_1 = 415\text{--}445$  nm (green) and  $\lambda_2 = 490\text{--}530$  nm (blue). CLSM images show the merged image of both emission ranges. Scale bars: 5  $\mu\text{m}$ . d) Distribution of the GP of Laurdan in z-DSs–lipid hybrids. e) Scheme of the pore formation with addition of  $\alpha$ -hemolysin which enabled the transport and quenching of calcein fluorescence by  $\text{Co}^{2+}$ . f) CLSM images of the addition of  $\alpha$ -hemolysin to calcein-filled z-DSs. The membrane of z-DSs was labeled with Nile red (magenta) while the vesicle lumen contains calcein (cyan). Scale bars: 5  $\mu\text{m}$ . g) FACS shows a decrease in calcein fluorescence intensity after addition of  $\alpha$ -hemolysin confirming pore formation and quenching of calcein in the lumen by  $\text{Co}^{2+}$ .

plasma (10%). Plasma is the most challenging biological fluid.<sup>[34]</sup> In all cases, we observed no increase in the hydrodynamic diameter compared to the pure vesicle dispersion, even after a contact time of 24 h. Since no detectable increase in the hydrodynamic radius occurred due to protein adsorption or vesicle aggregation, we conclude no significant fouling of the vesicles. This evaluation was also carried out for giant z-DS using CLSM. z-DSs assembled in  $10 \times 10^{-3}$  M HEPES buffer remained intact in BSA, lysozyme, and 10% blood plasma solutions (Figure S32, Supporting Information). Although such z-DSs were stable even in blood plasma, we observed a lower density of vesicles, presumably due to the high osmotic difference between the HEPES buffer and the blood plasma. To minimize osmotic shock, we repeated the study but formed z-DSs in sucrose solution ( $300 \times 10^{-3}$  M) with higher osmolarity. In this case, we observed a high density of intact vesicles after an incubation time of  $t = 30$  min (Figure S33, Supporting Information) and  $t = 24$  h (Figure S34, Supporting Information), even in pure blood plasma. To closely monitor the interactions

of proteins and giant z-DSs, we incubated vesicles with fluorescently labeled BSA (Texas Red, red) in CLSM (Figure S35, Supporting Information). After 24 h we did not observe any increase in red fluorescence signal at the membrane revealing that no significant amounts of BSA proteins had attached to the JD<sup>PC</sup> membrane. Contrarily, a significant increase in red fluorescence was detected at the outer membrane periphery in the positive control which consisted of positively charged dendrimersomes co-assembled from JD<sup>PC</sup>:JD<sup>cat</sup> (8:2 molar ratio).

To test the compatibility with living cells, we performed a standardized colorimetric cell viability assay using three different cell types: immortalized human cancer cells (Caco-2 and HeLa), as well as cells related to human lung epithelium (H441). In all cell types, we observed a cell viability of 100% when contacted with z-DSs (Figure S29a, Supporting Information) demonstrating that z-DSs are non-cytotoxic and biocompatible. The z-DSs display an excellent biocompatibility as they maintain their structural integrity when contacted with proteins and display no cytotoxicity. Moreover, we tested whether the giant

z-DSs could be internalized into cells by incubation of fluorescently labeled z-DSs with normal human dermal fibroblasts for 24 h (Figure S30, Supporting Information). Observation by dual fluorescence/phase contrast microscopy revealed the presence of both, vesicles and fibroblasts upon mixing. After a subsequent washing step, only living fibroblasts remained, demonstrating that giant z-DSs do not attach to or internalize into cells.

## 2.6. Fusion with Liposomes

Vesicle fusion is an essential mechanism that drives biological processes such as intra- and inter-cellular transport, communication, signaling, protein sorting, endocytosis, and even infections.<sup>[35]</sup> To mimic the fusion process on a basic level we studied the charge-mediated fusion, which was shown to be very efficient for liposomes.<sup>[36]</sup> Here, we investigated charge-mediated fusion of JD<sup>PC</sup> vesicles with liposomes by CLSM as giant vesicles. Cationic DSs were prepared by co-assembling JD<sup>PC</sup> with JD<sup>cat</sup> and labeling with red-fluorescent Liss Rhod-PE. Anionic liposomes were prepared by the co-assembly of DLPC with DLPG and labeled with green-fluorescent NBD-PC lipid (Figure 5, Figures S36 and S38, Supporting Information). Upon mixing the two vesicle dispersions, we observed three dominant behaviors (Figure 5): 1) vesicles with one fluorescence signal indicating no fusion, 2) adhesion between z-DSs and liposomes visualized by the distinctly different fluorescence of the systems, and 3) vesicles with an overlap of both fluorescence signals across the whole membrane demonstrating full fusion. To estimate fusion efficiency, we analyzed CLSM images of 410 vesicles after 4 h of incubation (Figure S39, Supporting Information). Based on the ratio of remaining unfused vesicles we estimate that 92% of possible fusion events occurred. Additionally, we studied global behavior by fluorescence resonance energy transfer (FRET) using fluorescence spectroscopy (Figure 5c).<sup>[37]</sup> Acceptor vesicles were assembled from DLPC:DLPG (8:2 molar ratio) containing no dye. Donor vesicles were assembled from JD<sup>PC</sup>:JD<sup>cat</sup> (8:2 molar ratio) containing two FRET dyes (0.5 mol% Liss Rhod-PE and 0.5 mol% NBD-PE). The close proximity of the fluorescent dyes in the donor vesicles results in their quenching. Fusion between donor and acceptor vesicles increases the fluorescence intensity as the dyes are diluted over the additional membrane area and thereby their respective distance increases. The maximum fluorescence intensity was obtained by adding Triton X to the donor DSs (Figure S37, Supporting Information).<sup>[13d]</sup> Obtained fluorescence intensities were calculated relative to the determined maximum. Upon addition of acceptor vesicles to the donor dendrimersomes at  $t = 200$  s, we observed an increase in the relative fluorescence intensity which reached a plateau of 40% after 2500 s. These results demonstrate successful fusion and incorporation of both dyes inside the generated JD-lipid hybrid vesicles. Cationic DSs also underwent fusion with neutral liposomes indicating favorable kinetics, despite a lack of opposing charges (Figure S40, Supporting Information). Since no fusion occurred when neutral z-DSs were mixed with neutral or anionic liposomes (Figure S41, Supporting Information), we hypothesize that the conical shape of JD<sup>cat</sup> stabilizes

the energetically unfavorable inverted micellar intermediate during fusion and thereby reducing the imposed kinetic barrier.<sup>[38]</sup> However, the lack of opposing charges led to a decreased efficiency as only an estimated 37% of possible fusion events occurred within 4 h.

We additionally studied the fusion of small vesicles ( $D_h < 140$  nm) by DLS (Figure S42, Supporting Information). Hybrid vesicles of fused cationic DSs and anionic liposomes displayed sizes that are consistent with theoretical values for binary fusion assuming conservation of volume (Section 4.16.4, Supporting Information). Other vesicle compositions did not afford vesicles with a measurable increase in size due to less efficiency or overall lack of fusion.

## 2.7. Motility

Living organisms heavily depend on cell motility for survival, feeding, and mass transport. Their locomotion requires significant amounts of energy since cells operate at low Reynolds numbers where they experience viscous forces that dominate the inertial ones.<sup>[39]</sup> As a result, cells have evolved various mechanisms for cell motility that rely on complex machinery. However, much simpler propulsion methods based on enzymatic decomposition of small molecules accompanied by gas formation have been utilized in liposomes and polymerosomes.<sup>[40]</sup> H<sub>2</sub>O<sub>2</sub> is often used as a chemical fuel that can be readily transported inside the lumen to enzymatically decompose into innocuous water and oxygen by catalase to provide propulsion.<sup>[41]</sup> We used a minimal system to harvest chemical energy from externally supplied H<sub>2</sub>O<sub>2</sub> to enable propulsion. We encapsulated catalase in the lumen of z-DSs. No motion was observed in the absence of H<sub>2</sub>O<sub>2</sub> as shown in Figure 6a and Figure S26, Supporting Information. Addition of H<sub>2</sub>O<sub>2</sub> and mixing followed by observation in a chamber (10 min after addition) resulted in significant movement of vesicles across the medium (Figure 6b). Initially, (less than 15 min) the motion appears random while later there seems to be a correlated motion. To rule out convection as a possible artifact we examined the mean square displacement (MSD, Figure S43, Supporting Information) which showed no parabolic component demonstrating the motion was not convective. Moreover, the MSD followed a linear function in the first 15 min and in the last 8 min indicating diffusive motion on average well in line with propulsion after fuel consumption. The broken segments in between indicate the driven motion in random directions.<sup>[42]</sup>

## 2.8. z-DSs Sense the Presence of H<sub>2</sub>O<sub>2</sub> in Their Surrounding

Cells use chemistry as a language to communicate with each other.<sup>[43]</sup> They produce and release signaling molecules to elicit responses by neighboring cells. An example of such molecules is H<sub>2</sub>O<sub>2</sub>. Elevated hydrogen peroxide levels are expressed by cells under oxidative stress or in cancer cells. Neighboring cells sense H<sub>2</sub>O<sub>2</sub> and respond by initiating processes related to preventing and repairing oxidative damage.<sup>[44]</sup> Building artificial cells that are able to sense biomolecules is regarded as a key technology to bridge the gap between synthetic and natural

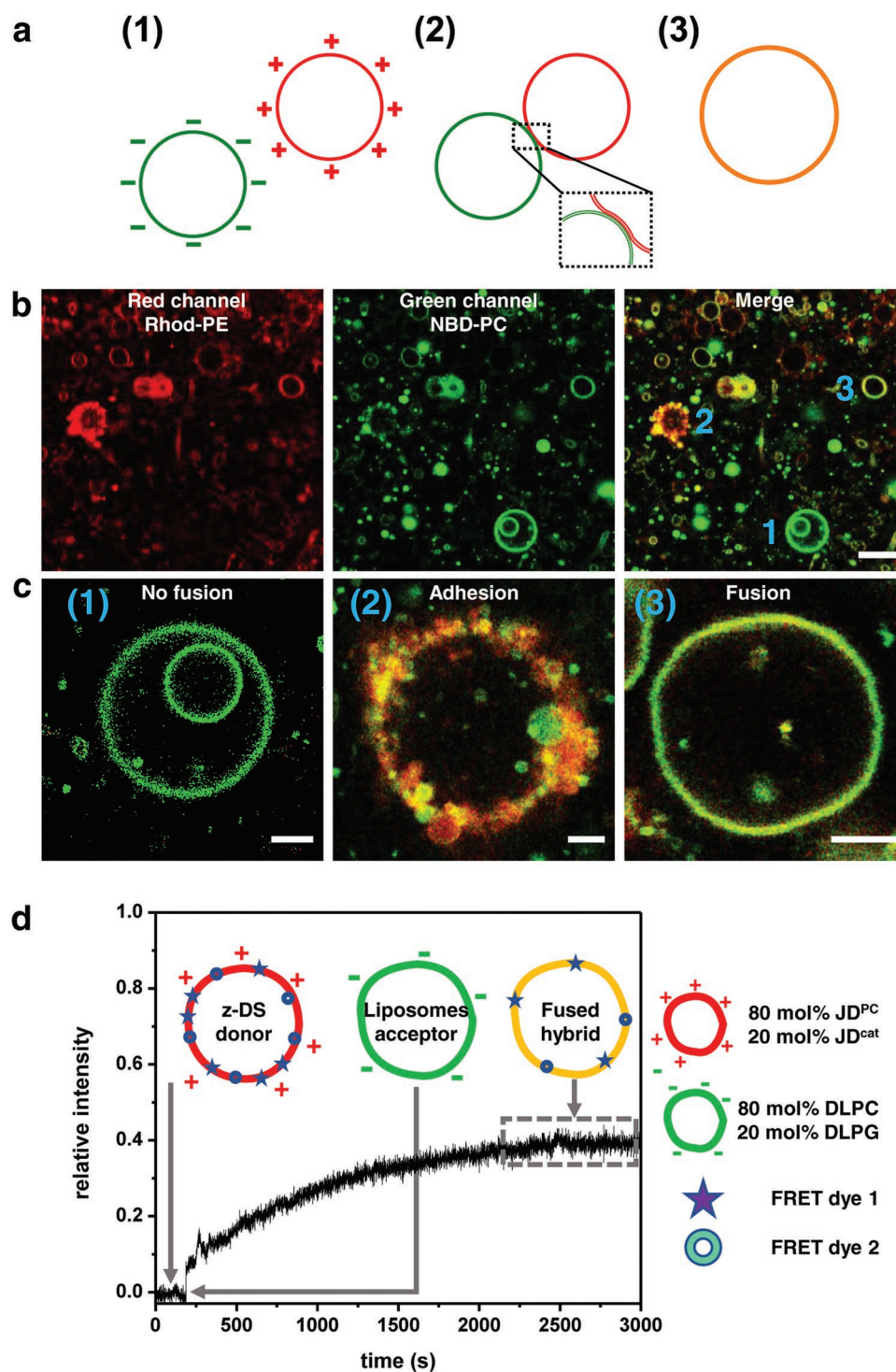


**Figure 5.** Fusion of DSs with liposomes driven by electrostatic interactions. a) Scheme of the fusion process: 1) The negatively charged liposomes (green) are attracted to a positively charged DSs (red) due to Coulombic interactions. 2) This is followed by adhesion and docking with the concomitant bending of the contact region. 3) Fusion proceeds few minutes afterward and the dyes are exchanged which yields an apparent orange color in the merged CLSM image. b) CLSM overview after mixing of positively charged JD<sup>PC</sup>:JD<sup>cat</sup> (8:2 molar ratio) DSs (1 mol% Liss Rhod-PE, red) and negatively charged DLPC:DLPG (8:2 molar ratio) liposomes (1 mol% NBD-PC, green). c) Selected vesicles showing: 1) no fusion, 2) adhesion, or 3) full fusion. d) A large population of vesicles was studied by FRET using fluorescence spectroscopy where the donor contains both FRET dyes. Upon addition of acceptor vesicles, a fluorescence increase was detected consistent with the formation of fused hybrids. Scale bars: 20  $\mu\text{m}$  in (a) and 5  $\mu\text{m}$  in (b).

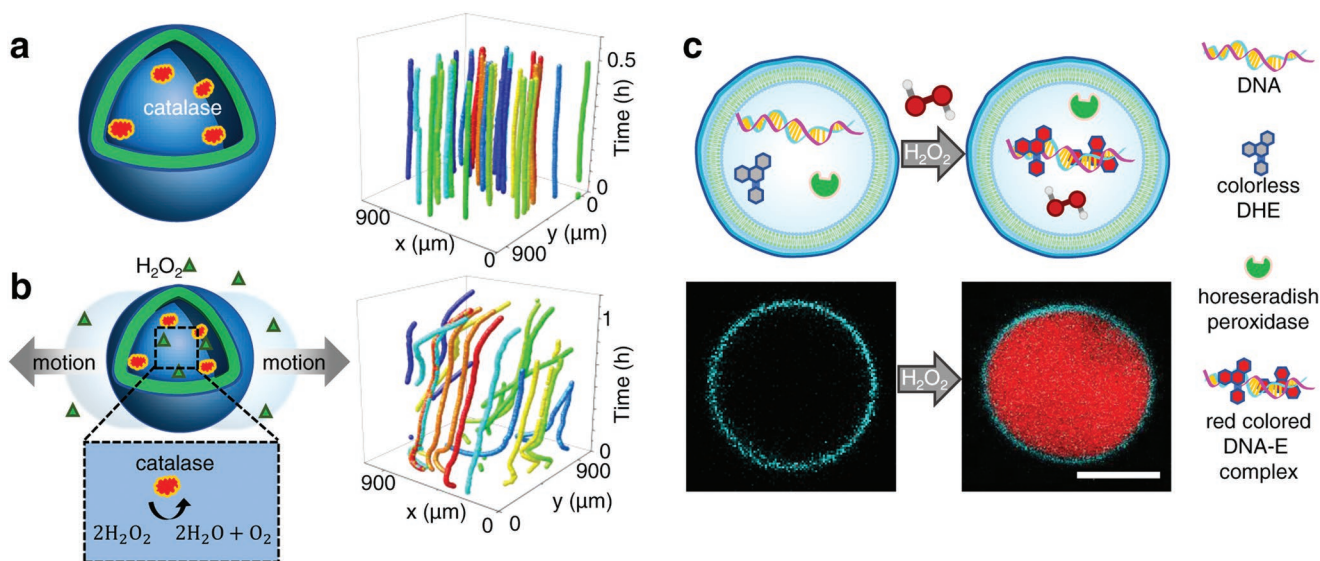


**Figure 6.** Programming motility in z-DSs. a) The position of catalase-filled z-DSs was monitored in CLSM for 30 min. Within the observation time the position of the vesicles in  $x$  and  $y$  remained constant. b) In contrast, after addition of hydrogen peroxide, the vesicles exhibited strong motion. The movement is due to catalase that catalyzes a reaction within the vesicle lumen leading to a decomposition of hydrogen peroxide into water and oxygen. c) z-DSs are utilized as a biosensor. Within z-DSs we encapsulated DNA, horseradish peroxidase (HRP), and dihydroethidium (DHE). Upon addition of membrane permeable hydrogen peroxide in the external solution, a red colored DNA-E complex is formed within the vesicle lumen. The generation of red fluorescence within the lumen was monitored by CLSM. The membrane was labeled with 1 mol% Laurdan. Scale bar: 5  $\mu\text{m}$ .

cells. We formed  $\text{H}_2\text{O}_2$ -detecting z-DSs by encapsulating horseradish peroxidase and DNA and incubating them with membrane-permeable dihydroethidium (DHE) (Figure 6c). Upon addition of  $\text{H}_2\text{O}_2$ , HRP catalyzed the oxidation of DHE to ethidium (E) which intercalates with DNA to generate a red fluorescent product within the z-DS lumen.<sup>[45]</sup>

We performed control experiments that exclude any effect of the laser that was used for excitation of the dye and proved that only upon addition of  $\text{H}_2\text{O}_2$  fluorescence within the vesicle lumen was generated (Figure S44, Supporting Information). We utilized fluorescence spectroscopy as a more sensitive technique to study the global behavior z-DSs that were prepared in the same manner. The addition of  $\text{H}_2\text{O}_2$  led to an immediate gradual increase in fluorescence intensity that reached a plateau after 2000 s. Under these conditions a  $\text{H}_2\text{O}_2$  concentration as low as 35  $\mu\text{M}$  was detectable (Figure S45, Supporting Information). These results demonstrate the first steps toward the production of synthetic biosensors to detect environments with elevated  $\text{H}_2\text{O}_2$  concentrations in medical applications or environmental science.

### 3. Conclusion

We have introduced a new concept for cell-membrane mimicry based on the self-assembly of a JD bearing a PC head-group ( $\text{JD}^{\text{PC}}$ ) into z-DSs. In the molecular design of  $\text{JD}^{\text{PC}}$  we strategically eliminated the weak points that cause degradation and low stability of liposomes. This resulted in membranes with a higher chemical and mechanical stability compared to liposomes. The resulting vesicles mimic the periphery of natural cell membranes, as well as their most essential physical properties such as bilayer thickness, flexibility, and lateral

mobility. Such high level of biomimicry enabled the incorporation of lipids, glycolipids, and protein pores. Functionalization of the membrane with structure directing lipids allowed us to program the formation of onion-type vesicles and raft-like domains. We employed these z-DSs to mimic essential cellular functions such as fusion, environmental sensing, and motility on a basic level. We envision that our system offers a platform for minimal cell mimics that, despite their synthetic nature, can integrate and interact with living matter. It offers a superior alternative to liposomes by virtue of its chemical stability that not only improves handling and usage in mild conditions but also allows studies at elevated temperatures.

### 4. Experimental Section

**Statistical Analysis:** The reported syntheses were performed at least twice to confirm the reproducibility of the results. All directly measured data were presented without pre-processing unless stated otherwise. All boxplots were generated from at least 10 data points containing 25–75% of the data set. Qualitative angular fluctuation analysis in Figure S24, Supporting Information was performed on a single snapshot of a representative vesicle for each composition while quantitative analysis of bending rigidities is depicted in the interval plots in Figure 2c which were generated from 6 data points for each composition. Protein experiments were performed in triplicate. For temperature stability, insertion of  $\alpha$ -hemolysin, biocompatibility in protein solutions and blood plasma, sensing, as well as fusion we obtained data on different locations by always studying a population of giant and small vesicles, respectively. For CLSM we show multiple CLSM overviews and selected representative single vesicles. Additional quantitative characterization was done in FACS with 15 000 events per sample, in FRET using fluorescence spectroscopy and in DLS. The analysis of vesicle size distribution was performed with 100 vesicles (Figure S20, Supporting Information) while for the calculation of fusion efficiency 410 and 344 vesicles were analyzed from CLSM images (Table S6, Supporting

Information). The interval plots in Figure S23a, Supporting Information were generated from 13 data points for z-DSs and 6 for POPC liposomes. All data were processed according to the description in the respective supporting information section. Statistical analysis and data fitting were performed in OriginPro2018, Python, and R.

## Supporting Information

Supporting Information is available from the Wiley Online Library or from the author.

## Acknowledgements

This project was financially supported by the European Commission within a H2020-NMBP-TR-IND-2018, EVPRO grant 814495-2. Moreover, the authors acknowledge support of RWTH University via the calls Innovation Sprint 2021 (project ANVIVES) as part of the “Exzellenz Start-up Center NRW” initiative and ERS Seed Fund Project SFSynt003 and ERS Seed Fund Project SFSynt005. IBEC is a member of the CERCA program. M.A. acknowledges funding from International Max Planck Research School on Multiscale Bio-Systems (IMPRS).

Open access funding enabled and organized by Projekt DEAL.

## Conflict of Interest

The authors declare no conflict of interest.

## Data Availability Statement

The data that support the findings of this study are available from the corresponding author upon reasonable request.

## Keywords

biosensors, bottom-up synthetic biology, hybrid vesicles, synthetic cells, vesicle fusion, vesicle motility, zwitterionic dendrimersomes

Received: July 11, 2022

Revised: September 7, 2022

Published online: October 31, 2022

- [1] a) P. Schwille, *Science* **2011**, *333*, 1252; b) P. Schwille, J. Spatz, K. Landfester, E. Bodenschatz, S. Herminghaus, V. Sourjik, T. J. Erb, P. Bastiaens, R. Lipowsky, A. Hyman, P. Dabrock, J.-C. Baret, T. Vidakovic-Koch, P. Bieling, R. Dimova, H. Mutschler, T. Robinson, T. Y. D. Tang, S. Wegner, K. Sundmacher, *Angew. Chem., Int. Ed.* **2018**, *57*, 13382; c) R. J. Brea, M. D. Hardy, N. K. Devaraj, *Chem. - Eur. J.* **2015**, *21*, 12564; d) F. Lussier, O. Stauer, I. Platzman, J. P. Spatz, *Trends Biotechnol.* **2021**, *39*, 445.
- [2] a) S. J. Singer, G. L. Nicolson, *Science* **1972**, *175*, 720; b) H. F. Lodish, *Molecular Cell Biology*, W. H. Freeman, New York **2016**.
- [3] a) F. Bezanilla, *Nat. Rev. Mol. Cell Biol.* **2008**, *9*, 323; b) K. Keren, *Eur. Biophys. J.* **2011**, *40*, 1013; c) D. C. Gadsby, *Nat. Rev. Mol. Cell Biol.* **2009**, *10*, 344.
- [4] O. G. Mouritsen, M. Bloom, *Biophys. J.* **1984**, *46*, 141.

- [5] D. Morzy, M. Bastings, *Angew. Chem., Int. Ed.* **2022**, *61*, e202114167.
- [6] a) W. Rawicz, K. C. Olbrich, T. McIntosh, D. Needham, E. Evans, *Biophys. J.* **2000**, *79*, 328; b) R. Dimova, *Adv. Colloid Interface Sci.* **2014**, *208*, 225.
- [7] M. Grit, D. J. A. Crommelin, *Chem. Phys. Lipids* **1993**, *64*, 3.
- [8] a) A. Reis, C. M. Spickett, *Biochim. Biophys. Acta, Biomembr.* **2012**, *1818*, 2374; b) E. Schnitzer, I. Pinchuk, D. Lichtenberg, *Eur. Biophys. J.* **2007**, *36*, 499; c) K. A. Runas, N. Malmstadt, *Soft Matter* **2015**, *11*, 499.
- [9] B. M. Discher, Y. Y. Won, D. S. Ege, J. C. Lee, F. S. Bates, D. E. Discher, D. A. Hammer, *Science* **1999**, *284*, 1143.
- [10] a) J. Lefley, C. Waldron, C. R. Becer, *Polym. Chem.* **2020**, *11*, 7124; b) M. Massignani, H. Lomas, G. Battaglia, in *Modern Techniques for Nano- and Microreactors/-reactions*, Advances in Polymer Science, Vol. 229 (Ed: F. Caruso), Springer, Berlin/Heidelberg, Germany **2010**, Ch. 40; c) E. Rideau, R. Dimova, P. Schwille, F. R. Wurm, K. Landfester, *Chem. Soc. Rev.* **2018**, *47*, 8572.
- [11] a) H. Bermúdez, D. A. Hammer, D. E. Discher, *Langmuir* **2004**, *20*, 540; b) R. Dimova, U. Seifert, B. Pouligny, S. Förster, H. G. Döbereiner, *Eur. Phys. J. E: Soft Matter Biol. Phys.* **2002**, *7*, 241.
- [12] a) F. Ite, M. Chami, A. Najer, S. Lörcher, D. Wu, I. A. Dinu, W. Meier, *Macromolecules* **2014**, *47*, 7588; b) A. Mecke, C. Dittrich, W. Meier, *Soft Matter* **2006**, *2*, 751; c) F. Ite, A. Najer, C. G. Palivan, W. Meier, *Nano Lett.* **2015**, *15*, 3871; d) G. Srinivas, D. E. Discher, M. L. Klein, *Nano Lett.* **2005**, *5*, 2343.
- [13] a) L. Otrin, A. Witkowska, N. Marušič, Z. Zhao, R. B. Lira, F. L. Kyrilis, F. Hamdi, I. Ivanov, R. Lipowsky, P. L. Kastritis, R. Dimova, K. Sundmacher, R. Jahn, T. Vidaković-Koch, *Nat. Commun.* **2021**, *12*, 4972; b) N. Marušič, L. Otrin, Z. Zhao, R. B. Lira, F. L. Kyrilis, F. Hamdi, P. L. Kastritis, T. Vidaković-Koch, I. Ivanov, K. Sundmacher, R. Dimova, *Proc. Natl. Acad. Sci. USA* **2020**, *117*, 15006; c) M. Chemin, P.-M. Brun, S. Lecommandoux, O. Sandre, J.-F. L. Meins, *Soft Matter* **2012**, *8*, 2867; d) N. Marušič, L. Otrin, J. Rauchhaus, Z. Zhao, F. L. Kyrilis, F. Hamdi, P. L. Kastritis, R. Dimova, I. Ivanov, K. Sundmacher, *Proc. Natl. Acad. Sci. USA* **2022**, *119*, e2122468119.
- [14] T. P. T. Dao, A. Brûlet, F. Fernandes, M. Er-Rafik, K. Ferji, R. Schweins, J. P. Chapel, A. Fedorov, M. Schmutz, M. Prieto, O. Sandre, J. F. Le Meins, *Langmuir* **2017**, *33*, 1705.
- [15] A. M. Wagner, J. Quandt, D. Söder, M. Garay-Sarmiento, A. Joseph, V. S. Petrovskii, L. Witzdam, T. Hammoor, P. Steitz, T. Haraszti, I. I. Potemkin, N. Y. Kostina, A. Herrmann, C. Rodriguez-Emmenegger, *Adv. Sci.* **2022**, *9*, 2200617.
- [16] a) V. Percec, D. A. Wilson, P. Leowanawat, C. J. Wilson, A. D. Hughes, M. S. Kaucher, D. A. Hammer, D. H. Levine, A. J. Kim, F. S. Bates, K. P. Davis, T. P. Lodge, M. L. Klein, R. H. DeVane, E. Aqad, B. M. Rosen, A. O. Argintaru, M. J. Sienkowska, K. Rissanen, S. Nummelin, J. Ropponen, *Science* **2010**, *328*, 1009; b) S. E. Sherman, Q. Xiao, V. Percec, *Chem. Rev.* **2017**, *117*, 6538.
- [17] a) D. Zhang, E. N. Atochina-Vasserman, D. S. Maurya, N. Huang, Q. Xiao, N. Ona, M. Liu, H. Shahnavaz, H. Ni, K. Kim, M. M. Billingsley, D. J. Pochan, M. J. Mitchell, D. Weissman, V. Percec, *J. Am. Chem. Soc.* **2021**, *143*, 12315; b) Q. Xiao, S. S. Yadavalli, S. Zhang, S. E. Sherman, E. Fiorin, L. da Silva, D. A. Wilson, D. A. Hammer, S. Andre, H. J. Gabius, M. L. Klein, M. Goulian, V. Percec, *Proc. Natl. Acad. Sci. USA* **2016**, *113*, E1134; c) S. S. Yadavalli, Q. Xiao, S. E. Sherman, W. D. Hasley, M. L. Klein, M. Goulian, V. Percec, *Proc. Natl. Acad. Sci. USA* **2019**, *116*, 744.
- [18] a) N. Yu. Kostina, D. Söder, T. Haraszti, Q. Xiao, K. Rahimi, B. E. Partridge, M. L. Klein, V. Percec, C. Rodriguez-Emmenegger, *Angew. Chem., Int. Ed.* **2021**, *60*, 8352; b) C. Rodriguez-Emmenegger, Q. Xiao, N. Y. Kostina, S. E. Sherman, K. Rahimi,

- B. E. Partridge, S. Li, D. Sahoo, A. M. Reveron Perez, I. Buzzacchera, H. Han, M. Kerzner, I. Malhotra, M. Moller, C. J. Wilson, M. C. Good, M. Goulian, T. Baumgart, M. L. Klein, V. Percec, *Proc. Natl. Acad. Sci. USA* **2019**, *116*, 5376; c) N. Y. Kostina, A. M. Wagner, T. Haraszti, K. Rahimi, Q. Xiao, M. L. Klein, V. Percec, C. Rodriguez-Emmenegger, *Soft Matter* **2021**, *17*, 254.
- [19] S. Zhang, H.-J. Sun, A. D. Hughes, B. Draghici, J. Lejnieks, P. Leowanawat, A. Bertin, L. Otero De Leon, O. V. Kulikov, Y. Chen, D. J. Pochan, P. A. Heiney, V. Percec, *ACS Nano* **2014**, *8*, 1554.
- [20] a) M. Peterca, V. Percec, P. Leowanawat, A. Bertin, *J. Am. Chem. Soc.* **2011**, *133*, 20507; b) I. Buzzacchera, Q. Xiao, H. Han, K. Rahimi, S. Li, N. Y. Kostina, B. J. Toebes, S. E. Wilner, M. Möller, C. Rodriguez-Emmenegger, T. Baumgart, D. A. Wilson, C. J. Wilson, M. L. Klein, V. Percec, *Biomacromolecules* **2019**, *20*, 712.
- [21] a) R. Dimova, C. M. Marques, *The Giant Vesicle Book*, CRC Press, Boca Raton, FL, USA **2019**; b) R. Dimova, *Annu. Rev. Biophys.* **2019**, *48*, 93.
- [22] K. Mitra, I. Ubarretxena-Belandia, T. Taguchi, G. Warren, D. M. Engelman, *Proc. Natl. Acad. Sci. USA* **2004**, *101*, 4083.
- [23] a) R. S. Gracià, N. Bezlyepkina, R. L. Knorr, R. Lipowsky, R. Dimova, *Soft Matter* **2010**, *6*, 1472; b) H. A. Faizi, S. L. Frey, J. Steinkühler, R. Dimova, P. M. Vlahovska, *Soft Matter* **2019**, *15*, 6006; c) H. A. Faizi, C. J. Reeves, V. N. Georgiev, P. M. Vlahovska, R. Dimova, *Soft Matter* **2020**, *16*, 8996.
- [24] a) N. Kučerka, Y. Liu, N. Chu, H. I. Petrache, S. Tristram-Nagle, J. F. Nagle, *Biophys. J.* **2005**, *88*, 2626; b) N. Kučerka, S. Tristram-Nagle, J. F. Nagle, *J. Membr. Biol.* **2006**, *208*, 193.
- [25] J. Pécréaux, H. G. Döbereiner, J. Prost, J. F. Joanny, P. Bassereau, *Eur. Phys. J. E: Soft Matter Biol. Phys.* **2004**, *13*, 277.
- [26] J. C. M. Lee, M. Santore, F. S. Bates, D. E. Discher, *Macromolecules* **2002**, *35*, 323.
- [27] F. Brochard-Wyart, P. G. De Gennes, O. Sandre, *Phys. A* **2000**, *278*, 32.
- [28] K. A. Riske, R. Dimova, *Biophys. J.* **2005**, *88*, 1143.
- [29] a) T. Portet, R. Dimova, *Biophys. J.* **2010**, *99*, 3264; b) R. B. Lira, F. S. C. Leomil, R. J. Melo, K. A. Riske, R. Dimova, *Adv. Sci.* **2021**, *8*, 2004068; c) F. S. C. Leomil, M. Zoccoler, R. Dimova, K. A. Riske, *Bioinf. Adv.* **2021**, *1*, vbab037.
- [30] A. M. Wagner, H. Eto, A. Joseph, S. Kohyama, T. Haraszti, R. A. Zamora, M. Vorobii, M. I. Giannotti, P. Schwille, C. Rodriguez-Emmenegger, *Adv. Mater.* **2022**, *34*, 2202364.
- [31] Q. Xiao, S. Zhang, Z. Wang, S. E. Sherman, R.-O. Moussodia, M. Peterca, A. Muncan, D. R. Williams, D. A. Hammer, S. Vértesy, S. André, H.-J. Gadius, M. L. Klein, V. Percec, *Proc. Natl. Acad. Sci. USA* **2016**, *113*, 1162.
- [32] L. A. Bagatolli, *Biochim. Biophys. Acta, Biomembr.* **2006**, *1758*, 1541.
- [33] L. A. Bagatolli, E. Gratton, *Biophys. J.* **2000**, *79*, 434.
- [34] a) C. Rodriguez Emmenegger, E. Brynda, T. Riedel, Z. Sedlakova, M. Houska, A. B. Alles, *Langmuir* **2009**, *25*, 6328; b) K. Ishihara, N. P. Ziats, B. P. Tierney, N. Nakabayashi, J. M. Anderson, *J. Biomed. Mater. Res.* **1991**, *25*, 1397; c) K. Ishihara, H. Nomura, T. Mihara, K. Kurita, Y. Iwasaki, N. Nakabayashi, *J. Biomed. Mater. Res.* **1998**, *39*, 323.
- [35] R. Jahn, T. Lang, T. C. Südhof, *Cell* **2003**, *112*, 519.
- [36] R. B. Lira, T. Robinson, R. Dimova, K. A. Riske, *Biophys. J.* **2019**, *116*, 79.
- [37] R. B. Lira, R. Dimova, in *Advances in Biomembranes and Lipid Self-Assembly*, Vol. 30 (Ed: R. Lipowsky), Academic Press, San Diego, CA, USA **2019**, pp. 229–270.
- [38] a) D. P. Siegel, *Biophys. J.* **1984**, *45*, 399; b) H. Ellens, D. P. Siegel, D. Alford, P. L. Yeagle, L. Boni, L. J. Lis, P. J. Quinn, J. Bentz, *Biochemistry* **1989**, *28*, 3692; c) P. R. Cullis, M. J. Hope, *Nature* **1978**, *271*, 672.
- [39] E. Lauga, T. R. Powers, *Rep. Prog. Phys.* **2009**, *72*, 096601.
- [40] L. Wang, S. Song, J. Hest, L. K. E. A. Abdelmohsen, X. Huang, S. Sánchez, *Small* **2020**, *16*, 1907680.
- [41] T. Patiño, X. Arqué, R. Mestre, L. Palacios, S. Sánchez, *Acc. Chem. Res.* **2018**, *51*, 2662.
- [42] W. S. Jang, H. J. Kim, C. Gao, D. Lee, D. A. Hammer, *Small* **2018**, *14*, 1801715.
- [43] S. Mann, *Acc. Chem. Res.* **2012**, *45*, 2131.
- [44] E. A. Veal, A. M. Day, B. A. Morgan, *Mol. Cell* **2007**, *26*, 1.
- [45] a) N. Patsoukis, I. Papapostolou, C. D. Georgiou, *Anal. Bioanal. Chem.* **2005**, *381*, 1065; b) J. Zielonka, S. Srinivasan, M. Hardy, O. Ouari, M. Lopez, J. Vasquez-Vivar, N. G. Avadhani, B. Kalyanaram, *Free Radical Biol. Med.* **2008**, *44*, 835.

# ADVANCED MATERIALS

## Supporting Information

for *Adv. Mater.*, DOI: 10.1002/adma.202206288

Zwitterionic Dendrimersomes: A Closer Xenobiotic Mimic  
of Cell Membranes

*Anton Joseph, Anna M. Wagner, Manuela Garay-Sarmiento, Mina Aleksanyan, Tamás Haraszti, Dominik Söder, Vasil N. Georgiev, Rumiana Dimova, Virgil Percec, and Cesar Rodriguez-Emmenegger\**

1 Supporting Information

2

3 **Zwitterionic dendrimersomes: a closer xenobiotic mimic of cell membranes**

4 *Anton Joseph, Anna M. Wagner, Manuela Garay-Sarmiento, Mina Aleksanyan, Tamás*  
5 *Haraszti, Dominik Söder, Vasil N. Georgiev, Rumiana Dimova, Virgil Percec and Cesar*  
6 *Rodriguez-Emmenegger\**

7

8 A. Joseph, A. M. Wagner, M. Garay-Sarmiento, Dr. T. Haraszti, D. Söder, Prof. C.

9 Rodriguez-Emmenegger

10 DWI – Leibniz Institute for Interactive Materials, Forckenbeckstraße 50, 52074 Aachen,  
11 Germany

12 E-mail: rodriguez@dwirwth-aachen.de

13

14 A. Joseph, A. M. Wagner, Dr. T. Haraszti, D. Söder

15 Institute of Technical and Macromolecular Chemistry, RWTH Aachen University,

16 Worringerweg 2, 52074 Aachen, Germany

17

18 M. Garay-Sarmiento

19 Chair of Biotechnology, RWTH Aachen University, Worringerweg 3, 52074 Aachen,

20 Germany

21

22 M. Aleksanyan

23 Institute for Chemistry and Biochemistry, Freie Universität Berlin, Takustraße 3, 14195

24 Berlin, Germany

25

26 M. Aleksanyan, Dr. V. N. Georgiev, Dr. R. Dimova

27 Max Planck Institute of Colloids and Interfaces, Science Park Golm, 14476 Potsdam,

28 Germany

29

30 Prof. V. Percec

31 Roy & Diana Vagelos Laboratories, Department of Chemistry, University of Pennsylvania,

32 19104-6323 Philadelphia, Pennsylvania, United States of America

33

34

35 Prof. C. Rodriguez-Emmenegger  
36 Institute for Bioengineering of Catalonia (IBEC), The Barcelona Institute of Science and  
37 Technology (BIST), Carrer de Baldiri Reixac 10-12, 08028 Barcelona, Spain.  
38 E-mail: crodriguez@ibecbarcelona.eu  
39  
40 Prof. C. Rodriguez-Emmenegger  
41 Institució Catalana de Recerca i Estudis Avançats (ICREA), Passeig Lluís Companys 23,  
42 08028 Barcelona, Spain  
43

44	<b>Table of Contents</b>	
45	1. Materials.....	4
46	2. Methods.....	4
47	3. Synthesis and molecular characterization .....	18
48	4. Supplementary Results .....	22
49	4.1 NMR characterization of JD <sup>PC</sup> .....	22
50	4.2 NMR characterization of JD <sup>cat</sup> .....	24
51	4.3 Long-term stability studies of bulk JD <sup>PC</sup> and z-DSs .....	26
52	4.4 Stability of z-DSs under shear stress.....	28
53	4.5 Thermal stability of single-single and twin-twin dendrimersomes.....	30
54	4.6 Differential Scanning Calorimetry .....	32
55	4.7 Analysis of distribution of size .....	32
56	4.8 Analysis of bilayer thickness by AFM.....	33
57	4.9 Analysis of bilayer thickness by cryo-TEM.....	34
58	4.10 Micropipette aspiration studies .....	35
59	4.11 Analysis of membrane fluctuations.....	35
60	4.12 Electroporation.....	37
61	4.13 Lipid-JD <sup>PC</sup> hybrids .....	37
62	4.14 Formation of raft-like microdomains .....	38
63	4.15 Interaction with biological media .....	41
64	4.15.1 Interactions of z-DSs and Normal Human Dermal Fibroblasts (NHDF).....	41
65	4.15.1 DLS investigation of z-DSs compatibility in protein solutions .....	42
66	4.15.2 Compatibility of z-DSs prepared in 10 mM HEPES buffer with protein solutions	
67	44	
68	4.15.3 Compatibility of z-DSs prepared in 300 mM sucrose with protein solutions....	46
69	4.15.4 Interactions of z-DSs and fluorescently labeled BSA .....	48
70	4.16 Fusion with liposomes .....	50
71	4.16.1 Fusion of charged giant z-DSs with charged liposomes .....	51
72	4.16.2 Fusion of charged giant z-DSs with neutral liposomes.....	54
73	4.16.3 Fusion of neutral giant z-DSs with neutral or negatively charged liposomes....	56
74	4.16.4 Fusion of Small Unilamellar Vesicles (SUVs) by DLS .....	57
75	4.17 Motility of z-DSs .....	59
76	4.18 Biosensing of hydrogen peroxide .....	60
77	5. References .....	62
78		

## 1. Materials

All materials were used as received or otherwise stated. Methyl 3,5-dihydroxybenzoate was obtained from abcr, Germany. 1-Bromododecane, 2-Chloro-2-oxo-1,3,2-dioxaphospholane, Et<sub>3</sub>N and 2.0M Me<sub>3</sub>N solution in MeCN were received from TCI Europe, Belgium. Et<sub>3</sub>N was distilled and dried over 20% w/v activated molecular sieve (3 Å, Type 564, Carl Roth, Germany) for two days prior to use. The NMe<sub>3</sub> solution was dried over the same activated molecular sieve (20% w/v) for two days prior to use. The anhydrous solvents DMF, THF, EtOH and MeOH (stored over molecular sieve) were purchased from Acros Organics, Belgium. Prior to use as solvents for amphiphiles or fluorescent labels, these solvents were filtered through 0.2 µm syringe filters. CH<sub>2</sub>Cl<sub>2</sub>, EtOAc, anhydrous K<sub>2</sub>CO<sub>3</sub>, MgSO<sub>4</sub>, NaHCO<sub>3</sub>, Na<sub>2</sub>SO<sub>4</sub> as well as HPLC-grade solvents CHCl<sub>3</sub>, MeOH and H<sub>2</sub>O, used in flash column chromatography of JD<sup>PC</sup>, were purchased from VWR, Germany. Aluminum oxide (90, basic, 0.063-0.2 mm) was purchased from Carl Roth. Human blood plasma, 1.0 M LiAlH<sub>4</sub> solution in THF, Nile red, calcein, Laurdan, α-hemolysin, Bodipy and CoCl<sub>2</sub>·6H<sub>2</sub>O and Triton X-100 were purchased from Sigma-Aldrich, Germany. Fluorescently labeled BSA (Texas Red) was purchased from Fisher Scientific. HEPES was supplied by PenReac AppliChem, Germany. The following lipids were purchased from Avanti Polar Lipids, USA: 12:0 PC (DLPC) 1,2-dilauroyl-sn-glycero-3-phosphocholine; 16:0 PC (DPPC) 1,2-dipalmitoyl-sn-glycero-3-phosphocholine; 18:0 PC (DSPC), 1,2-distearoyl-sn-glycero-3-phosphocholine; 16:0 NBD PE, 1,2-dipalmitoyl-sn-glycero-3-phosphoethanolamine-N-(7-nitro-2-1,3-benzoxadiazol-4-yl) (ammonium salt); 14:0-06:0 NBD PC, 1-myristoyl-2-{6-[(7-nitro-2-1,3-benzoxadiazol-4-yl)amino]hexanoyl}-sn-glycero-3-phosphocholine. 16:0 Liss Rhod PE (1,2-dipalmitoyl-sn-glycero-3-phosphoethanolamine-N-(lissamine rhodamine B sulfonyl) (ammonium salt)). Atto 633 DOPE was purchased from Sigma Aldrich. All syntheses were performed in flame-dried flasks under a nitrogen atmosphere in anhydrous solvents using standard Schlenk techniques.

## 2. Methods

*NMR spectra* were recorded at room temperature using a Bruker Avance III 400 MHz spectrometer. Recorded spectra were analysed using the MestReNova V.12.0.1 software. Chemical shifts are reported relative to the solvent residual peak (CDCl<sub>3</sub>, δ<sub>H</sub> = 7.26 ppm, δ<sub>C</sub> = 77.16 ppm).<sup>[1]</sup> For <sup>31</sup>P-NMR spectra absolute referencing in relation to the <sup>1</sup>H-NMR spectra was performed using the MestReNova software. The following abbreviations were used throughout: s = singlet, d = doublet, t = triplet, q = quartet, etc., m = multiplet. Coupling constants (*J*) are given in Hz.

113 *High-resolution electron spray ionization mass spectra (HR-ESI-MS)* were recorded using a  
114 micrOTOF-QII instrument from Bruker Daltonik (Billerica, Massachusetts).

115  
116 *Flash column chromatography* was conducted using Silica gel 60 (0.04 – 0.063 mm) from Carl  
117 Roth. Thin-layer chromatography (TLC) was carried out on Macherey-Nagel ALUGRAM Xtra  
118 SIL G/UV F<sub>254</sub> plates. Visualization was achieved by UV irradiation (254 nm) or staining with  
119 basic KMNO<sub>4</sub> solution.

120  
121 *High-performance liquid chromatography* was performed using an Agilent-1260-system  
122 equipped with a degaser, quad-pump, autosampler, oven, diode-array detector and an ELS-  
123 detector (type: SofTa 1300). An VDSpher®-C18-E column (4.0 x 250 mm, 5 μm, 100 Å, VDS-  
124 Optilab) was applied at a flow rate of 1.0 mL·min<sup>-1</sup> at 35 °C. Inject volume for samples and  
125 references were 10 μL. References and samples were dissolved in Eluent Methanol (HPLC  
126 grade, VWR):Chloroform (HPLC grade, VWR) in ratio 75:25. The measurements were run  
127 isocratic. Results were evaluated using the PSS WinGPC UniChrom software (Version 8.3.2).

128  
129 **Vesicle preparation**

130 *Thin-film hydration method*, also referred to as spontaneous swelling method,<sup>[2]</sup> was performed  
131 as follows: Amphiphiles were dissolved in CHCl<sub>3</sub> ( $c = 10 \text{ mg}\cdot\text{mL}^{-1}$ ). For co-assemblies, the  
132 respective amphiphile stock solutions were mixed in the reported molar ratios. For samples  
133 used in confocal microscopy measurements, stock solutions of Bodipy, Nile red  
134 ( $c = 0.2 \text{ mg}\cdot\text{mL}^{-1}$  in THF), Laurdan ( $c = 0.2 \text{ mg}\cdot\text{mL}^{-1}$  in CHCl<sub>3</sub>) or fluorescently labelled lipid  
135 ( $c = 1 \text{ mg}\cdot\text{mL}^{-1}$  in CHCl<sub>3</sub>) were added in the specified molar ratio relative to the amount of  
136 amphiphile. After deposition of the mixtures from Table S1 and Table S2 on a roughened Teflon  
137 plate, the solvent was left to evaporate under ambient conditions for 30 minutes. The Teflon  
138 plates were transferred into a vial and dried *in vacuo* for 1 h. 300 μL of an appropriate aqueous  
139 medium for the respective experiment was added onto the dry amphiphile film, so that the  
140 Teflon plate was completely covered and then left in the oven for hydration at 60 °C for 12 h.  
141 This temperature is above the main phase transition temperature of all amphiphiles used in the  
142 herein reported studies. The method yields vesicle dispersions with an amphiphile  
143 concentration of  $c_{\text{amphiphile}} = 1 \text{ mg}\cdot\text{mL}^{-1}$ .

144 In the following Tables S1–S5, we denote  $n$  as the molar percentage of each component,  $c_{\text{stock}}$   
145 as the stock concentration of amphiphiles in organic solvent used for the deposition onto the  
146 Teflon plate and  $V_{\text{stock}}$  as the exact volume that is deposited for each coassembly.

147 **Table S1.** Mixing protocol during labeling of z-DS membrane with fluorescent dyes. Each  
 148 sample was rehydrated with 300  $\mu\text{L}$  of Milli-Q water or buffer solution.

	<b>JD<sup>PC</sup></b>	<b>Bodipy</b>	<b>JD<sup>PC</sup></b>	<b>Nile red</b>	<b>JD<sup>PC</sup></b>	<b>Laurdan</b>
<b>n (mol%)</b>	99.5	0.5	99.5	0.5	99.5	0.5
<b>c<sub>stock</sub> (mg·mL<sup>-1</sup>)</b>	10	0.2	10	0.2	10	0.2
<b>V<sub>stock</sub> (<math>\mu\text{L}</math>)</b>	30.0	3.1	30.0	3.7	30.0	4.1

149  
 150 **Table S2.** Mixing protocol during labeling of z-DS membrane with fluorescent lipids. Each  
 151 sample was rehydrated with 300  $\mu\text{L}$  of Milli-Q water or buffer solution.

	<b>JD<sup>PC</sup></b>	<b>Rh-PE</b>	<b>JD<sup>PC</sup></b>	<b>Rh-PE</b>	<b>JD<sup>PC</sup></b>	<b>Rh-PE</b>	<b>JD<sup>PC</sup></b>	<b>NBD- PC</b>
<b>n (mol%)</b>	99.9	0.1	99	1	90	10	99	1
<b>c<sub>stock</sub> (mg·mL<sup>-1</sup>)</b>	10	1	10	1	10	1	10	1
<b>V<sub>stock</sub> (<math>\mu\text{L}</math>)</b>	29.9	0.6	29.4	5.8	24.7	53.4	29.7	3.5

152  
 153 *Electroformation method* was performed as follows: A stock solution of JD<sup>PC</sup> in CHCl<sub>3</sub>  
 154 (5 mg·mL<sup>-1</sup>) was prepared and mixed with stock solutions of Nile red ( $c = 0.2 \text{ mg}\cdot\text{mL}^{-1}$  in THF),  
 155 Laurdan ( $c = 0.2 \text{ mg}\cdot\text{mL}^{-1}$  in CHCl<sub>3</sub>), fluorescently labeled lipid ( $c = 1 \text{ mg}\cdot\text{mL}^{-1}$  in CHCl<sub>3</sub>) or  
 156 DliC<sub>18</sub> (1 mg·mL<sup>-1</sup> in CHCl<sub>3</sub>) in the specified molar ratio relative to the amount of amphiphile.  
 157 A total of 14  $\mu\text{L}$  stock solution was spread as a thin film on two conductive ITO-coated glasses  
 158 (ITO film thickness <100 nm, resistance 50  $\Omega$ ; Präzisions Glas & Optik, Iserlohn, Germany).  
 159 The glasses were dried *in vacuo* for 1 h at room temperature. A 1.8 mL chamber was prepared  
 160 by placing a Teflon spacer between the two glasses which was then filled with an appropriate  
 161 aqueous medium for the respective experiments. Using a function generator, an effective  
 162 sinusoidal voltage of 10 Hz and 1.05 mV root mean square (measured at the ITO-coated  
 163 glasses) was applied for 1 h at room temperature. For each experiment the vesicles were  
 164 immediately used within a day. The method yields vesicle dispersions with an amphiphile  
 165 concentration of  $c_{\text{amphiphile}} = 0.039 \text{ mg}\cdot\text{mL}^{-1}$ .

166  
 167 *Injection method* was performed as follows: 50  $\mu\text{L}$  of an amphiphile solution in ethanol was  
 168 injected into 1 mL Milli-Q water or buffer and vortexed for 5 seconds. In order to vary the final  
 169 amphiphile concentration, the stock solution concentration was varied while the injected  
 170 volume and the volume of water remained constant. The samples were left uncovered overnight

171 to allow for evaporation of ethanol. The method yields vesicle dispersions with an amphiphile  
172 concentration of  $c_{\text{amphiphile}} = 0.06 - 2 \text{ mg}\cdot\text{mL}^{-1}$ .

173

174 *Extrusion.* Vesicles were formed by thin-film hydration and then subjected to 11 cycles of  
175 extrusion through polycarbonate membranes with a 100 nm pore diameter using the Avanti  
176 Mini-Extruder (Avanti Polar Lipids, USA).

177

### 178 **Vesicle characterization**

179 *Confocal Laser Scanning Microscopy (CLSM)* was performed on a Leica TCS SP8 confocal  
180 microscope (Wetzlar, Germany) using a 63x/1.40 glycerol-immersion objective and a PMT or  
181 HyD detector. Images were recorded at a resolution of 1024x1024 px and videos at 512x512 px  
182 at a scanning speed of 600 Hz. Unless otherwise noted, measurements were performed at 22 °C.  
183 The observation chamber was prepared by depositing a vesicle dispersion between two high  
184 precision microscope cover glasses ( $170 \pm 5 \mu\text{m}$ ) that were sealed with Secure-Seal<sup>TM</sup> spacers  
185 (diameter = 13 mm, thickness = 0.12 mm). Fiji-ImageJ software was used to crop images and  
186 adjust contrast and brightness.

187

188 *Phase contrast microscopy* was performed on an inverted Axiovert 135 phase contrast  
189 microscope (Zeiss, Jena, Germany) equipped with an ultra-high-speed digital camera v2512  
190 (Phantom, Vision Research, New Jersey, USA). A mercury lamp HBO W/2 was used for the  
191 illumination of the samples and all the images were acquired with a 20x/0.4 Ph2 objective at  
192 acquisition speed of 20000 frames per second (fps). ImageJ (NIH, USA) software was used  
193 for the analysis of the images.

194

195 *Atomic force microscopy (AFM)* was performed on a Multimode Atomic Force Microscope  
196 NanoScope V (Digital Instruments) using OTESPA-R3 silicon probes (Bruker, France; tip  
197 radius = 7 nm, nominal spring constant =  $26 \text{ N}\cdot\text{m}^{-1}$ ). For the sample preparation, a diluted  
198 dispersion of JD<sup>PC</sup> DSs, prepared by thin-film hydration in water ( $c_{\text{diluted}} = 0.5 \text{ mg}\cdot\text{mL}^{-1}$ ), was  
199 drop casted on freshly peeled Mica and dried at ambient conditions at 22 °C and  $\approx 25 - 30\%$   
200 relative humidity. Images were recorded in air under ambient conditions as topological scans  
201 in tapping mode and analyzed using the Gwyddion software.<sup>[3]</sup>

202

203 *Cryogenic transmission electron microscopy (Cryo-TEM)* was performed on a Zeiss Libra<sup>TM</sup>  
204 120 transmission electron microscope (Oberkochen, Germany) in cryogenic mode. Images

205 ware recorded at  $-168\text{ }^{\circ}\text{C}$  with an applied electron beam acceleration voltage of 120 kV using  
206 an in-column Omega energy filter with a CCD detector. For the sample preparation, a JD<sup>PC</sup>  
207 dispersion ( $5\text{ }\mu\text{L}$ ,  $1\text{ mg}\cdot\text{mL}^{-1}$ ), prepared via the injection method, was deposited on plasma-  
208 treated lacey grids. After blotting, the sample was flash frozen in liquid ethane using a FEI  
209 Vitrobot (Model Mark IV) plunge freezing station. Afterwards, the samples were fixed on a  
210 Model 910 cryo transfer specimen holder from Gatan (Pleasanton, California).

211  
212 *Dynamic light scattering (DLS)* measurements were performed on a Zetasizer Ultra (Malvern  
213 Instrument, UK) using a laser wavelength of  $\lambda = 632.8\text{ nm}$  and a fixed scattering angle of  $174.4^{\circ}$   
214 (back scattering). 1 mL of vesicle dispersion prepared by the injection method or extrusion were  
215 transferred into DTS0012 disposable cuvettes and equilibrated at  $25\text{ }^{\circ}\text{C}$  for 90 s before each  
216 measurement. Data acquisition was performed in triplicate for each sample. Data processing  
217 was performed by the ZS XPLOER 1.2.0.91 software.

218  
219 *Fluorescence Activated Cell Sorting (FACS)*. Flow cytometry measurements were performed  
220 on a MoFlo Astrios EQs Sorter (Beckman Coulter, US) with  $1.5\cdot 10^3$  events per sample. The  
221 fluorescence of calcein was excited at 488 nm and detected within the range of 513 – 526 nm.  
222 For quantification, median fluorescence intensity was analyzed with the FlowJo software (Tree  
223 Star, Inc., USA).

224  
225 *Fluorescence Spectroscopy* was performed using a FluoroMax-4 Spectrofluorometer (Horiba  
226 Jobin Yvon GmbH, Germany) in a 3.5 mL high-precision quartz glass cuvette (Hellma  
227 Analytics, optical path length 10x10 mm.).

## 228 229 **Characterization of z-dendrimersome properties**

230 *Fluorescence recovery after photobleaching (FRAP)*. FRAP experiments were performed to  
231 determine the diffusion coefficient of a fluorescently labeled lipid (Liss Rhod-PE) in supported  
232 bilayers formed from JD<sup>PC</sup> or lipids, respectively. Small unilamellar vesicles (SUVs) were  
233 prepared by dissolving JD<sup>PC</sup> and lipids in  $\text{CHCl}_3$  ( $c = 10\text{ mg mL}^{-1}$ ) and mixing with Liss Rhod-  
234 PE lipid (0.01 mol%). 80  $\mu\text{L}$  of the mixed solutions were transferred into 1 mL vials. The  
235 solvent was evaporated under a nitrogen stream and afterwards under high vacuum for 1 h.  
236 Afterwards, JD<sup>PC</sup>/lipids were rehydrated in 200  $\mu\text{L}$  buffer (25 mM Tris-HCl pH 7.5, 150 mM  
237 KCl, 5 mM  $\text{MgCl}_2$ ) and vortexed for 20 s. The samples were sonicated for 30 min and diluted  
238 with hydration buffer to yield a SUV dispersion ( $c = 0.5\text{ mg mL}^{-1}$ ). A chamber was constructed

239 by first rinsing a glass coverslip with EtOH and water (3 times) and drying under a nitrogen  
 240 stream. Afterwards, a cut 0.5 mL Eppendorf tube was glued onto the glass slide using Norland  
 241 Optical Adhesive 61 (Norland Products Inc, USA) and cured by UV irradiation for 15 min. The  
 242 chambers were treated with air plasma (60 s, 0.2 mbar). Afterwards, the SUV dispersions  
 243 (50  $\mu$ L) were placed into their respective chambers and incubated for 3 min at 37  $^{\circ}$ C. The  
 244 supported bilayers were washed with a total of 2 mL buffer (25 mM Tris-HCl pH 7.5, 150 mM  
 245 KCl) to remove the vesicles that did not fuse.

246 FRAP analysis was based on a previously reported method by E. Miglioniri *et al.*<sup>[4]</sup> using a  
 247 custom-made Python script. 20 pre bleach frames (256x256 pixel) of the supported bilayer were  
 248 recorded at 1% attenuated laser power of a 561 nm laser in the bidirectional scan mode at a scan  
 249 speed of 1800 Hz with the pinhole at 1 Airy unit. Afterwards, bleaching was performed for 10  
 250 frames at 100% laser power by defining a circle with a nominal bleaching radius of  $r_n = 5.0 \mu\text{m}$ .  
 251 The fluorescence recovery was recorded for 500 post bleach frames at a laser power of 1%. To  
 252 compensate for any bleaching caused during the imaging, the background count (dark current,  
 253  $I_{bg}$ ) was subtracted from the data and normalized by using the intensity  $I_{ref}$  of a non-bleached  
 254 area at the edge of each frame. Equation 1 yields  $I_{rel}$  as for the relative intensity of a given point  
 255 in the image.

$$I_{rel} = \frac{I - I_{bg}}{I_0 - I_{bg}} \cdot \frac{I_{ref 0}}{I_{ref}} \quad (1)$$

256 In a homogeneous sample with constant concentration  $c_0(x,y)$ , the inverse relative intensity  
 257 profile  $(1 - I_{rel})$  follows the same diffusion law as  $c(t,x,y)$ . In Fourier space, we used the  
 258 diffusion equation with the spatial wave vector  $q_i$  ( $i = x,y$ ) as:

$$c(q_x, q_y, t) = c_0(q_x, q_y) \cdot e^{-4\pi^2(q_x^2 + q_y^2)Dt} \quad (2)$$

259 A home-written script in python was written to extract the time dependent bleaching data at  
 260 discrete wave vectors. Each curve was fitted individually, and then in merged form plotted as  
 261  $4\pi^2q^2t$  with  $a_0$  as the immobile fraction. This allowed to discard experiments with detected  
 262 spatial anisotropy in the data set. We obtained the diffusion coefficient independent of the  
 263 bleaching profile if the spatial variation of the original concentration was low in comparison to  
 264 that of the bleached area. Immobile fraction was determined as  $a_0/(a_0+c_0)$  from the fits.

265  
 266 *Differential scanning calorimetry (DSC)* was performed on a PerkinElmer DSC 8500 with a  
 267 nitrogen flow of 20 mL $\cdot$ min $^{-1}$  (sccm) and controlled by the Pyris 13.3.1.0014 software. Prior to  
 268 measurement, the JD<sup>PC</sup> sample was annealed at 60  $^{\circ}$ C at high vacuum for 2 h. Measurements  
 269 were performed using aluminium pans with covers (PerkinElmer) that were pierced with 3 holes.

270 The sample was annealed at 140 °C for 30 min and cooled to the starting temperature of -70 °C  
271 at 10 °C·min<sup>-1</sup> prior to the first heating cycle.

272  
273 *Contour analysis of vesicles.* We analyzed the undulations of z-DSs, liposomes and  
274 polymersomes by CLSM. Vesicles were prepared from JD<sup>PC</sup>, a lipid (DLPC) and a block-  
275 copolymer (poly(BD<sub>87</sub>-*b*-EO<sub>72</sub>) (BDEO) by thin-film hydration while labeling the membrane  
276 with 0.1 mol% Nile red, respectively. 16 µl of vesicle solution in water (1 mg·mL<sup>-1</sup>) was mixed  
277 with 4 µl of 10 mM HEPES to deflate the vesicles and allow the fluctuation. Images were taken  
278 in CLSM with a resolution of 512x512 pixels at a scan speed of 1000 Hz.

279  
280 *Fluctuation analysis* was performed according to a previously reported protocol.<sup>[5]</sup> GUVs  
281 composed of JD<sup>PC</sup>, POPC and DLPC were electroformed at 22 °C in sucrose (25 mM),  
282 respectively. The harvested vesicles were diluted in 27 mM glucose solution to obtain  
283 fluctuating vesicles. The low sugar concentration limited the influence of gravity on the vesicle  
284 shape as well as softening effects of sugars.<sup>[6]</sup> The vesicles were placed in a chamber made of  
285 two cover slips and a 2 mm-thick Teflon spacer. The GUVs were observed under phase-contrast  
286 mode on a Zeiss Axio Observer D1 microscope using a 40× Numerical Aperture (NA) 0.6 Ph2  
287 air objective. The equatorial fluctuations were acquired with a digital camera (pco.edge, PCO  
288 AG, Kelheim, Germany) at a frequency of 20 frames per second and an image exposure time  
289 of 200 µs, at room temperature (22 °C). 2500 images per vesicle were recorded.<sup>[5a]</sup>

290  
291 *Edge tension analysis* was performed according to previously reported protocols.<sup>[7]</sup> GUVs  
292 composed of JD<sup>PC</sup>, POPC and DLPC were electroformed at 22 °C in sucrose (200 mM), and 10  
293 times diluted with a solution of 200 mM glucose containing 0.1 mM NaCl. The electroporation  
294 chamber, (Eppendorf electrofusion chamber, Hamburg, Germany), contained a pair of parallel  
295 cylindrical electrodes with 92 µm radii and spaced by 500 µm distance from each other. The  
296 chamber was connected to a βtech pulse generator GHT\_Bi500 (βtech, l'Union, France) to  
297 apply square-wave direct current (DC) single pulse on each analyzed GUV (note that the  
298 chamber solution was exchanged after the application of a single pulse to avoid observation on  
299 preporated vesicles whose membrane might not have resealed properly). The pulse strength  
300 applied for DLPC, POPC and JD<sup>PC</sup> vesicles was 55, 60 and 75 V (1.1, 1.2 and 1.5 kV·cm<sup>-1</sup>),  
301 respectively. The pulse duration was 3 ms. Image processing and pore edge tension value for  
302 each GUV was calculated from the time dependence of pore closure detected and analyzed by  
303 using a lab developed software, PoET described in literature.<sup>[7b]</sup> The pore closure dynamics is

304 described by the hydrodynamic model reported earlier by Brochard-Wyart *et al.*<sup>[8]</sup> Membrane  
 305 pores were monitored through the fast camera for obtaining high temporal resolution and the  
 306 data were evaluated by the software PoET, measuring the pore radius,  $r$ , from every recorded  
 307 image. Pore dynamics were characterized by plotting the quantity,  $R^2 \ln(r)$  as a function of time,  
 308 where  $R$  is the GUV radius. Typical datasets for each different membrane composition are  
 309 shown in Figure S25. The regime of linear time dependence of  $R^2 \ln(r)$  correspond to the quasi-  
 310 static leakout regime and the edge tension  $\gamma$  is obtained from the slope  $\alpha$  of this dependence  
 311 using the equation of  $\gamma = -\left(\frac{3}{2}\right)\pi\eta\alpha$ , where  $\eta$  is the medium viscosity ( $0.89 \cdot 10^{-4}$  Pa·s for our  
 312 experimental conditions).

313  
 314 *Membrane permeability and thermal stability of liposomes and dendrimersomes.* For  
 315 observation in CLSM, JD<sup>PC</sup> DSs and liposomes (DLPC, POPC) were prepared by thin-film  
 316 hydration in an aqueous solution of calcein ( $c_{\text{amphiphiles}} = 1 \text{ mg}\cdot\text{mL}^{-1}$ ,  $c_{\text{calcein}} = 0.03 \text{ mg}\cdot\text{mL}^{-1}$ ,  
 317  $48 \text{ }\mu\text{M}$ ) and labeled with 0.1 mol% Nile red, respectively. For FACS analysis, vesicles were  
 318 prepared by injecting a JD<sup>PC</sup> or liposome solution ( $c_{\text{amphiphiles}} = 0.5 \text{ mg}\cdot\text{mL}^{-1}$ ) into an aqueous  
 319 solution of calcein. To quench the calcein fluorescence outside the vesicle lumen we added  
 320  $2 \text{ }\mu\text{L}$  of a  $\text{CoCl}_2 \cdot 6\text{H}_2\text{O}$  in water ( $c = 0.5 \text{ mg}\cdot\text{mL}^{-1}$ ,  $c_{\text{Co}^{2+}} = 13 \text{ }\mu\text{M}$ ) to  $300 \text{ }\mu\text{L}$  vesicle dispersion.  
 321 To assess the temperature stability,  $50 \text{ }\mu\text{l}$  of vesicle dispersion was heated to  $80 \text{ }^\circ\text{C}$  for 1 h using  
 322 a water bath. Vesicles were investigated by monitoring the fluorescence stemming from the  
 323 lumen (calcein) using CLSM while the object fluorescence intensity was monitored in  
 324 FACS before and after addition of  $\text{Co}^{2+}$ , and after heating.

325  
 326 *Effect of Shear stress on membrane stability.* z-DSs were prepared by electroformation in a  
 327  $200 \text{ mM}$  sucrose and calcein ( $c = 0.03 \text{ mg}\cdot\text{mL}^{-1}$ ) solution while the membrane was labeled with  
 328  $0.5 \text{ mol}\%$  Nile red. To evaluate the effect of shear stress on the stability of z-DSs, the vesicles  
 329 were pumped through a flow cell (flow channel height =  $100 \text{ }\mu\text{m}$ , width =  $1.98 \text{ mm}$ , hydraulic  
 330 diameter =  $190 \text{ }\mu\text{m}$ ) at  $25 \text{ }^\circ\text{C}$ . The flow speed was varied between  $300 - 500 \text{ }\mu\text{L}\cdot\text{min}^{-1}$  using a  
 331 peristaltic pump. By assuming the flow cell as a rectangular duct, the resulting wall shear stress  
 332  $\tau_w$  was calculated according to the following analytical expression:

$$333 \quad \tau_w = \frac{6 \mu Q}{w h^2}$$

334  $\mu$  is the dynamic viscosity of the solution ( $0.97 \text{ mPa}\cdot\text{s}$  for  $0.2 \text{ M}$  sucrose<sup>[9]</sup>),  $Q$  is the flow rate,  
 335 while  $w$  and  $h$  are the width and the height of the flow cell, respectively.<sup>[10]</sup> The calculated wall

336 shear stresses ranged between 1.47 and 2.45 Pa. Within the given parameters the Reynolds  
 337 numbers are  $< 9$ , indicating a constant laminar flow.<sup>[11]</sup>

338  
 339 *Generalized polarization analysis by Laurdan.* The formation of raft-like microdomains was  
 340 studied by co-assembling JD<sup>PC</sup> with lipids of varying chain length, ranging from DLPC (C12)  
 341 to DSPC (C18). The vesicles were prepared by thin-film hydration by labeling the membrane  
 342 with 1 mol% Laurdan, according to the following Table S3:

343  
 344 **Table S3.** Mixing protocol for co-assemblies used in the generalized polarization. Each sample  
 345 was rehydrated with 300  $\mu$ L of Milli-Q water.

	JD <sup>PC</sup>	DLPC	Laurdan	JD <sup>PC</sup>	DPPC	Laurdan	JD <sup>PC</sup>	DSPC	Laurdan
<b>n (mol%)</b>	79.2	19.8	1	79.2	19.8	1	79.2	19.8	1
<b>c<sub>stock</sub> (mg·mL<sup>-1</sup>)</b>	10	10	0.2	10	10	0.2	10	10	0.2
<b>V<sub>stock</sub> (<math>\mu</math>L)</b>	24.2	5.8	8.3	23.3	6.8	8.1	22.9	7.3	8.0

346  
 347 *Interaction with proteins* was studied by CLSM and DLS. For CLSM, z-DSs were formed by  
 348 thin-film hydration in 10 mM HEPES buffer or by electroformation in 300 mM sucrose. In both  
 349 cases the membrane was labeled using Bodipy (0.5 mol%) as fluorescent dye. The vesicle  
 350 dispersion was mixed in 1:1 v:v ratio with 100  $\mu$ M solutions of BSA and lysozyme, respectively,  
 351 as well as 10% and 100% human blood plasma. For studies where vesicles were formed in  
 352 10 mM HEPES, the BSA, lysozyme and 10% blood plasma solution were prepared in the same  
 353 buffer. When investigated vesicles were formed in 300 mM sucrose, the protein solutions were  
 354 prepared in 300 mM glucose. The mixtures were incubated for 30 min and 24 h prior to  
 355 observation by CLSM. For DLS studies, the z-DSs were prepared by injection method into  
 356 10 mM HEPES buffer using a final amphiphile concentration of 1 mg·mL<sup>-1</sup>. The utilized vesicle  
 357 dispersions were measured prior to incubation with the respective protein solutions. The vesicle  
 358 dispersions were mixed in a 1:1 v:v ratio with 100  $\mu$ M solutions of BSA and lysozyme (10 mM  
 359 HEPES buffer), respectively, as well as 10% human blood plasma (in 10 mM HEPES buffer).  
 360 The vesicles were incubated for 30 min and subsequently 24 h prior to the measurements.

361  
 362 *Cultivation of cells.* HeLa and Caco-2 cells were cultured in Dulbecco's Modified Eagle  
 363 Medium (DMEM, Gibco<sup>TM</sup>) supplemented with 10% fetal bovine serum (FBS) and 1%  
 364 pen/strep (AntibioticAntimycotic (100X) Gibco®). H441 Cells (ATCC) were cultured in  
 365 Roswell Park Memorial Institute growth medium (RPMI-1640, Gibco<sup>TM</sup>) containing 10% FBS.

366 Cultivation was carried out at 37°C and in humidified 5% CO<sub>2</sub> atmosphere. For the cytotoxicity  
367 assay, cells were seeded at a density of 20.000 cells per well in 96-well plates.

368  
369 *Cytotoxicity assay.* Cytotoxicity was assessed by determining cell viability using the MTS assay  
370 (The CellTiter 96® Aqueous One Solution Cell Proliferation Assay, Promega) after 24 h of  
371 incubation. Briefly, z-DSs were prepared in water by the thin-film hydration method with a  
372 final amphiphile concentration of 1 mg·mL<sup>-1</sup>. Subsequently, vesicles were sterilized by UV  
373 disinfection (254 nm) for 1 h. Then, 30 µL of vesicle solution was mixed with 70 µL of cell  
374 culture medium and added to each well. Incubation was carried out for 24 h at 37°C and in a  
375 humidified atmosphere with 5% CO<sub>2</sub>. 70 µL culture medium mixed with 30 µL Milli-Q water  
376 served as a negative control. For the MTS assay, the vesicle medium in each well was  
377 exchanged for 20 µL of MTS reagent mixed with 100 µL of cell culture medium. The  
378 microplates were allowed to incubate for 3 h and absorbance was recorded at 490 nm using the  
379 SpectraMax® M3 multimode microplate reader. The collected absorbance data were  
380 normalized, and the negative control was set as 100% reference.

381  
382 *Uptake of vesicles by cells.* Normal human dermal fibroblasts (NHDF) were cultured in DMEM  
383 with 10% FBS until passage 8. Upon harvesting with trypsin treatment cells were transferred  
384 to a 96-well plate at 70.000 cells/well in 100 µL DMEM with FBS. After 24 h, the medium was  
385 removed. z-DSs were prepared by thin film rehydration in Milli-Q water ( $c = 1 \text{ mg}\cdot\text{mL}^{-1}$ ) and  
386 the membrane was labeled with 1 mol% Liss Rhod-PE. The z-DS dispersion was mixed in a  
387 3:7 ratio with DMEM without FBS. As a control experiment, DMEM was mixed with pure  
388 Milli-Q in the same ratio. After 24 h of cultivation (37 °C, 5% CO<sub>2</sub>), medium was removed and  
389 replaced with 100 µL of either vesicle dispersion or control medium and incubated for  
390 additional 24 h. Finally, cells were observed before and after washing of the wells with PBS  
391 buffer using a fluorescence microscope Axio Observer Z1, equipped with an ApoTome system  
392 (Zeiss, Germany) using a 40x objective in phase contrast and fluorescence mode at excitation  
393  $\lambda = 544 \text{ nm}$ .

394  
395 *Insertion of  $\alpha$ -hemolysin.* 5 µl of  $\alpha$ -hemolysin in sodium citrate buffer (20 µM) were added to  
396 15 µl of z-DS dispersion prepared by thin-film hydration ( $c = 1 \text{ mg}\cdot\text{mL}^{-1}$ ) with encapsulated  
397 calcein and Co<sup>2+</sup> in the outer solution. The vesicle dispersion was visualized by CLSM after 1 h  
398 of the initial injection.

399

400 *Fusion of giant DSs with giant liposomes monitored in DLS.* Cationic DSs ( $\text{JD}^{\text{PC}}:\text{JD}^{\text{cat}}$  8:2 molar  
 401 ratio), uncharged z-DSs, anionic liposomes (DLPC:DLPG 8:2 molar ratio) and uncharged  
 402 DLPC liposomes were prepared by the extrusion method. Prior to mixing, the respective vesicle  
 403 dispersion were measured by DLS. The same volumes of each vesicle dispersion (500  $\mu\text{L}$  per  
 404 dispersion) were mixed to obtain a final volume of 1 mL per binary mixture. DLS of the  
 405 resulting mixed dispersions were measured after 1 h and 4 h of incubation.

406  
 407 *Fusion of giant DSs with giant liposomes monitored in CLSM.* In fusion experiments, vesicles  
 408 were prepared by following the thin-film hydration method. We assembled positively charged  
 409 dendrimersomes from 80 mol%  $\text{JD}^{\text{PC}}$  and 20 mol%  $\text{JD}^{\text{cat}}$  and labeled the membrane with  
 410 1 mol% Liss Rhod-PE. Negatively charged liposomes were assembled from 80 mol% DLPC  
 411 and 20 mol% DLPG and labeled with 1 mol% NBD-PC according to Table S4.  
 412 Dendrimersomes and liposomes were mixed in the same volumes and their fusion was studied  
 413 in CLSM immediately after mixing.

414  
 415 **Table S4.** Mixing protocol for co-assemblies used in CLSM fusion studies. Each sample was  
 416 rehydrated with 300  $\mu\text{L}$  of Milli-Q water.

	$\text{JD}^{\text{PC}}$	$\text{JD}^{\text{cat}}$	Rh-PE	DLPC	DLPG	NBD-PC
<b>n (mol%)</b>	79.2	19.8	1	79.2	19.8	1
<b><math>c_{\text{stock}}</math> (<math>\text{mg}\cdot\text{mL}^{-1}</math>)</b>	10	10	1	10	10	1
<b><math>V_{\text{stock}}</math> (<math>\mu\text{L}</math>)</b>	23.7	5.9	4.7	23.7	6.0	2.9

417  
 418 *Fluorescence Spectroscopy for the examination of fusion.* Vesicles were prepared by thin-film  
 419 hydration in Milli-Q water. Donor vesicles were labeled with 0.5 mol% of Liss Rhod-PE and  
 420 0.5 mol% of NBD-PE while acceptor vesicles were not labeled (Table S5). 6.25  $\mu\text{L}$  of donor  
 421 vesicle dispersion was mixed with 2.5 mL Milli-Q water and a stable baseline was recorded.  
 422 Afterwards, 12.5  $\mu\text{L}$  of acceptor vesicle dispersion was added. The excitation wavelength was  
 423 set to 467 nm, emission wavelength to 533 nm and the entrance slit and exit slit were 6 nm  
 424 band-pass.

425

426 **Table S5.** Mixing protocol for co-assemblies used in fusion experiments for fluorescence  
 427 spectroscopy. Each sample was rehydrated with 300  $\mu\text{L}$  of Milli-Q water.

	Donor Vesicles							Acceptor Vesicles		
	JD <sup>PC</sup>	JD <sup>cat</sup>	Rh- PE	NBD- PE	JD <sup>PC</sup>	Rh- PE	NBD- PE	DLPC	DLPG	DLPC
<b>n (mol%)</b>	79.2	19.8	0.5	0.5	99	0.5	0.5	80	20	100
<b>c<sub>stock</sub> (mg·mL<sup>-1</sup>)</b>	10	10	1	1	10	1	1	10	10	10
<b>V<sub>stock</sub> (<math>\mu\text{L}</math>)</b>	23.8	5.9	2.3	1.4	29.5	2.3	1.4	23.9	6.0	30

428  
 429 *H<sub>2</sub>O<sub>2</sub> biosensing.* z-DSs for sensing experiments were prepared via the general electroformation  
 430 protocol in a sucrose solution (100 mM) containing horseradish peroxidase (10 U·mL<sup>-1</sup>) and  
 431 DNA (74  $\mu\text{g}\cdot\text{mL}^{-1}$ ). 1 mol% Laurdan was used as a fluorescent membrane label. 0.2 mL of the  
 432 vesicle dispersion were mixed with 0.8 mL glucose solution (95 mM) and centrifuged at  
 433 2000 rpm for 3 minutes. 0.8 mL of the supernatant were exchanged for 0.8 mL 95 mM glucose  
 434 solution and centrifuged at 2000 rpm for 3 minutes. In total, this washing step was performed  
 435 7 times to remove outer HRP and DNA. The dihydroethidium solution was prepared by  
 436 injecting 1  $\mu\text{L}$  DHE solution in anhydrous DMSO (30 mM) into 1 mL of 95 mM glucose  
 437 solution and vortexing for 20 s. Prior to confocal measurements, 20  $\mu\text{L}$  of cleaned vesicle  
 438 dispersion was incubated with 80  $\mu\text{L}$  DHE solution for 15 minutes in the dark. To 20  $\mu\text{L}$  of the  
 439 incubated vesicle dispersion 0.5  $\mu\text{L}$  of H<sub>2</sub>O<sub>2</sub> solution (3 wt%) were added and the sample was  
 440 immediately observed via CLSM.

441  
 442 *Fluorescence Spectroscopy for the examination of biosensing.* For biosensing experiments,  
 443 vesicles were prepared by electroformation and purified as described in the previous section.  
 444 Here, the excitation wavelength was set to 515 nm, emission to 604 nm and the entrance slit  
 445 and exit slit were 6 nm band-pass.

446  
 447 *Particle tracking and Mean Square Displacement (MSD) calculation.* z-DSs for motility  
 448 experiments were prepared via the general electroformation protocol in a sucrose solution  
 449 (100 mM) containing catalase (10 U·mL<sup>-1</sup>). 1 mol% 16:0 Liss Rhod PE was used as a  
 450 fluorescent membrane label. 0.2 mL of the vesicle dispersion were mixed with 0.8 mL glucose  
 451 solution (95 mM) and centrifuged at 2000 rpm for 3 minutes. 0.8 mL of the supernatant were  
 452 exchanged for 0.8 mL 95 mM glucose solution and centrifuged at 2000 rpm for 3 minutes. In

453 total, this washing step was performed 7 times to remove outer catalase. A cut 0.5 mL  
454 Eppendorf tube was glued onto the glass slide using Norland Optical Adhesive 61 (Norland  
455 Products Inc, USA) and cured by UV irradiation for 15 min. Into the chamber, 20  $\mu\text{L}$  of cleaned  
456 vesicle dispersion were diluted with 180  $\mu\text{L}$  glucose solution. The vesicles were allowed to  
457 settle for 10 minutes. Afterwards, their motion was recorded. To start enzymatically driven  
458 motility, 2.5  $\mu\text{L}$  of  $\text{H}_2\text{O}_2$  solution (3 wt%) were added to the chamber. After 10 min, the z-DSs  
459 motion was recorded.

460 Vesicles were tracked in confocal fluorescence images using a modified algorithm based on the  
461 work of Crocker *et al.*<sup>[12]</sup> The intensity images were filtered in two steps. A smoothed image  
462 was created using a Gaussian filter with a standard deviation of 6 pixels, and a background  
463 image using a running average with a 15 pixels radius box-car kernel. Both kernels were  
464 normalized. The filtered image was the difference between the smoothed and the background  
465 images (see the band-pass filter in Crocker *et al.*). A threshold was applied at 15% of the  
466 maximal intensity of the filtered image, and every pixel below this value was ignored. Local  
467 maxima were found above the threshold with a radius of 6 pixels, then patches around these  
468 maxima were collected and the peak position was calculated from the first statistical momentum  
469 of the intensity around this pixel. For a more accurate estimation, the minimum of the intensity  
470 within the patch was subtracted. The obtained positions were collected to trajectories based on  
471 the nearest neighbors between images. A trajectory was cut if no neighbor was found within 10  
472 pixels around a position. Trajectories shorter than 100 points were ignored. Mean squared  
473 displacement was calculated as the population average of the squared distances from the first  
474 position of the trajectories  $r(0)$  according to:

$$MSD = \langle |r(t) - r(0)|^2 \rangle$$

477 *Micropipette aspiration.* Micropipettes were pulled from borosilicate capillaries (1B100-4,  
478 World Precision Instruments, Inc.) with pipette puller (Sutter Instruments, Novato, CA) and  
479 then shaped with a microforge (Narishige, Tokyo, Japan). The pipette tips were incubated in  
480 buffer solution, containing 2% casein to reduce the adhesion of the vesicle membrane to the  
481 pipette. After the incubation, the micropipette was rinsed with water to remove free BSA.  
482 Aspiration of GUVs was performed in a homemade experimental chamber with a volume of  
483 0.5 mL. GUVs were prepared according to the electroformation protocol in 100 mM sucrose  
484 solution using 0.5 mol% of DiIC<sub>18</sub> dye. Prior to measurement they were diluted with a 97 mM  
485 glucose solution (1:1 v:v). The chamber was built from two parallel glass coverslip separated  
486 by Teflon spacer with opening from one side for inserting the micropipette. After insertion of

487 the micropipette, the opening was sealed with silicone grease (Baysilone, Bayer) to prevent  
488 evaporation. The vesicles were observed on a Leica TCS SP5 confocal microscope (Mannheim,  
489 Germany), equipped with 40 x objective. DiIC<sub>18</sub> was excited with a diode-pumped solid-state  
490 laser 561 nm laser and the fluorescence signal was collected in the range of 580 – 700 nm. The  
491 micropipette was operated using a three-dimensional micromanipulator system (Sutter  
492 Instruments, Novato, CA) mounted on the microscope. The aspiration pressure in the  
493 micropipette was controlled by changing the height of a water reservoir mounted on a linear  
494 translational stage (M-531.PD, Physik Instrumente, Germany). The maximum difference in  
495 suction pressure between two data points was 200 N·m<sup>-2</sup>. The membrane was allowed to  
496 equilibrate for 30 s after each change in aspiration pressure. Equilibrium height of the water  
497 reservoir corresponding to zero pressure across the pipette tip was set prior to each measurement.  
498 The membrane tension was assessed as:

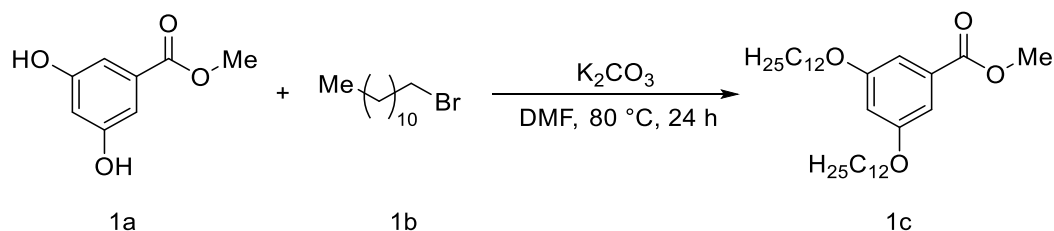
499 
$$\Sigma = \frac{\Delta P R_p}{2(1 - R_p/R_{ve})}$$

500 where  $\Delta P$  is the suction pressure,  $R_{ve}$  and  $R_p$  are respectively the radii of the spherical vesicle  
501 and the micropipette. The apparent area increase  $\alpha$  was determined according to a previously  
502 published protocol by measuring the length of the aspirated cylinder.<sup>[13]</sup>

503

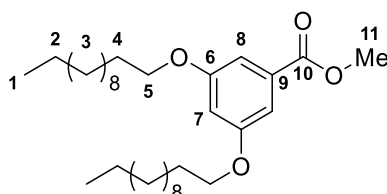
504 **3. Synthesis and molecular characterization**

505 Synthesis of methyl 3,5-bis(dodecyloxy)benzoate (1c)

506 **Figure S1.** Synthesis of 1c.  
507

508  
509 Following a modified procedure reported by Janni and Manheri,<sup>[14]</sup> under a nitrogen atmosphere  
510 a suspension of methyl 3,5-dihydroxybenzoate (1a, 6.00 g, 35.7 mmol, 1 equiv.) and K<sub>2</sub>CO<sub>3</sub>  
511 (29.6 g, 214 mmol, 6 equiv.) in DMF was stirred at room temperature for 5 min.  
512 1-Bromododecane (1b, 18.9 mL, 19.6 g, 78.5 mmol, 2.2 equiv.) was added over 1 min and the  
513 suspension was stirred at 80 °C for 24 h.

514 The reaction mixture was allowed to cool down to 60 °C and precipitated into water (300 mL).  
515 The suspension was filtered, and the filter cake dried *in vacuo*. The resulting solid was dissolved  
516 in CH<sub>2</sub>Cl<sub>2</sub> (200 mL), dried over MgSO<sub>4</sub> and passed through a basic alumina column using  
517 CH<sub>2</sub>Cl<sub>2</sub> as eluent. The solvent was evaporated *in vacuo* to yield the respective product as a  
518 white solid (17.8 g, 35.2 mmol, 99%).



519  
520 **Figure S2.** Chemical structure and NMR assignment of methyl 3,5-bis(dodecyloxy)benzoate  
521 (1c).  
522

523 **Molecular formula:** C<sub>32</sub>H<sub>56</sub>O<sub>4</sub>. **Molecular weight:** 504.80 g mol<sup>-1</sup>.

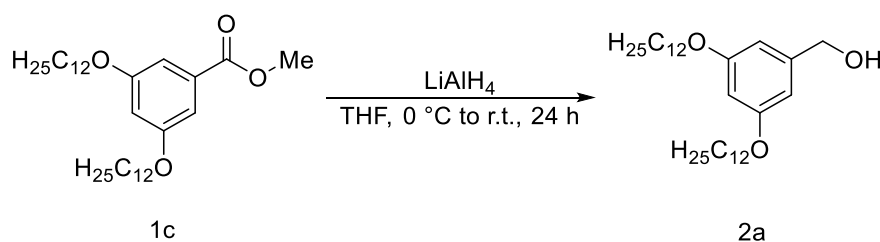
524 **<sup>1</sup>H-NMR** (400 MHz, CDCl<sub>3</sub>): δ = 7.15 (d, *J* = 2.3 Hz, 2H, **8-H**), 6.63 (t, *J* = 2.3 Hz, 1H, **7-H**),  
525 3.96 (t, *J* = 6.5 Hz, 4H, **5-H**), 3.89 (s, 3H, **11-H**), 1.77 (p, *J* = 6.7 Hz, 4H, **4-H**), 1.55-1.15 (m,  
526 36H, **2;3-H**), 0.88 (t, *J* = 6.7 Hz, 6H, **1-H**) ppm.

527 **<sup>13</sup>C-NMR** (75 MHz, CDCl<sub>3</sub>): δ = 167.1 (**10-C**), 160.3 (**6-C**), 131.9 (**9-C**), 107.8 (**8-C**), 107.7  
528 (**7-C**), 68.4 (**5-C**), 52.2 (**11-C**), 32.1 (**4-C**), 30.3-26.1 (**3-C**), 22.9 (**2-C**), 14.2 (**1-C**) ppm.

529 All spectroscopic data are in accordance with previous reports.<sup>[15]</sup>

530

531 Synthesis of (3,5-bis(dodecyloxy)phenyl)methanol (2a)



532

533 **Figure S3.** Synthesis of 2a.

534

535 Under a nitrogen atmosphere 1c (4.00 g, 7.93 mmol, 1 equiv.) was dissolved in THF (32 mL).

536 Immediately after placing the solution into an ice bath, a solution of LiAlH<sub>4</sub> in THF (1 M,

537 8 mL, 8 mmol, 1 equiv.) was slowly added under vigorous stirring. After complete addition the

538 ice bath was removed, and the solution was stirred at room temperature for 16 h.

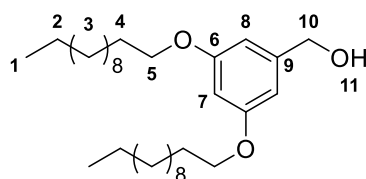
539 The reaction mixture was quenched by slow dropwise addition of saturated aqueous NaHCO<sub>3</sub>

540 solution under vigorous stirring. The resulting suspension was filtered, and the collected filtrate

541 was extracted with EtOAc (3 x 30 mL). The organic phases were combined and dried over

542 Na<sub>2</sub>SO<sub>4</sub>. The solvent was evaporated *in vacuo* to yield the desired product as a white solid

543 (3.59 g, 7.53 mmol, 95%).



544

545 **Figure S4.** Chemical structure and NMR assignment of (3,5-bis(dodecyloxy)phenyl)methanol  
546 (2a).

547

548 **Molecular formula:** C<sub>31</sub>H<sub>56</sub>O<sub>3</sub>. **Molecular weight:** 476.79 g mol<sup>-1</sup>.

549 **<sup>1</sup>H-NMR** (400 MHz, CDCl<sub>3</sub>): δ = 6.50 (d, *J* = 2.2 Hz, 2H, **8-H**), 6.38 (t, *J* = 2.3 Hz, 1H, **7-H**),

550 4.61 (s, 2H, **10-H**), 3.93 (t, *J* = 6.6 Hz, 4H, **5-H**), 2.04 (s, 1H, **11-H**), 1.76 (p, *J* = 6.7 Hz, 4H, **4-**

551 **H**), 1.47-1.27 (m, 36H, **2;3-H**), 0.88 ppm (t, *J* = 6.7 Hz, 6H, **1-H**).

552 **<sup>13</sup>C-NMR** (101 MHz, CDCl<sub>3</sub>): δ = 160.7 (**6-C**), 143.3 (**9-C**), 105.2 (**8-C**), 100.7 (**7-C**), 68.2 (**5-**

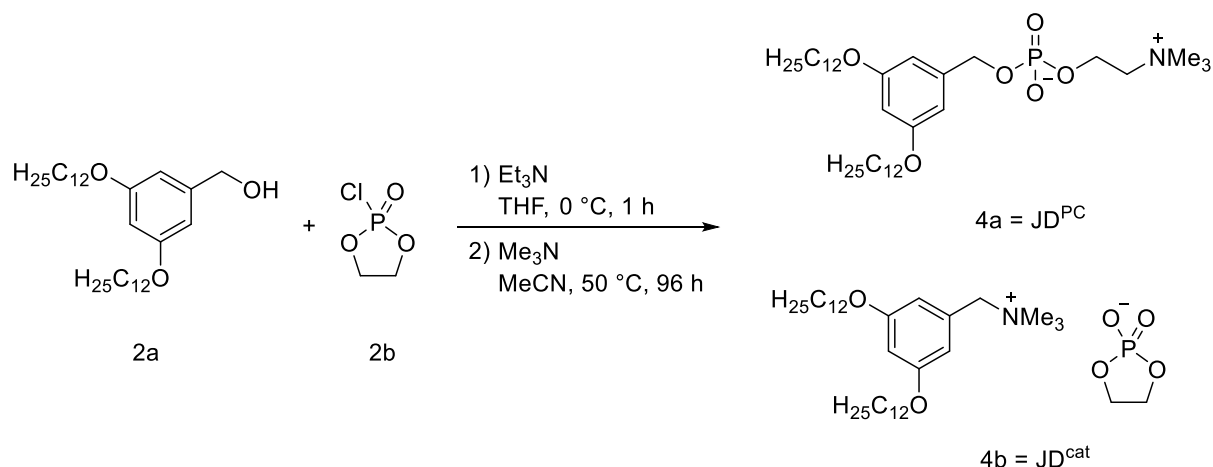
553 **C**), 65.6 (**10-C**), 32.1-26.2 (**3;4-C**), 22.8 (**2-C**), 14.3 (**1-C**) ppm.

554 All spectroscopic data are in accordance with previous reports.<sup>[16]</sup>

555

556

557 Synthesis of 3,5-bis(dodecyloxy)benzyl (2-(trimethylammonio)ethyl) phosphate (JD<sup>PC</sup>, 4a) and  
 558 1-(3,5-bis(dodecyloxy)phenyl)-*N,N,N*-trimethylmethanaminium 1,3,2-dioxaphospholan-2-  
 559 olate 2-oxide (JD<sup>cat</sup>, 4b)



560

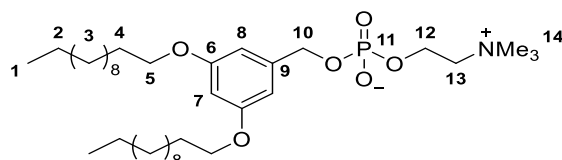
561 **Figure S5.** Synthesis of JD<sup>PC</sup> (4a) and JD<sup>cat</sup> (4b).

562

563 In a 10 mL Schlenk tube to a solution of 2a (1.00 g, 2.10 mmol, 1.05 equiv.) and anhydrous  
 564 Et<sub>3</sub>N (292 μL, 212 mg, 2.10 mmol, 1.05 equiv.) in THF (2.0 mL) was added 2b (183.8 μL,  
 565 286 mg, 2.00 mmol, 1 equiv.) at 0 °C and the reaction mixture was stirred at 0 °C for 1 hour.  
 566 The formed white precipitate was filtered off into a 50 mL round bottom flask under a nitrogen  
 567 atmosphere via a filter cannula. The precipitate was washed with anhydrous THF (3 x 0.5 mL)  
 568 and the combined filtrate was dried under stirring for 3 h *in vacuo*. A solution of Me<sub>3</sub>N in  
 569 anhydrous MeCN (2 M, 12 mL, 24 mmol, 12 equiv.) was added under a nitrogen atmosphere  
 570 and the flask was sealed using a new rubber septum. The reaction was stirred at 50 °C for 96 h.  
 571 The reaction mixture was concentrated *in vacuo*. The residue was subjected to flash column  
 572 chromatography (8 g SiO<sub>2</sub>, ~1 L 2:8 MeOH:CHCl<sub>3</sub> until the cationic product JD<sup>cat</sup> is removed  
 573 then 4:25:75 H<sub>2</sub>O:MeOH:CHCl<sub>3</sub>) to yield the desired product JD<sup>PC</sup> (06) as a colourless waxy  
 574 solid (146.0 mg, 0.227 mmol, 11%).

575 **Warning:** Under the reported reaction conditions, NMe<sub>3</sub> evaporates resulting in an overpressure  
 576 in the flask. Proper safety precautions should be taken by using a blast shield, as well as clean  
 577 and unblemished glassware that can withstand the generated pressure.

578



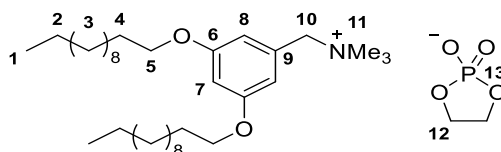
579

580 **Figure S6.** Chemical structure and NMR assignment of JD<sup>PC</sup>, 4a.

581

582 **Molecular formula:** C<sub>36</sub>H<sub>68</sub>NO<sub>6</sub>P. **Molecular weight:** 641.91 g mol<sup>-1</sup>.583 R<sub>f</sub> = 0.39 (4:25:75 H<sub>2</sub>O:MeOH:CHCl<sub>3</sub>)584 <sup>1</sup>H-NMR (400 MHz, CDCl<sub>3</sub>): δ = 6.48 (d, *J* = 2.2 Hz, 2H, **8-H**), 6.28 (t, *J* = 2.3 Hz, 1H, **7-H**),585 4.79 (d, *J* = 7.3 Hz, 2H, **10-H**), 4.22-4.08 (m, 2H, **12-H**), 3.85 (t, *J* = 6.6 Hz, 4H, **5-H**), 3.71-586 3.63 (m, 2H, **13-H**), 3.23 (s, 9H, **14-H**), 1.69 (p, *J* = 6.8 Hz, 4H, **4-H**), 1.45-1.16 (m, 36H,587 **2;3-H**), 0.84 (t, *J* = 6.8 Hz, 6H, **1-H**) ppm.588 <sup>13</sup>C-NMR (101 MHz, CDCl<sub>3</sub>): δ = 160.4 (**6-C**), 141.5 (d, *J* = 7.0 Hz, **9-C**), 106.0 (**8-C**), 100.1589 (**7-C**), 68.2 (**5-C**), 67.3 (d, *J* = 5.4 Hz, **10-C**), 66.3 (d, *J* = 6.8 Hz, **11-C**), 59.2 (d, *J* = 4.9 Hz, **12-**590 **C**), 54.3 (**13-C**), 32.0-26.2 (**3;4-C**), 22.8 (**2-C**), 14.2 (**1-C**) ppm.591 <sup>31</sup>P-NMR (162 MHz, CDCl<sub>3</sub>): δ = -0.38 (**11-P**) ppm.592 **HR-ESI-MS:** *m/z*: calcd. for [M+H]<sup>+</sup> = [C<sub>36</sub>H<sub>69</sub>NO<sub>6</sub>P]<sup>+</sup>: 664.4857; found: 642.4888.

593



594

595 **Figure S7.** Chemical structure and NMR assignment of JD<sup>cat</sup>, 4b.

596

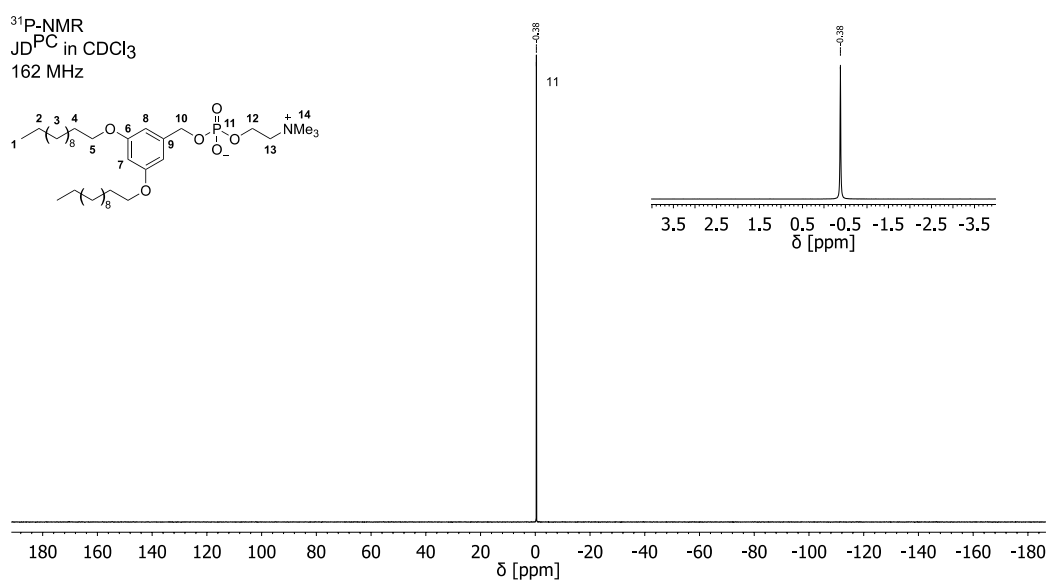
597 JD<sup>cat</sup> was isolated as a yellow tinted solid (320 mg, 0.499 mmol, 50%) from a downscaled

598 reaction where the above procedure was performed in a 25 mL flask using half of the amount

599 of reported reagents.

600 **Molecular formula:** C<sub>36</sub>H<sub>68</sub>NO<sub>6</sub>P. **Molecular weight:** 641.91 g mol<sup>-1</sup>.601 R<sub>f</sub> = 0.33 and 0.78 (2:8 MeOH:CHCl<sub>3</sub>)602 <sup>1</sup>H-NMR (400 MHz, CDCl<sub>3</sub>): δ = 6.66 (d, *J* = 2.0 Hz, 2H, **8-H**), 6.54-6.47 (m, 1H, **7-H**), 4.69603 (s, 2H, **10-H**), 4.20 (d, *J* = 10.1 Hz, 4H, **12-H**), 3.93 (t, *J* = 6.5 Hz, 4H, **5-H**), 3.23 (s, 9H, **11-H**),604 1.74 (p, *J* = 6.6 Hz, 4H, **4-H**), 1.50-1.14 (m, 36H, **2;3-H**), 0.87 (t, *J* = 6.8 Hz, 6H, **1-H**) ppm.605 <sup>13</sup>C-NMR (101 MHz, CDCl<sub>3</sub>): δ = 160.8 (**6-C**), 129.5 (**9-C**), 111.4 (**8-C**), 103.2 (**7-C**), 69.8,606 (**12-C**), 68.5 (**5-C**), 64.6 (**10-C**), 53.0 (**11-C**), 32.1-26.2 (**3;4-C**), 22.8 (**2-C**), 14.3 (**1-C**) ppm.607 <sup>31</sup>P-NMR (162 MHz, CDCl<sub>3</sub>): δ = -17.14 (**13-P**) ppm.608 **HR-ESI-MS:** *m/z*: calcd. for [M-C<sub>2</sub>H<sub>4</sub>O<sub>4</sub>P]<sup>+</sup> = [C<sub>34</sub>H<sub>64</sub>NO<sub>2</sub>]<sup>+</sup>: 518.4932; found: 518.4953.



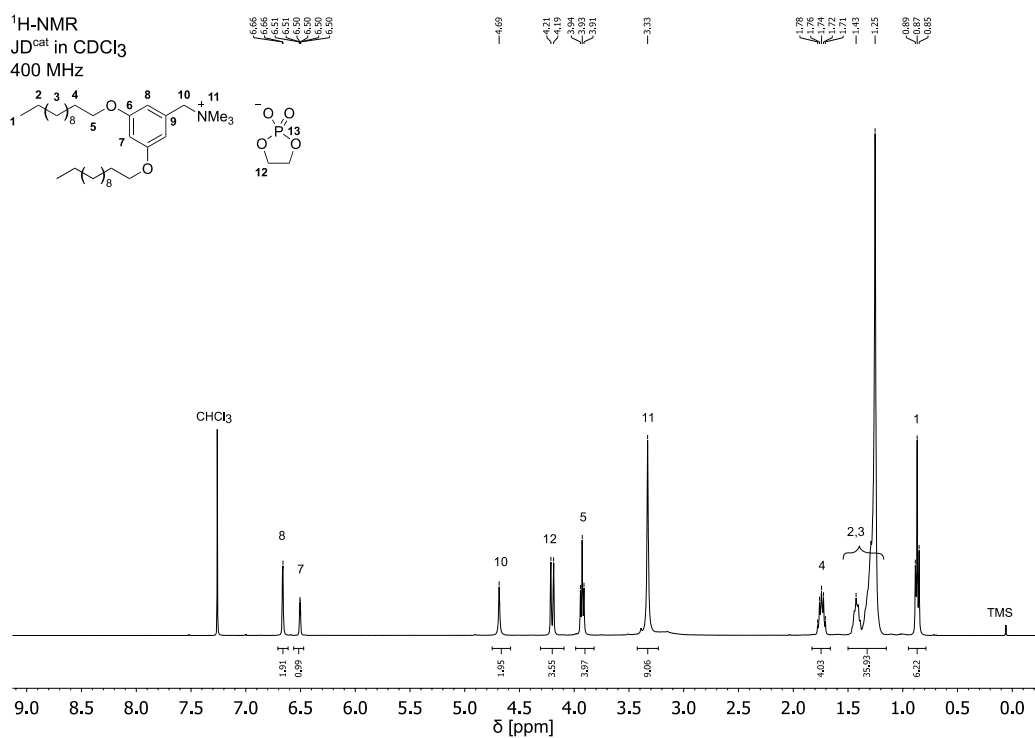


615

616 **Figure S10.** <sup>31</sup>P-NMR of JD<sup>PC</sup>.

617

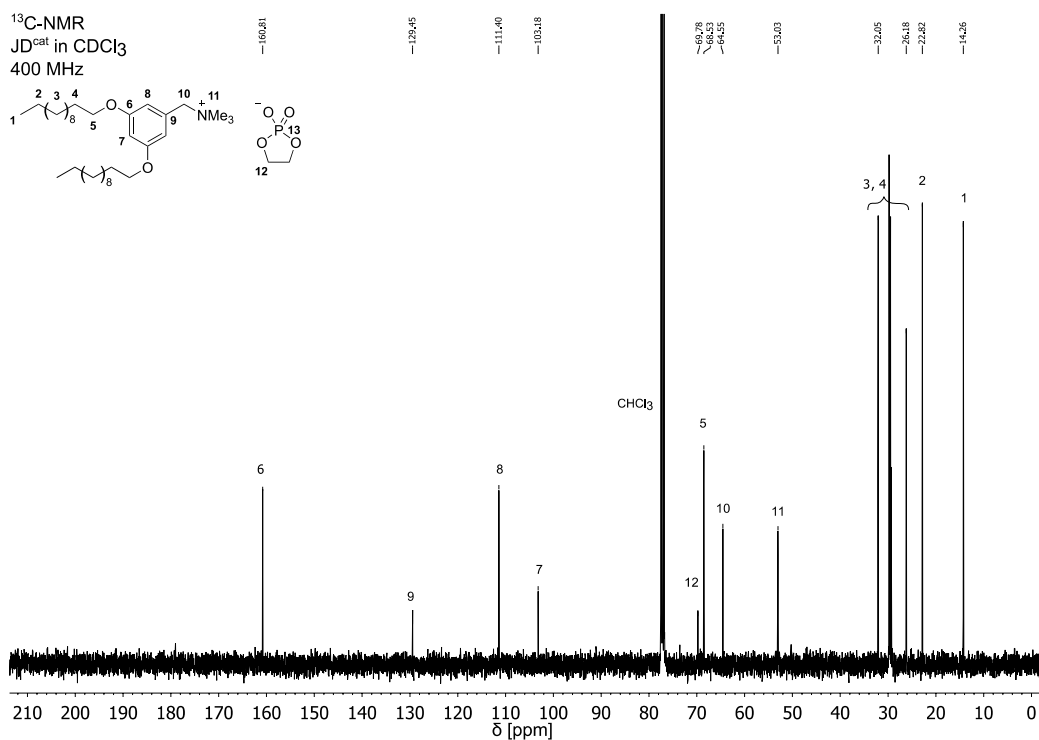
618

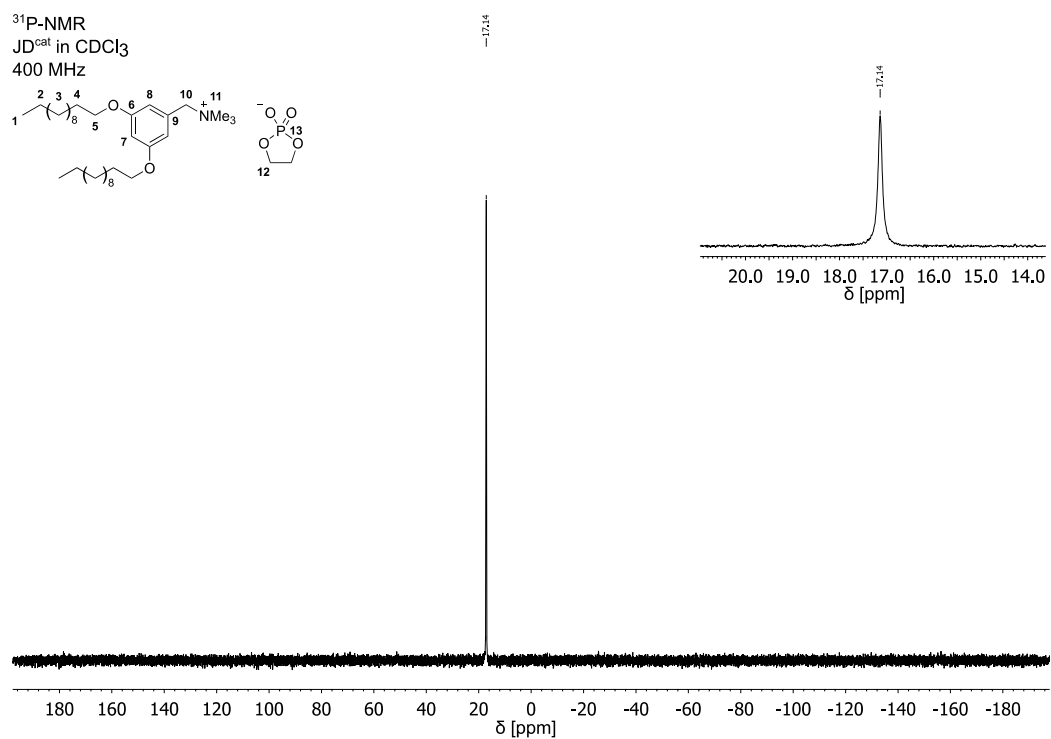
4.2 NMR characterization of JD<sup>cat</sup>

619

620 **Figure S11.** <sup>1</sup>H-NMR of JD<sup>cat</sup>.

621

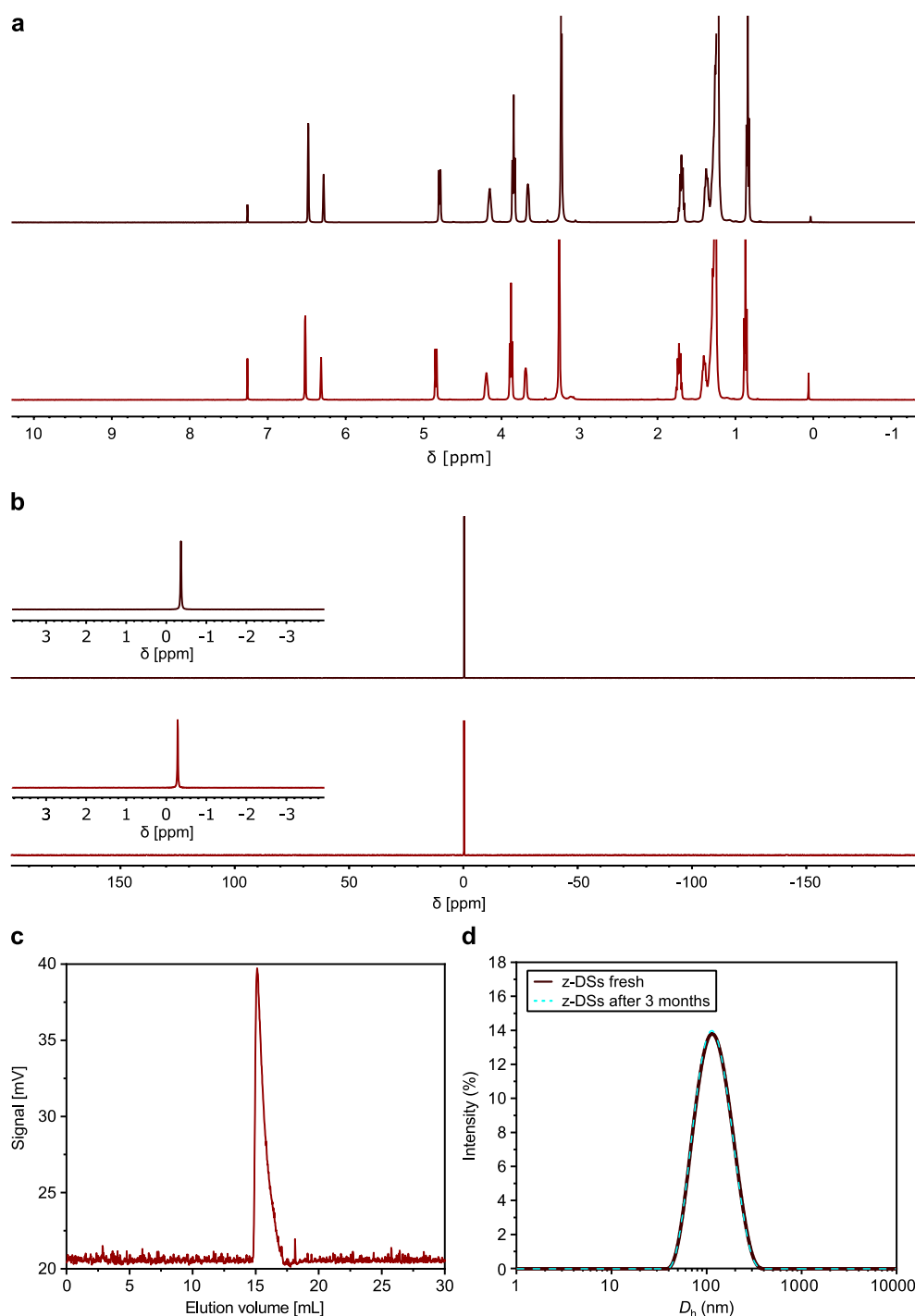




624

625 **Figure S13.**  $^{31}\text{P}$ -NMR of JD<sup>cat</sup>.

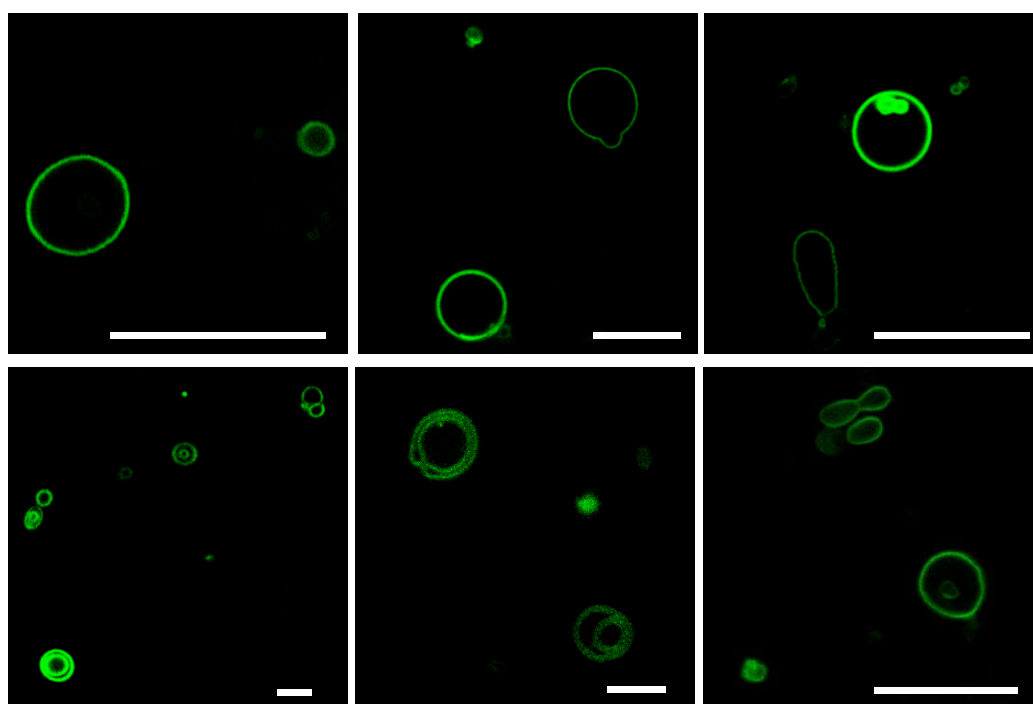
626

4.3 Long-term stability studies of bulk JD<sup>PC</sup> and z-DSs

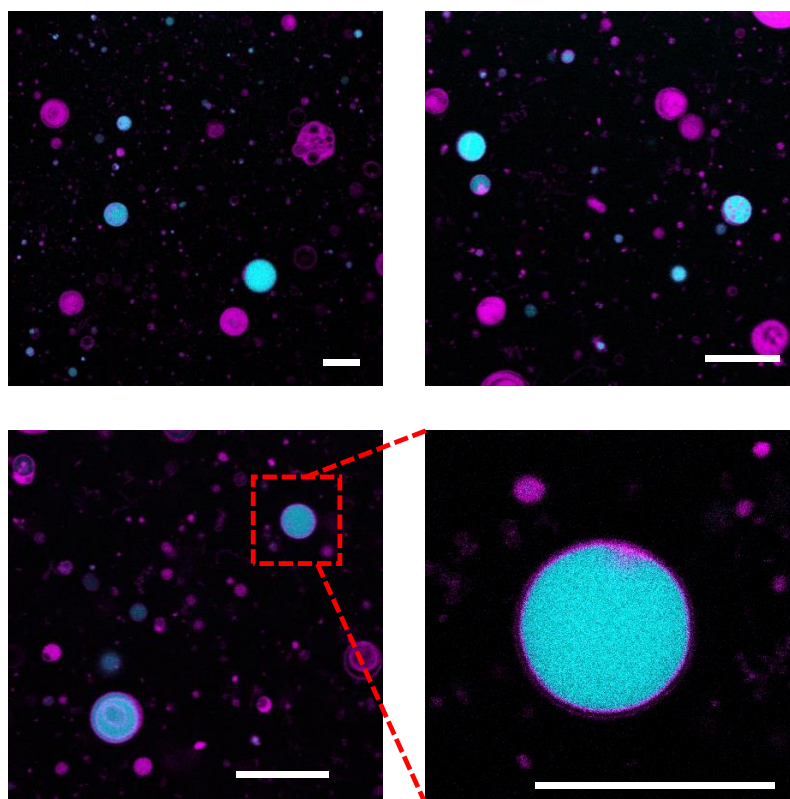
628

629 **Figure S14.** Long-term stability of JD<sup>PC</sup> and resulting z-DSs. (a) <sup>1</sup>H-NMR and (b) <sup>31</sup>P-NMR of  
 630 bulk JD<sup>PC</sup> directly after synthesis (top, black) and after 9 months of storage under ambient  
 631 conditions (bottom, red) show no significant changes. (c) Analytical HPLC of the bulk JD<sup>PC</sup>  
 632 sample after 9 months storage shows a single peak. Detector: Evaporative light scattering. (d)  
 633 Intensity distribution function of the  $D_h$  of small z-DSs prepared with injection method shows  
 634 no changes in distribution after 3 months storage under ambient conditions. The measurement  
 635 was carried out by DLS.

636 The long-term stability of giant z-DSs was investigated by forming vesicles by thin-film  
637 hydration in 10 mM HEPES buffer and storing the sample for 18 months at ambient conditions.  
638 Figure S15 depicts multiple CLSM overview images of giant z-DSs confirming that z-DSs are  
639 stable over long time periods, even in presence of salts. Additionally, we studied whether  
640 encapsulated components within the z-DS lumen or within the DS membrane undergo leakage  
641 over time (Figure S16). z-DSs were formed in a hydrophilic calcein solution  
642 ( $c = 0.03 \text{ mg}\cdot\text{mL}^{-1}$ ), and lipophilic Nile red was encapsulated within the membrane. The outside  
643 fluorescence of calcein was quenched upon addition of a  $\text{CoCl}_2$  solution. Calcein-filled and  
644 membrane-labeled z-DSs were stored at ambient conditions for 12 months. CLSM studies  
645 revealed that the vesicles remained intact, and both hydrophilic and lipophilic dyes did not leak.



646  
647 **Figure S15.** Long-term stability of giant z-DSs in buffer solution. z-DSs were formed in 10 mM  
648 HEPES buffer and stored for 18 months at ambient conditions. The membrane was labeled with  
649 0.5 mol% Bodipy. Scale bar is 20  $\mu\text{m}$ .

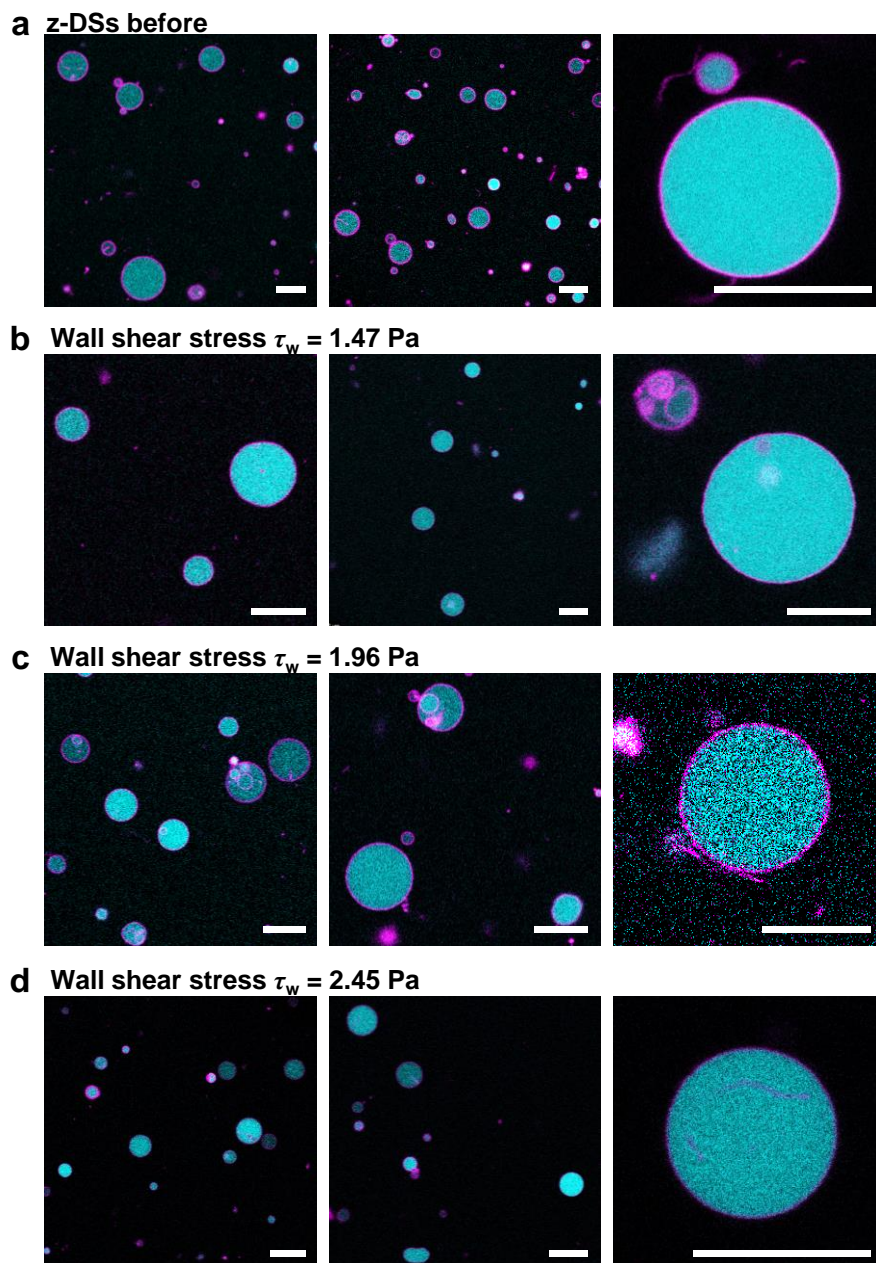


650  
 651 **Figure S16.** Long-term leakage study of giant z-DSs with encapsulated fluorescent hydrophilic  
 652 dye in the lumen and fluorescent lipophilic dye within the membrane. Vesicles were formed in  
 653 calcein (cyan), and the membrane was labeled with 0.5 mol% Nile red (magenta). Calcein was  
 654 quenched in the outer vesicle solution by adding  $\text{Co}^{2+}$ . After storing the vesicles for 12 months  
 655 at ambient conditions, we observed no leakage of calcein or Nile red. Scale bar is 20  $\mu\text{m}$ .

656

#### 657 **4.4 Stability of z-DSs under shear stress**

658 z-DSs were assembled by electroformation in a solution of 200 mM sucrose and calcein  
 659 ( $c = 0.03 \text{ mg}\cdot\text{mL}^{-1}$ ) while the membrane was labeled with 0.5 mol% Nile red. Prior to  
 660 observation in CLSM, z-DSs were mixed with 200 mM glucose (1:1). The fluorescence of  
 661 calcein in the outer solution was quenched upon addition of  $\text{Co}^{2+}$ . The calcein-filled z-DSs were  
 662 subjected to three different shear stress ranging from i)  $\tau_w = 1.47 \text{ Pa}$  ii)  $\tau_w = 1.96 \text{ Pa}$  to iii)  
 663  $\tau_w = 2.45 \text{ Pa}$  by varying the flow between 300 – 500  $\mu\text{L}\cdot\text{min}^{-1}$  (Figure S17). Such shear stress  
 664 is comparable to physiological conditions where shear stresses typically ranges from  $\tau = 0.003$ -  
 665 0.007 Pa in the eye up to  $\tau = 0.009 - 3 \text{ Pa}$  in the peroneal veins.<sup>[10, 17]</sup> At all applied shear stress  
 666 values, the z-DS membrane remained intact and no leakage of calcein was observed.

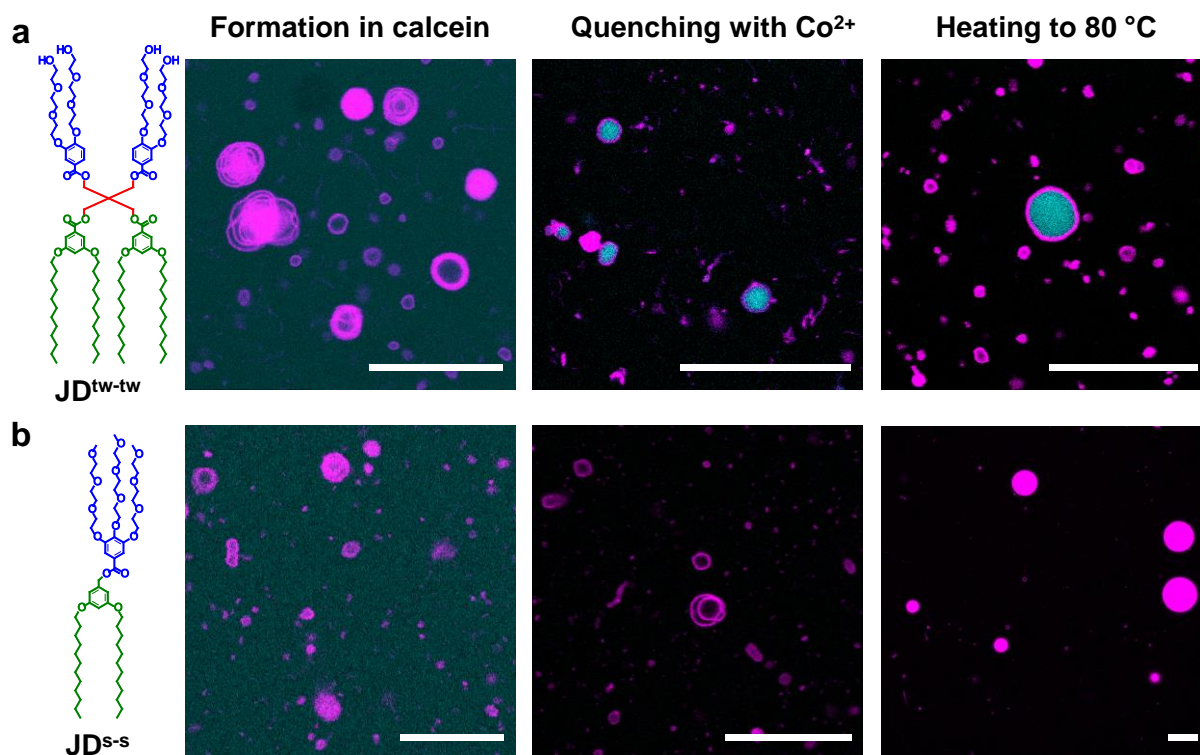


667  
 668 **Figure S17.** Effect of shear stress on the stability of calcein-filled z-DSs. Vesicles were  
 669 electroformed in 200 mM sucrose and calcein ( $c = 0.03 \text{ mg}\cdot\text{mL}^{-1}$ , cyan), and the membrane  
 670 was labeled with 0.5 mol% Nile red (magenta). Calcein was quenched in the outer vesicle  
 671 solution by adding  $\text{Co}^{2+}$  ions. Vesicles were imaged in CLSM after mixing with 200 mM  
 672 glucose (1:1) a) before shear stress and b) after applying a wall shear stress of  $\tau_w = 1.47$  Pa at  
 673  $300 \mu\text{L}\cdot\text{min}^{-1}$  flow speed, c)  $\tau_w = 1.96$  Pa at  $400 \mu\text{L}\cdot\text{min}^{-1}$  flow speed and d)  $\tau_w = 2.45$  Pa at  
 674  $500 \mu\text{L}\cdot\text{min}^{-1}$  flow speed. Scale bar is  $20 \mu\text{m}$ .  
 675

**676 4.5 Thermal stability of single-single and twin-twin dendrimersomes**

677 Thermal stability was additionally performed for dendrimersomes assembled from a single-  
678 single and a twin-twin JD in order to compare it with z-DSs. We used a single-single JD ( $JD^{s-s}$ )  
679 bearing the same hydrophobic dendron as  $JD^{PC}$  and a 3,4,5-substituted triethyleneglycol arene  
680 as the hydrophilic dendron (1). The twin-twin JD ( $JD^{tw-tw}$ ) consisted of the same hydrophobic  
681 dendron as  $JD^{PC}$  and a 3,4- substituted triethyleneglycol arene as the hydrophilic dendron. The  
682 experiments were performed as described above. Briefly, dendrimersomes were assembled by  
683 thin-film hydration in a solution of calcein. Both dendrimers formed dendrimersomes (Figure  
684 S18) with calcein encapsulated, although the overall quality of  $JD^{s-s}$  was lower than for  $JD^{tw-tw}$ .  
685 Then,  $Co^{2+}$  was added to quench the calcein remaining in the outside the dendrimersomes. The  
686 addition of these ions had no effect on the encapsulated calcein in  $JD^{tw-tw}$  dendrimersomes but  
687 quenched it in the  $JD^{s-s}$ . Thermal treatment at 80°C for 1 h destabilized the  $JD^{s-s}$   
688 dendrimersomes, which now formed aggregates and drops. On the other hand, the lumen of  
689  $JD^{tw-tw}$  dendrimersomes remained green fluorescent, indicating that they were stable. The  
690 comparable higher stability arises from the increased hydrophobic effect stemming from two  
691 hydrophobic dendrons.

692



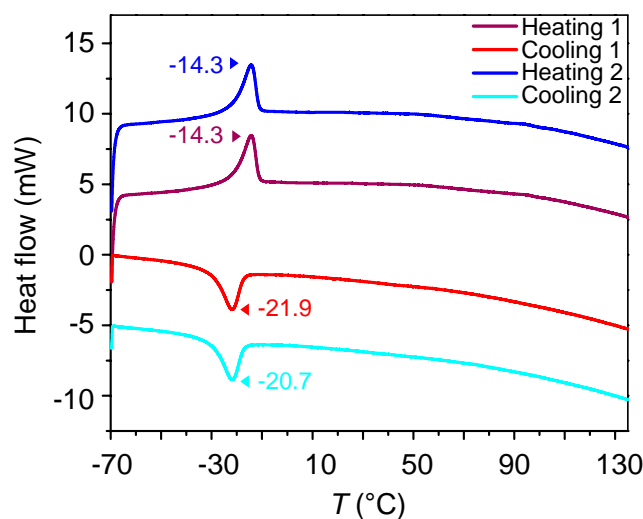
693

694

695 **Figure S18.** Temperature stability of calcein-filled a) single-single JDs (JD<sup>s-s</sup>) and b) twin-twin  
696 JDs (JD<sup>tw-tw</sup>). Vesicles were formed in calcein (cyan), and the membrane was labeled with  
697 0.5 mol% Nile red (magenta). Calcein was quenched in the outer vesicle solution by adding  
698 Co<sup>2+</sup> ions. Afterwards, vesicles were heated to 80°C for 1 h and then imaged in CLSM. Scale  
699 bar is 20 μm.

700

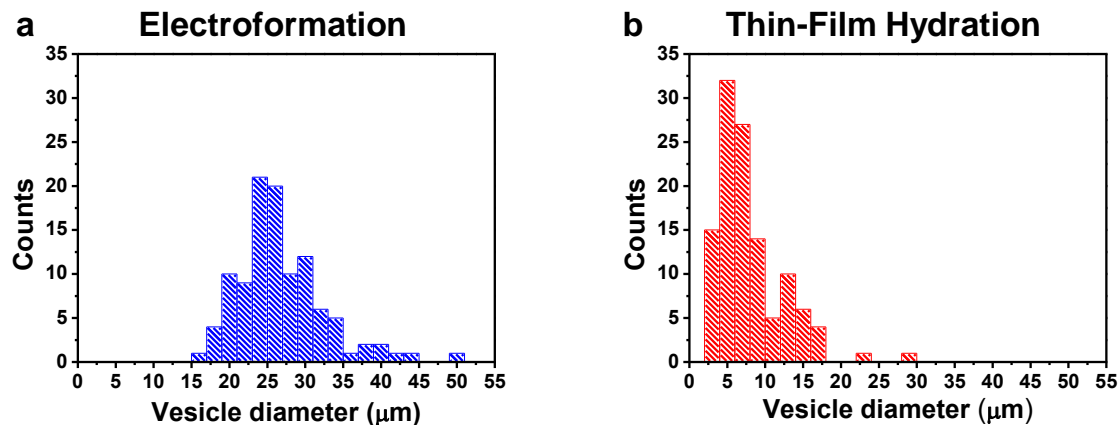
## 701 4.6 Differential Scanning Calorimetry



702  
 703 **Figure S19.** Thermal analysis of an annealed JD<sup>PC</sup> sample by DSC show distinct melting  
 704 transition at  $-14.3$  °C and an associated crystallization peak at  $-21.9$  °C. A subsequent heating  
 705 and cooling cycle displayed similar transitions. Therefore, at room temperature, JD<sup>PC</sup> is above  
 706 its phase transition temperature.

707

## 708 4.7 Analysis of distribution of size

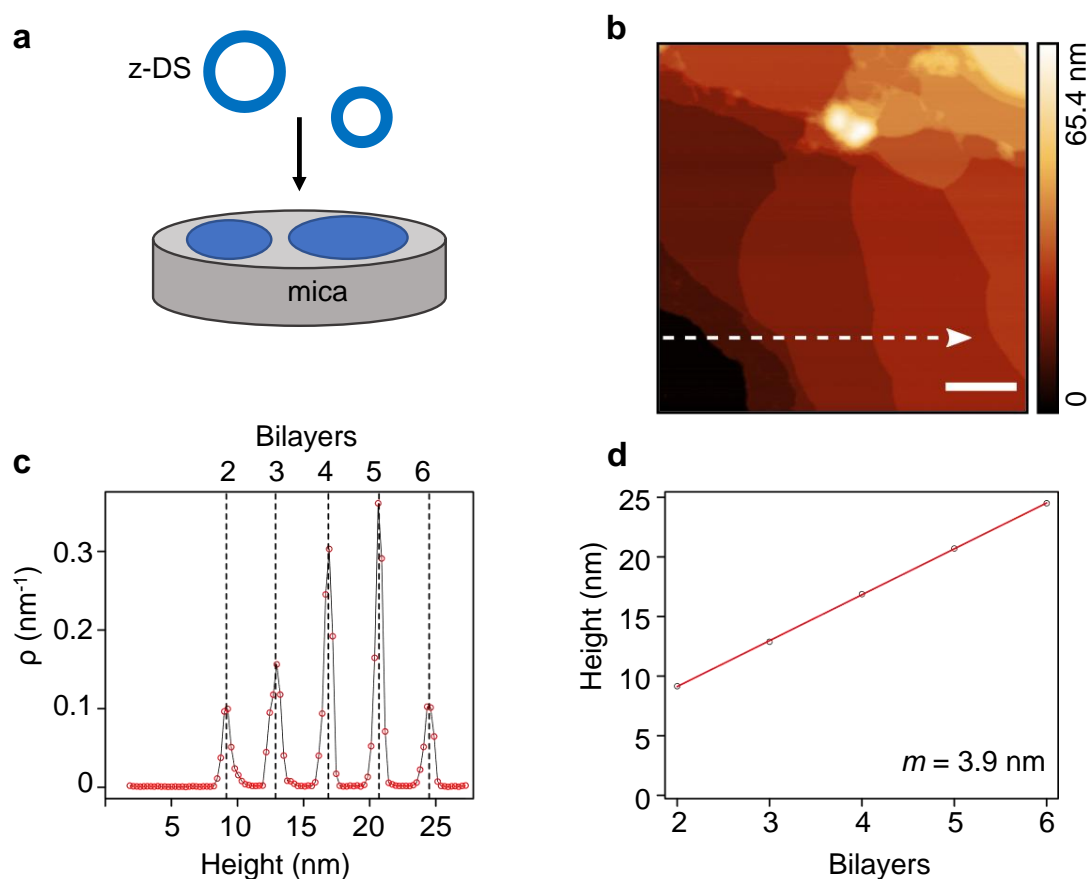


709  
 710 **Figure S20.** Analysis of z-DS sizes comparing vesicles prepared by a) electroformation and b)  
 711 thin-film hydration. 100 vesicles were analyzed for each method using CLSM images.

712

713 **4.8 Analysis of bilayer thickness by AFM**

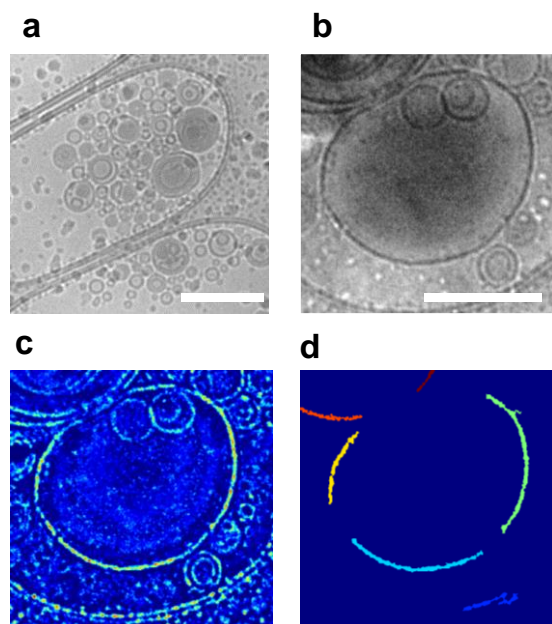
714 z-DSs were self-assembled by thin-film hydration and then drop casted on a freshly cleaved  
 715 mica surface. During drying of the JD film at ambient conditions, the vesicles collapse and form  
 716 a stack of flattened bilayers which allows to precisely measure the bilayer thickness. The  
 717 topology image in Figure S21b reveals at least six overlying flattened bilayers. The probability  
 718 density of bilayer heights in Figure S21b was analyzed with a custom-written script in R to find  
 719 the locations of the peaks. Therefore, a smoothed derivative was calculated by applying the first  
 720 derivative of a normalized Gaussian function. The transition points from positive to negative  
 721 values were found and refined by applying a first statistical momentum. The resulting peak  
 722 positions were plotted against their index and fitted with a linear regression to determine the  
 723 slope as the average bilayer height. Figure S21 reveals an average bilayer thickness of 3.9 nm.



724  
 725 **Figure S21.** Bilayer thickness analysis by AFM. (a) A dispersion of JD<sup>PC</sup> DSs was drop casted  
 726 on mica and dried to form a flattened stack of bilayer. (b) Topology scan in AFM depicts at  
 727 least 6 overlying bilayers. Scale bar is 500 nm. (c) Probability density of bilayer heights from  
 728 (b). (d) Analysis of the height distribution yields an average DS bilayer thickness of 3.9 nm.  
 729

730 **4.9 Analysis of bilayer thickness by cryo-TEM**

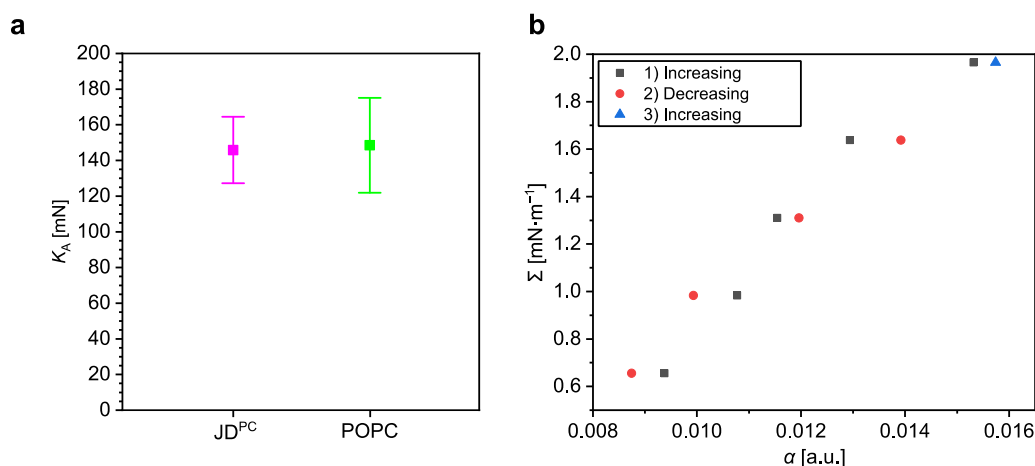
731 The analysis of the bilayer thickness of JD<sup>PC</sup> DSs was performed with z-DSs prepared by the  
732 injection method. Image processing of cryo-TEM images was performed using a custom-made  
733 python script following a general procedure. Background images were generated by smoothing  
734 via convolution of a Gaussian weight function (window typically 61 pixels, width  $\sigma = 10$   
735 pixels). The background was subtracted from the original image. All negative pixel values were  
736 set to zero. The resulting image was smoothed with a second Gaussian kernel (window size = 11  
737 pixels and width  $\sigma = 1$  pixels). A binary object mask was formed from pixels above an estimated  
738 threshold according to the 0.9 – 0.95 quantile of the corrected image. Pixels outside of the  
739 object areas defined by the mask image were set to zero, and pixels within the object mask were  
740 used to generate histograms typically with 250 bins between  $-1$  and  $1$ . The analysis reveals a  
741 constant bilayer thickness of 3.9 nm.



742 **Figure S22.** Bilayer thickness analysis by cryo-TEM. (a) Overview image displaying a  
743 multitude of small unilamellar JD<sup>PC</sup> vesicles. (b) A single unilamellar vesicle was chosen for  
744 the image analysis following (c, d) image processing yielding a bilayer thickness of 3.9 nm.  
745 Scale bars are 200 nm.  
746  
747

748

## 4.10 Micropipette aspiration studies



749

750 **Figure S23.** (a) Areal expansion modulus ( $K_A$ ) determined by micropipette aspiration show  
 751 similar elasticity of  $JD^{PC}$  and POPC membranes. Each point depicts the average value of 13 z-  
 752 DSs and 6 liposomes with the standard deviation, respectively. (b) Hysteresis analysis of an  
 753 aspirated z-DS in the high-tension regime shows a linear response between the tension  $\Sigma$  and  
 754 the apparent area increase  $\alpha$  during the first aspiration (1, black squares). Decreasing the  
 755 aspiration pressure led to a similar linear relationship (2, red dots), showing no hysteresis. A  
 756 final aspiration to the highest tension (3, blue triangle) demonstrated the reproducible response  
 757 of the z-DSs.

758

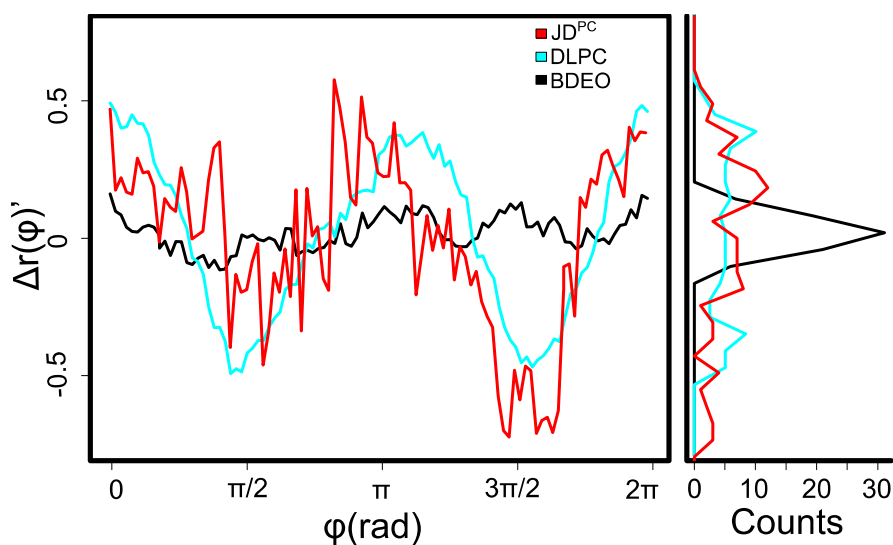
## 4.11 Analysis of membrane fluctuations

760 The bending rigidity and thus flexibility is governed by the membranes' ability to fluctuate.  
 761 Therefore, we studied the membrane undulations of vesicles from  $JD^{PC}$  as well as from a lipid  
 762 (DLPC) and from a block-copolymer (poly(BD87-b-EO72) (BDEO), respectively by CLSM.  
 763 The fluctuation analysis was performed by a custom-made script in python.<sup>[18]</sup> First, the  
 764 membrane of the vesicle was identified, and surrounding objects were removed using Fiji  
 765 ImageJ.<sup>[19]</sup> The background was subtracted from the original image and negative pixels set to  
 766 zero by a convolution of a Gaussian kernel (window size of 61 pixels, width  $\sigma = 10$  pixels).  
 767 Smoothing of the resulting image was performed by applying a second Gaussian kernel  
 768 (window size of 21 pixels, width  $\sigma = 3$  pixels). Following Otsu's method,<sup>[20]</sup> we generated a  
 769 binary image by applying a threshold. Confluent images with a predefined size range were  
 770 selected from the binary images, ranging from 500 – 15000 pixels area for each image. The  
 771 center of the vesicle was identified and expressed as polar coordinates and angles ( $0 - 2\pi$  rad)  
 772 relative to the center of the object. To determine the radius of the vesicle, the maximum was  
 773 identified in the defined angle bins and a local straight line was fitted in both directions from

774 the maximum and the crossing point.<sup>[5b]</sup> The exported profiles were further processed using R  
 775 by subtracting the mean radius from each data set according to  $\Delta r = r - \langle r \rangle$ . The zero angle was  
 776 set to the maximum of the curve and  $\Delta r(\varphi)$  was fitted with a series of cosine functions with  
 777 integer harmonics where  $\varphi$  is the angle obtained from the data set:

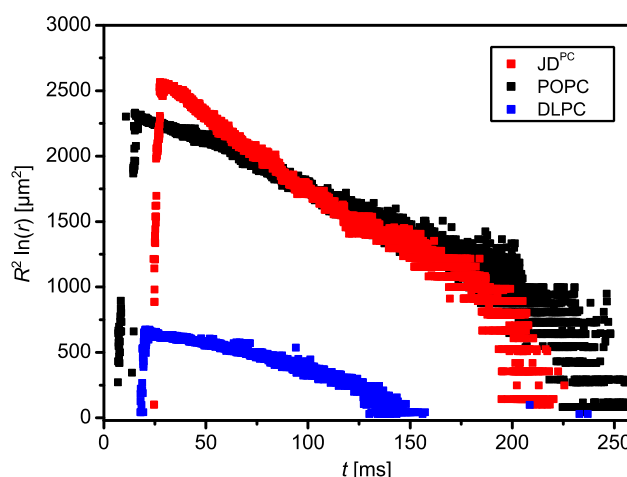
$$778 \quad \Delta r = \sum_{i=1}^N \alpha_i \cdot \cos(i\varphi)$$

779 The shape contributions were removed to show the individual fluctuation independent of size  
 780 and shape<sup>[21]</sup> by subtracting the two first harmonics of the cosine series generating  $\Delta r(\varphi)'$  from  
 781  $\Delta r(\varphi)$ .



782  
 783 **Figure S24.** Angular fluctuation of radii ( $\Delta r(\varphi)'$ ) of JD<sup>PC</sup> dendrimersomes, DLPC liposomes  
 784 and BDEO polymersomes after subtracting the first two harmonics of the cosine decomposition  
 785 (left) and distribution of the fluctuations (right).

786

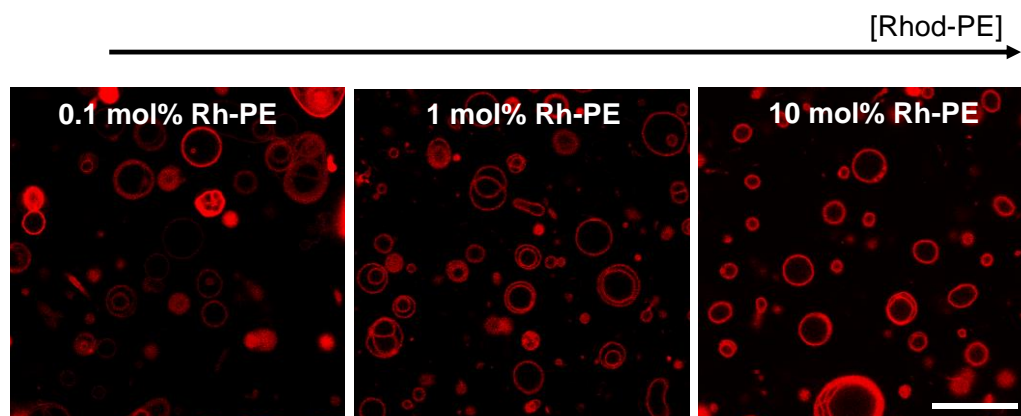
787 **4.12 Electroporation**

788  
789 **Figure S25.** Representative traces for the evolution of the porated region as a function of time  
790 in electroporation experiments for JD<sup>PC</sup> (red), POPC (black) and DLPC (blue).  $R$  is the vesicle  
791 radius,  $r$  the pore radius and  $t$  the time.

792

793 **4.13 Lipid-JD<sup>PC</sup> hybrids**

794 Co-assemblies of JD<sup>PC</sup> with different molar ratios of fluorescently labeled 16:0 Liss Rhod PE  
795 (0.1 – 10 mol%) lipid were prepared by thin-film hydration and visualized by CLSM. In all  
796 cases we observed GUVs with no apparent phase separation.



797  
798 **Figure S26.** CLSM images of JD<sup>PC</sup> co-assembled with fluorescently labeled Liss Rhod-PE with  
799 molar ratios in the range of 0.1 – 10 mol%. Scale bars are 20  $\mu\text{m}$ .

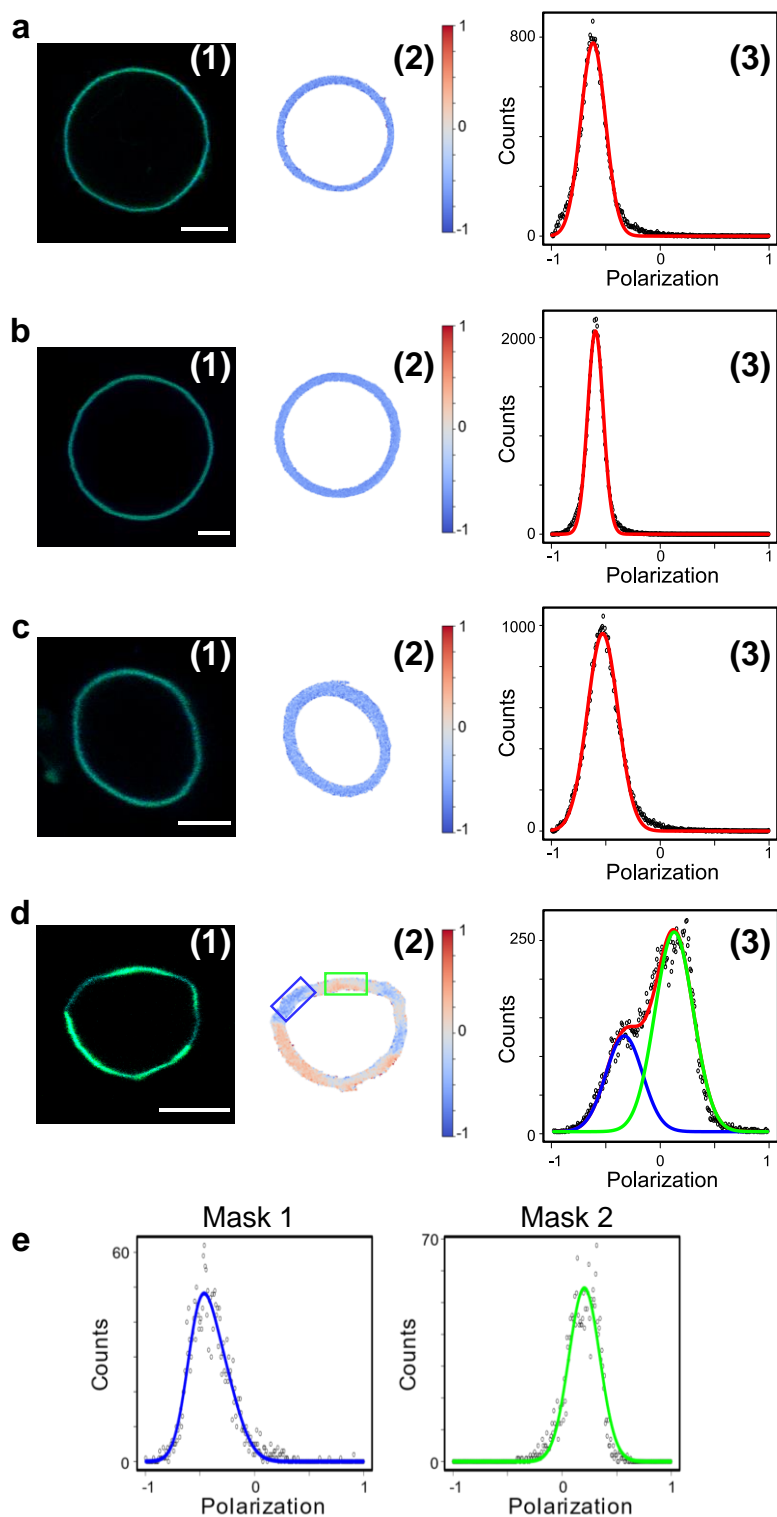
800

801 **4.14 Formation of raft-like microdomains**

802 We performed Laurdan generalized polarization (GP) analysis of JD<sup>PC</sup> vesicles labeled with  
803 1 mol% Laurdan and co-assembled by thin-film hydration with 20 mol% of DLPC (12:0 PC),  
804 DPPC (16:0 PC) or DSPC (18:0 PC), respectively. JD<sup>PC</sup> DSs were also prepared without  
805 additional lipids as a control sample. The vesicles were observed in CLSM using an attenuated  
806 (5%) 405 nm laser. Two emission ranges of  $\lambda_1 = 415 - 455$  nm and  $\lambda_2 = 490 - 530$  nm were  
807 simultaneously detected. Image processing was performed using a custom-made python script  
808 based on numpy, matplotlib and ImageP packages. The obtained images were smoothed using  
809 the Gaussian weight function. A sum image from the two emission ranges was generated. The  
810 background was subtracted by convolving a normalized Gaussian kernel (width = 20 pixels,  
811 window size = 121 pixels). All negative pixel values were set to zero. The resulting image was  
812 smoothed with a local weighted average using a Gaussian function with a width of 2 pixels  
813 (window size = 7 pixels). A binary object mask was formed from pixels above an estimated  
814 threshold according to the 0.9 – 0.95 quantile of the corrected image. Pixels outside of the  
815 object areas defined by the mask image were set to zero, and pixels within the object mask were  
816 used to generate histograms typically with 250 bins between –1 and 1. The GP was calculated  
817 according to Equation 3 where  $I_1$  and  $I_2$  denote the intensities detected in the 415 – 445 nm  
818 range the 490 – 530 nm range, respectively.

$$GP = \frac{I_1 - I_2}{I_1 + I_2} \quad (3)$$

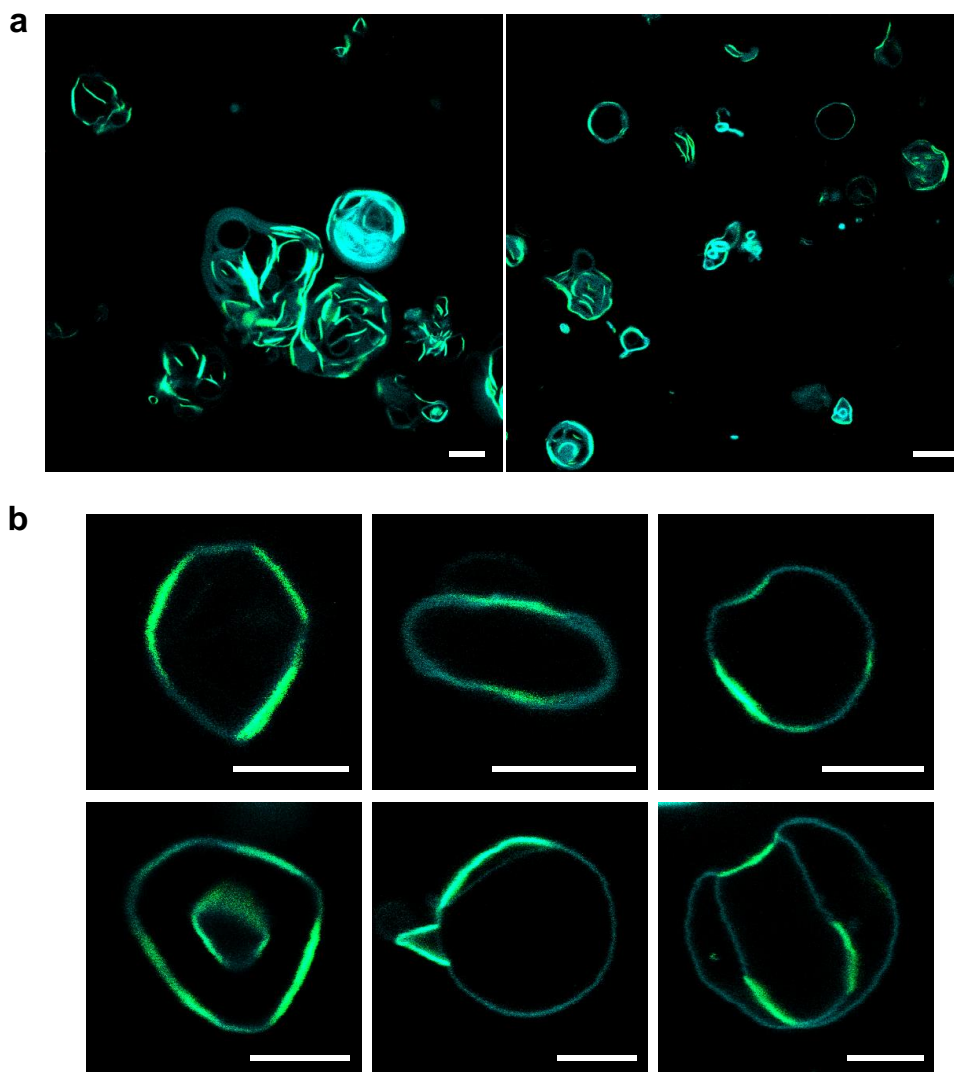
819  
820 We recorded CLSM images of a Laurdan solution in methanol (0.2 mg·mL<sup>-1</sup>) and the  
821 fluorescence spectrum in a spectrophotometer (FluoroMax, HORIBA). In both cases we  
822 obtained GP values of –0.98 and –0.96, respectively. Therefore, no correction multiplier was  
823 used for the calculation of GPs. The distribution of the obtained GP values was fitted to a  
824 Gaussian function, or the linear combination of two Gaussian functions in R.



825

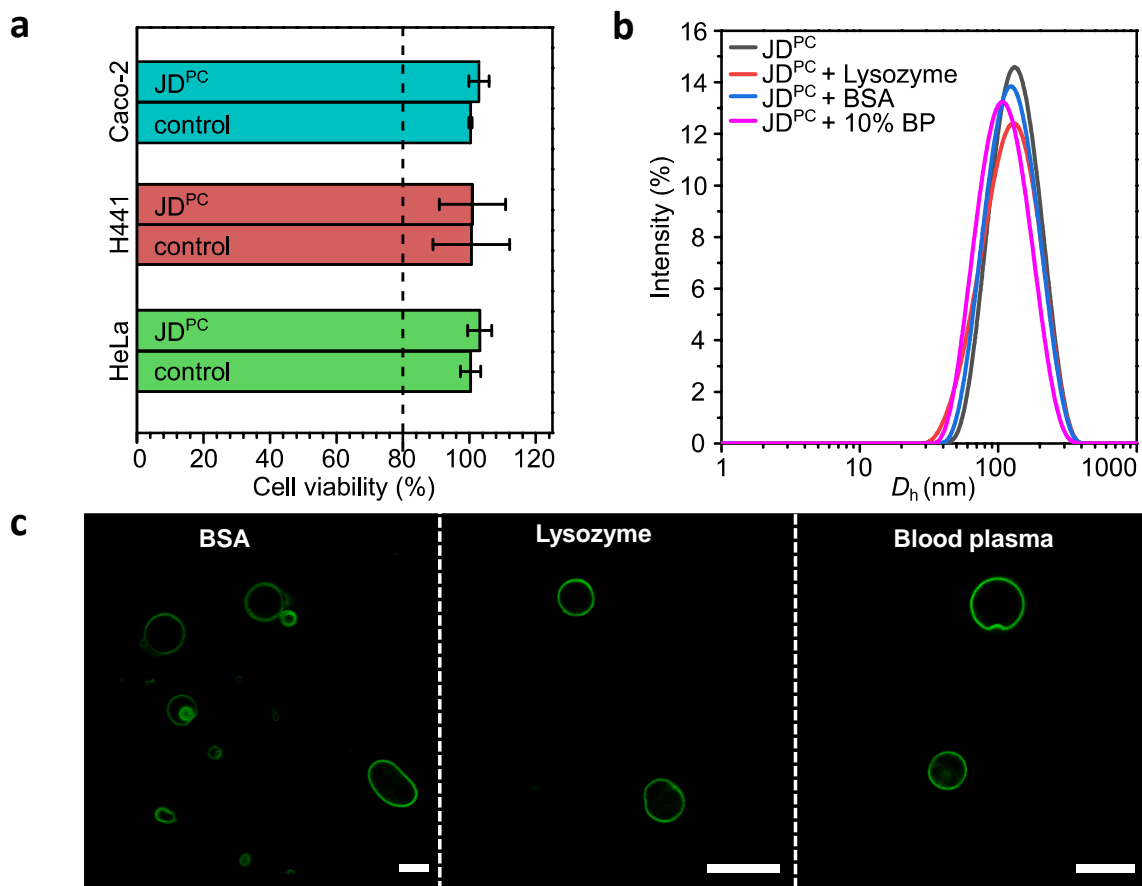
826 **Figure S27.** (1) Merged CLSM images of Laurdan emission detected at  $\lambda_1 = 415 - 445$  nm  
 827 (green) and  $\lambda_2 = 490 - 530$  nm (blue). Scale bars are  $5 \mu\text{m}$  (2) GP analysis of (1). (3) GP  
 828 distribution of Laurdan on the entire membrane. (a) Pure z-DSs and JD<sup>PC</sup>-Lipid hybrid vesicles  
 829 with (b) 20 mol% DLPC (C12), (c) 20 mol% DPPC (C16), (d) 20 mol% DSPC (C18), (e)  
 830 Distribution of the GP of Laurdan in the boxes depicted in d (2).

831



832  
833 **Figure S28.** CLSM imaging of vesicles composed of 80 mol% JD<sup>PC</sup> and 20 mol% DSPC (C18).  
834 (a) Overview images and (b) selected single vesicles depicting phase separation of the lipid and  
835 faceting of the vesicles. Laurdan emission was detected at  $\lambda_1 = 415 - 445$  nm (green) and  
836  $\lambda_2 = 490 - 530$  nm (blue). Scale bars are 10  $\mu\text{m}$  in (a) and 5  $\mu\text{m}$  in (b).  
837

## 4.15 Interaction with biological media

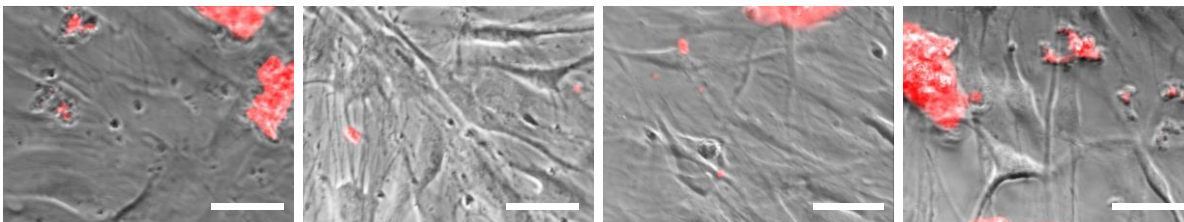
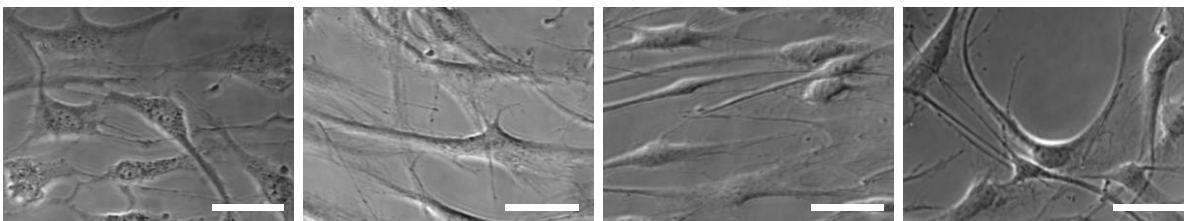
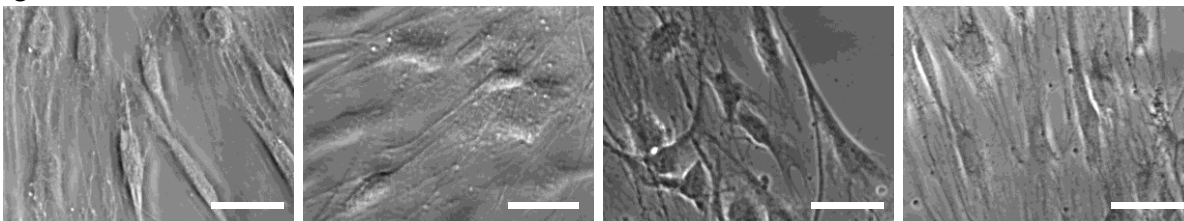


839  
 840 **Figure S29.** Compatibility of z-DSs with different biological media. (a) A standardized MTS  
 841 assay was performed with different cell-types. In all cases, cell viability after z-DS addition was  
 842 similar to the control samples where the same volume of water was added. (b)  $D_h$  of z-DSs  
 843 before and after incubation with different protein solutions for 24 h were determined by  
 844 dynamic light scattering. (c) CLSM images of z-DSs incubated with different protein solutions  
 845 for 30 min, labeled with Bodipy (0.5 mol%). Scale bars are 10  $\mu$ m.

846

847 **4.15.1 Interactions of z-DSs and Normal Human Dermal Fibroblasts (NHDF)**

848 Giant z-DSs were formed by thin-film hydration and their membrane was fluorescently labeled  
 849 with 1 mol% Liss Rhod-PE (red). z-DSs were mixed with cell culture medium (3:7) and added  
 850 to NHDFs. After 24 h of incubation at 37°C the chambers were imaged in phase contrast and  
 851 fluorescent mode. Figure S30a shows the presence of both fibroblasts and z-DSs after  $t = 24$  h.  
 852 After an additional washing step (Figure S30b) only living fibroblasts remained and no vesicles  
 853 were observed. The negative control sample where only Milli-Q water and culture medium  
 854 were mixed (3:7) displayed similar behavior. Thus, z-DSs do not attach or internalize into cells.

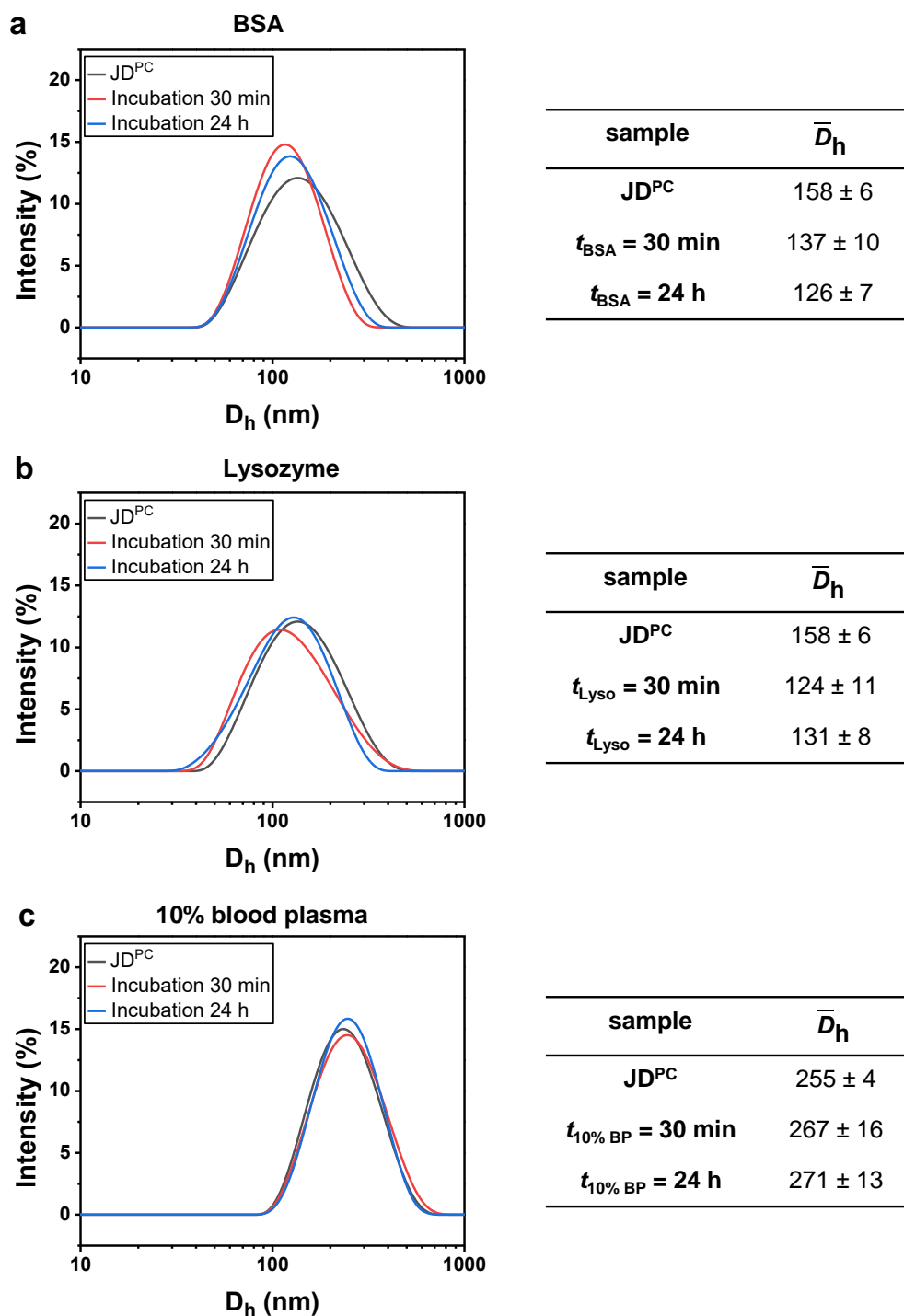
**a Before washing****b After washing****c Control water**

855  
856 **Figure S30.** Compatibility of z-DSs with normal human dermal fibroblasts (NHDF). z-DSs  
857 were incubated with cells for 24 h and imaged in phase contrast and fluorescence mode. a) Cells  
858 and fluorescently labeled z-DSs (1 mol% Liss Rhod-PE) are shown in contact before washing  
859 step and b) after washing showing only cells and no attached or internalized vesicles. c) Control  
860 sample with cells where only water was added. Scale bars are 50  $\mu\text{m}$ .

861

**4.15.1 DLS investigation of z-DSs compatibility in protein solutions**

862  
863 DLS was employed to study the stability of small z-DSs in contact with protein solutions. z-DSs  
864 were prepared by the injection method in HEPES. After measuring the vesicle dispersions, they  
865 were mixed with protein solutions of BSA, lysozyme and 10% blood plasma in HEPES buffer,  
866 respectively. After 30 min and subsequently 24 h, they were measured by DLS. All samples  
867 display no significant changes in the intensity distributions of the hydrodynamic diameter even  
868 after 24 h. The similar mean hydrodynamic diameters before and after protein incubation  
869 indicate that no significant aggregation or bursting of the z-DSs occurred.



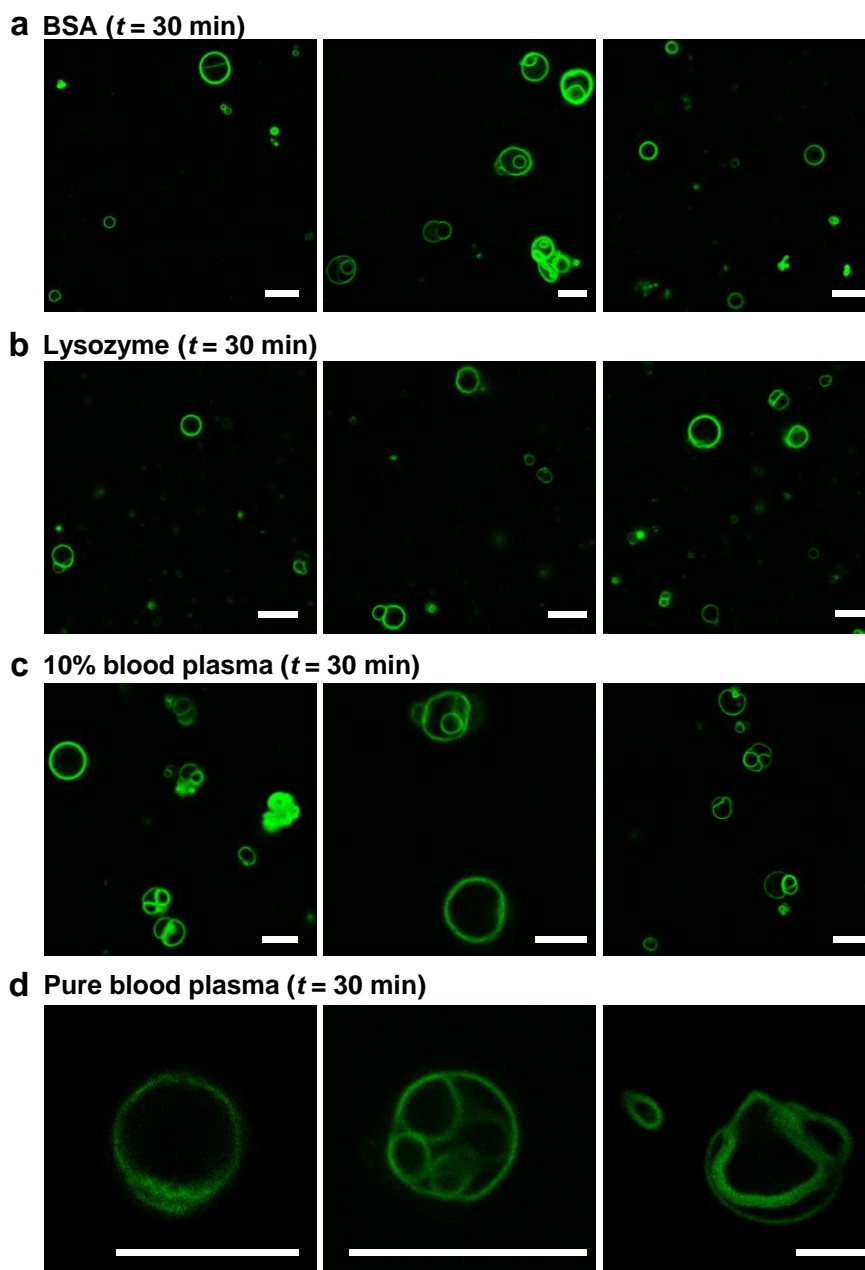
870

871 **Figure S31.** Intensity distribution of hydrodynamic diameters  $D_h$  were determined by DLS.  
 872 z-DSs were measured prior (black curves) to mixing with a) BSA, b) lysozyme and c) 10%  
 873 blood plasma in HEPES buffer. Red curves display the intensity distribution after 30 min  
 874 incubation, while blue curves are obtained after 24 h incubation. The tables on the right display  
 875 the determined mean diameter  $\bar{D}_h$  that was averaged over three measurements of the respective  
 876 samples.

877

878 **4.15.2 Compatibility of z-DSs prepared in 10 mM HEPES buffer with protein**  
879 **solutions**

880 z-DSs were formed in 10 mM HEPES buffer ( $c = 1 \text{ mg}\cdot\text{mL}^{-1}$ ) by thin-film hydration while  
881 labeling the membrane with 0.5 mol% Bodipy. BSA, lysozyme and 10% human blood plasma  
882 solutions were prepared in 10 mM HEPES. Afterwards, z-DS dispersion was mixed with  
883 solutions of BSA, lysozyme, 10% and 100% human blood plasma in a 1:1 v:v ratio, respectively.  
884 After  $t = 30 \text{ min}$ , vesicles were studied in CLSM (Figure S32). For BSA, lysozyme and 10%  
885 blood plasma, z-DSs remain unaffected, and we observed a high density of stable vesicles. In  
886 case of mixing with pure blood plasma, we observed only single vesicles – presumably due to  
887 the high osmotic pressure of the highly concentrated blood plasma. We therefore repeated the  
888 experiments with electroforming z-DSs in a sugar medium with a higher osmolarity to account  
889 for the osmotic difference. (Figure S33). We found that such vesicles showed an improved  
890 stability, even after an incubation time of  $t = 24 \text{ h}$  (Figure S34).



891  
892 **Figure S32.** Compatibility of z-DSs with different biological media. z-DSs were formed in  
893 10 mM HEPES buffer by thin-film hydration and mixed in a 1:1 v:v ratio with 100  $\mu$ M solutions  
894 of BSA, lysozyme, 10% and 100% human blood plasma. The mixtures were incubated for  
895 30 min prior to observation by CLSM indicating high stability of z-DSs in different biological  
896 media. The membrane was labeled with 0.5 mol% Bodipy. Scale bars are 20  $\mu$ m.  
897

## 4.15.3 Compatibility of z-DSs prepared in 300 mM sucrose with protein solutions

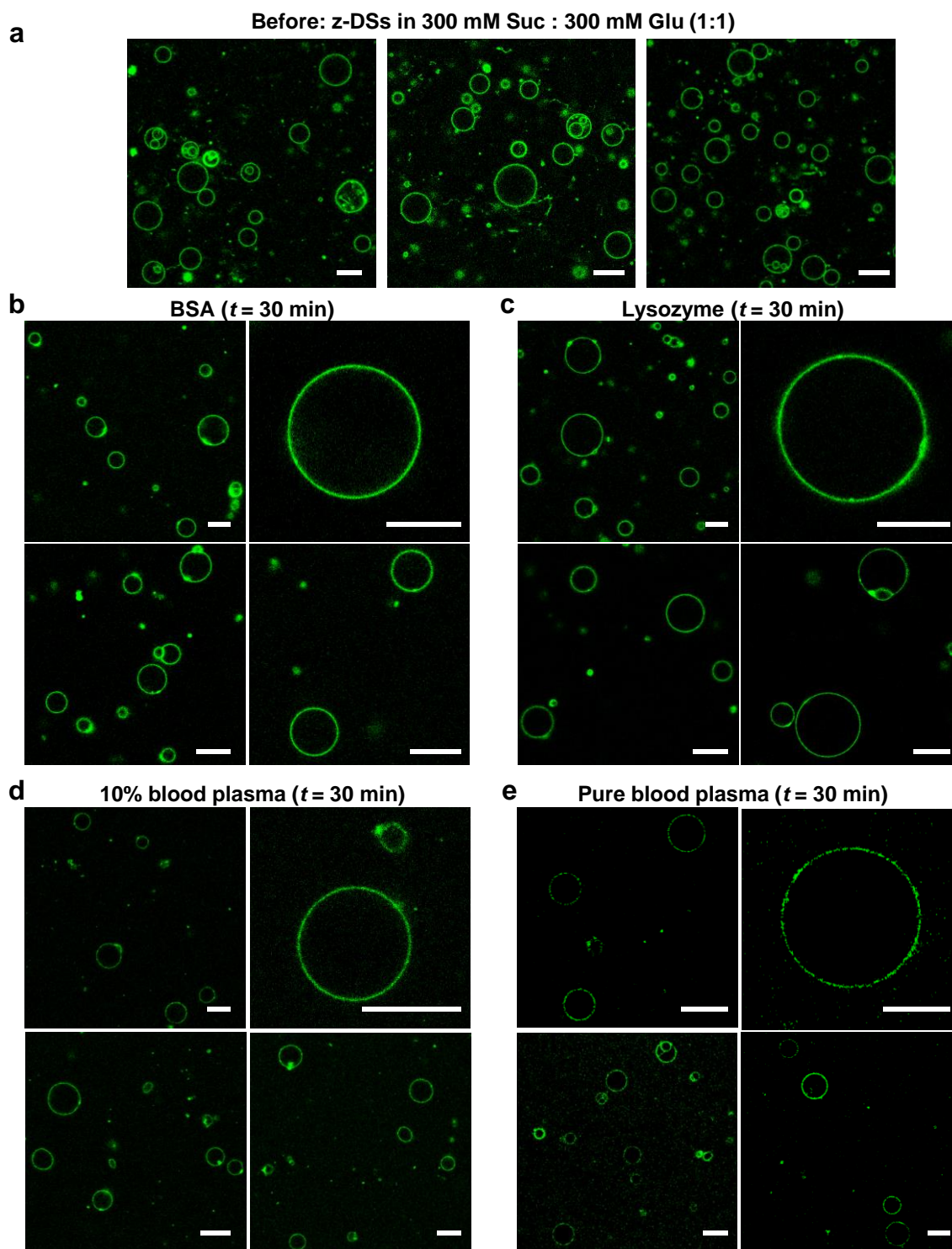
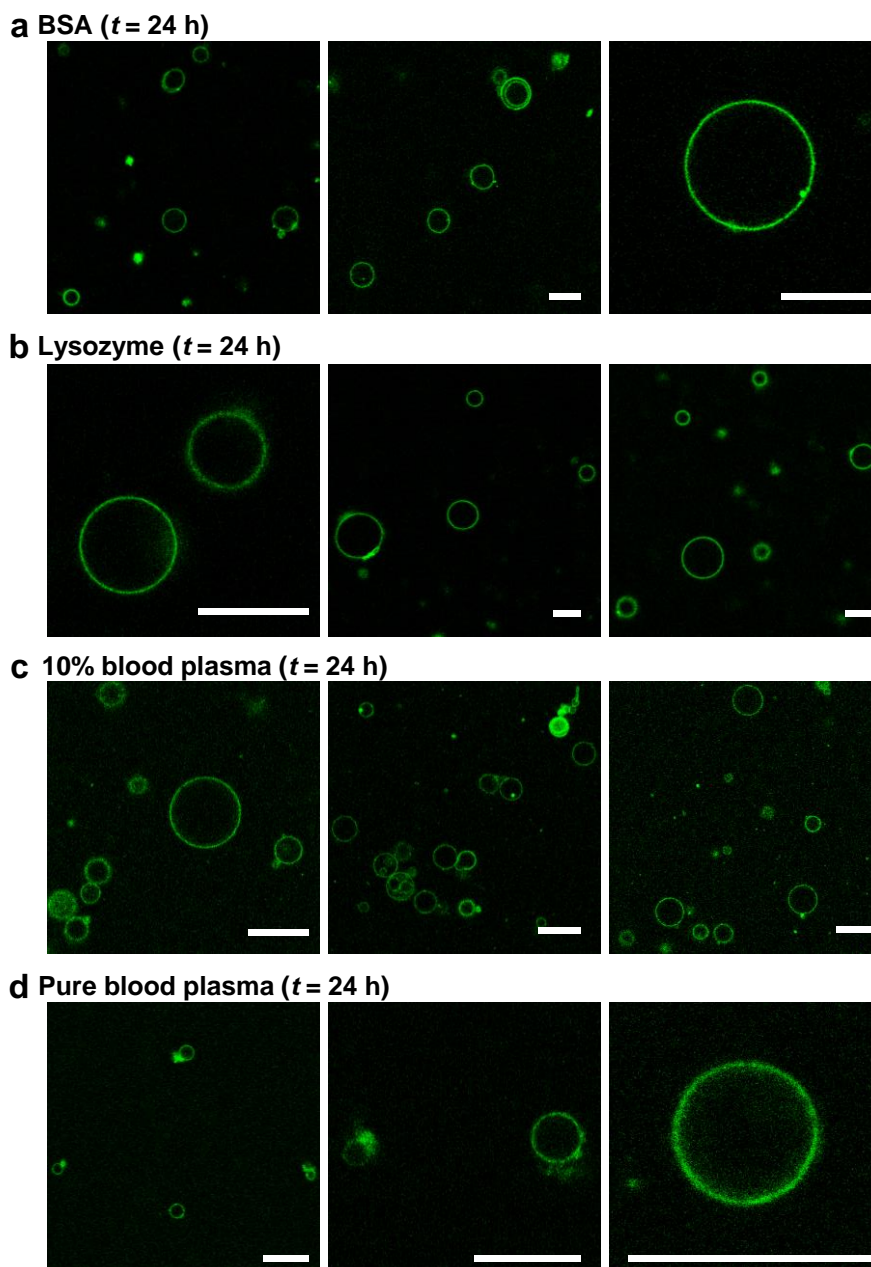


**Figure S33.** Compatibility of z-DSs with different biological media. z-DSs were assembled by  
 901 electroformation in 300 mM sucrose and mixed in a 1:1 v:v ratio with 100  $\mu$ M solutions of  
 902 BSA, lysozyme, 10% and 100% human blood plasma. Solutions of BSA, lysozyme and 10%  
 903 blood plasma were prepared in 300 mM glucose. The mixtures were incubated for 30 min prior  
 904 to observation by CLSM indicating high stability of z-DSs in different biological media. The  
 905 membrane was labeled with 0.5 mol% Bodipy. Scale bars are 20  $\mu$ m.



906

907 **Figure S34.** Compatibility of z-DSs with different biological media. z-DSs were electroformed908 in 300 mM sucrose and mixed in a 1:1 v:v ratio with 100  $\mu$ M solutions of BSA, lysozyme, 10%

909 and 100% human blood plasma. Solutions of BSA, lysozyme and 10% blood plasma were

910 prepared in 300 mM glucose. The mixtures were incubated for 24 h prior to observation by

911 CLSM indicating high long-term stability of z-DSs in different biological media. The

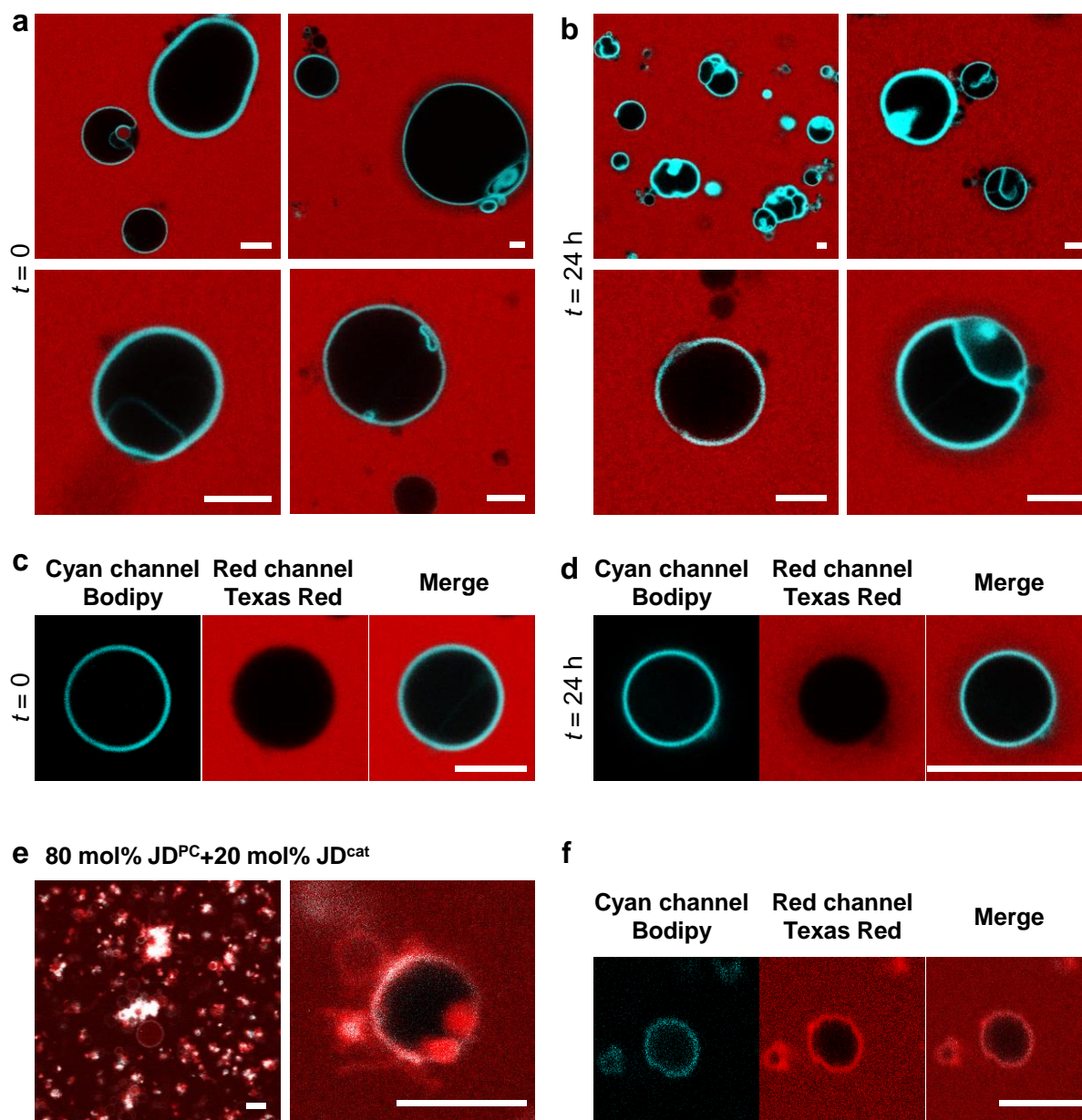
912 membrane was labeled with 0.5 mol% Bodipy. Scale bars are 20  $\mu$ m.

913

914 **4.15.4 Interactions of z-DSs and fluorescently labeled BSA**

915 We further studied z-DSs after incubation with fluorescently labeled BSA (Texas Red, red) in  
916 CLSM (Figure S35). z-DSs were formed in 10 mM HEPES by thin-film hydration while  
917 0.5 mol% Bodipy were added as a membrane label. The solution of labeled BSA was prepared  
918 in 10 mM HEPES with  $c_{\text{BSA}} = 6.6 \text{ mg}\cdot\text{mL}^{-1}$ . Immediately after mixing in a 1:1 v:v ratio ( $t = 0$ )  
919 and after  $t = 24 \text{ h}$ , we observed no increase in red fluorescence signal at the membrane revealing  
920 that no significant amounts of BSA had attached to the z-DSs, which remained stable.  
921 Additionally, we performed a control experiment where the membrane of the DSs is positively  
922 charged to force the adsorption of BSA. DSs were formed by co-assembly of  $\text{JD}^{\text{PC}}:\text{JD}^{\text{cat}}$  (8:2  
923 molar ratio) vesicles 10 mM HEPES by thin-film hydration and labeled with 0.5 mol% Bodipy.  
924 Immediately after contact with BSA, we observed changes in the shape and an increased red  
925 fluorescence signal at the membrane. The adsorption of proteins only at the external leaflet of  
926 the membrane not only causes the “protein corona” but drives strong deformation of the vesicles  
927 by changing the balance between the area of the external and internal leaflet. The lack of red  
928 fluorescence and the maintenance of the shape for z-DS assembled from only  $\text{JD}^{\text{PC}}$  support that  
929 their interface with water does not attract the proteins evaluated in this study.

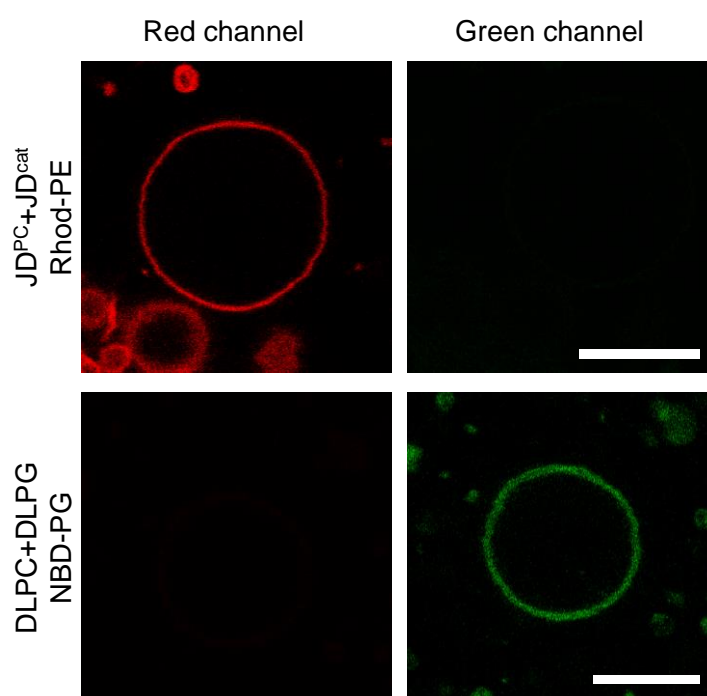
930



931  
 932 **Figure S35.** Compatibility of z-DSs with BSA. z-DSs were formed in 10 mM HEPES buffer  
 933 by thin-film hydration where a solution of fluorescently labeled BSA in 10 mM HEPES  
 934 ( $c_{\text{BSA}} = 6.6 \text{ mg}\cdot\text{mL}^{-1}$ ) was added in a 1:1 v:v ratio. z-DSs were imaged in CLSM a) immediately  
 935 after contact indicating no interactions between membrane and proteins where c) shows a single  
 936 vesicle with no increased fluorescence signal at the membrane in the Texas Red channel. b)  
 937 After 24 h of incubation time still no interactions could be observed with d) a unilamellar  
 938 vesicle with separate channels. e) 80 mol%  $\text{JD}^{\text{PC}}$  and 20 mol%  $\text{JD}^{\text{cat}}$  were co-assembled as a  
 939 control sample showing strong interactions between the positively charged membrane and the  
 940 labeled BSA with f) showing a single unilamellar vesicle with both overlapping fluorescence  
 941 signals at the membrane. z-DSs were labeled with 0.5 mol% Bodipy (cyan) and BSA was  
 942 labeled with Texas Red (red). Scale bars are 5  $\mu\text{m}$ .

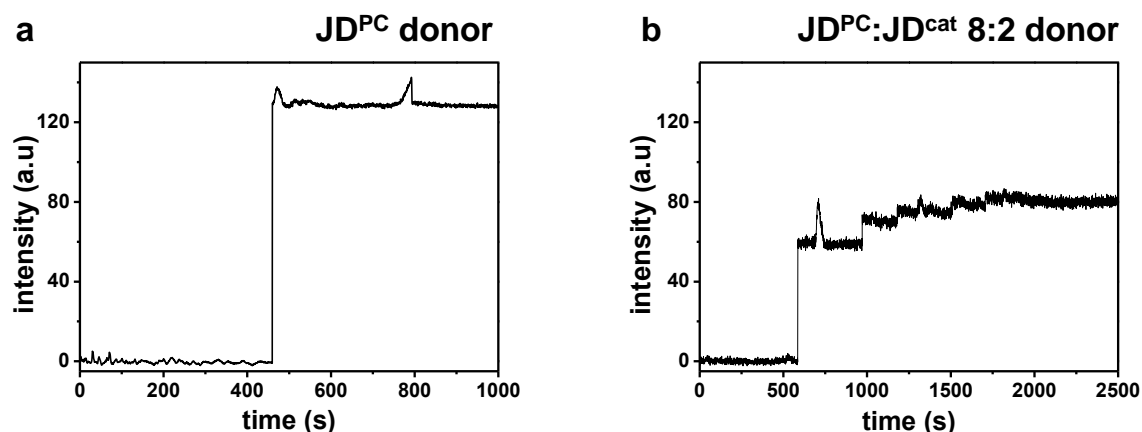
943 **4.16 Fusion with liposomes**

944 In the following section we assessed fusion using CSLM and the increase in fluorescent  
 945 intensity when FRET dyes dequenched during fusion using fluorescence spectroscopy. In  
 946 CLSM a dispersion of giant DSs was mixed with giant liposomes (both prepared by thin-film  
 947 hydration) in a 1:1 v:v ratio and observed immediately after mixing and after prolonged  
 948 incubation times ( $t = 4$  h, Figure S39). Firstly, to exclude any effects of crosstalk of the dyes  
 949 used in the fusion between positively charged dendrimersomes and negatively charged  
 950 liposomes in CLSM, we performed control experiments. Observing both samples separately, it  
 951 was evident that dendrimersomes only showed a fluorescence signal in the red channel and  
 952 liposomes in the green channel. Therefore, we rule out any crosstalk in our experimental design.



953 **Figure S36.** Control experiments to investigate crosstalk of fluorescently labeled lipids. z-DSs  
 954 were labelled with 1 mol% Liss Rhod-PE and liposomes were labeled with 1 mol% NBD-PC.  
 955 Scale bars are 10  $\mu\text{m}$ .  
 956

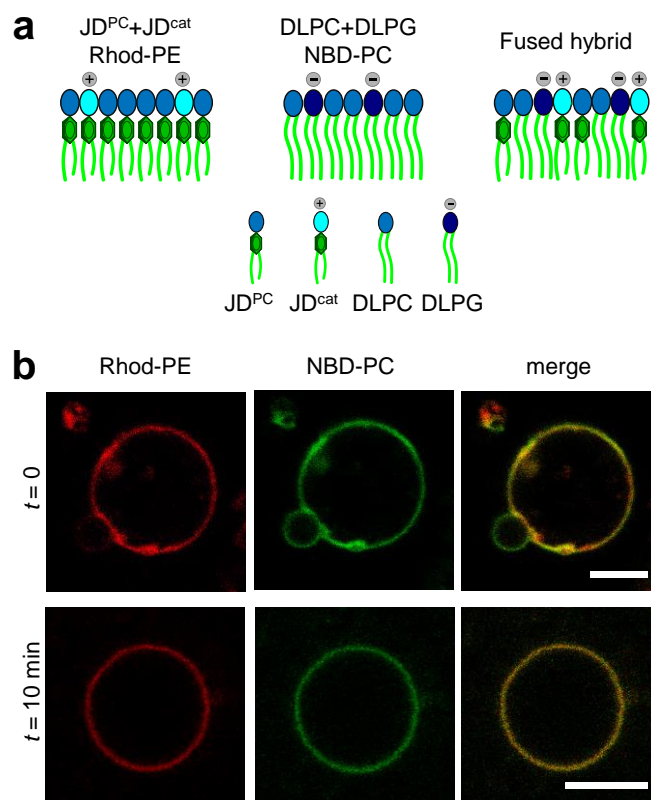
957  
 958 For a quantitative assessment of the global behavior, we used FRET by fluorescence  
 959 spectroscopy. For this we prepared DSs donors containing two FRET dyes. After addition of  
 960 non-labeled liposome acceptors, we studied the increase in fluorescence intensity that occurs  
 961 during fusion and a dequenching of the dyes. The maximum intensity was defined as the  
 962 intensity reached upon addition of Triton X to the respective donors (Figure S37).



963  
 964 **Figure S37.** Maximum fluorescence intensity was obtained by solubilizing all amphiphiles of  
 965 donor vesicles upon addition of Triton X in a) JD<sup>PC</sup> donor vesicles and b) JD<sup>PC</sup>-JD<sup>cat</sup> (8:2) donor  
 966 vesicles. In a) 50  $\mu$ l of Triton X was added while Triton X was added in 5x 10  $\mu$ L steps in b).  
 967

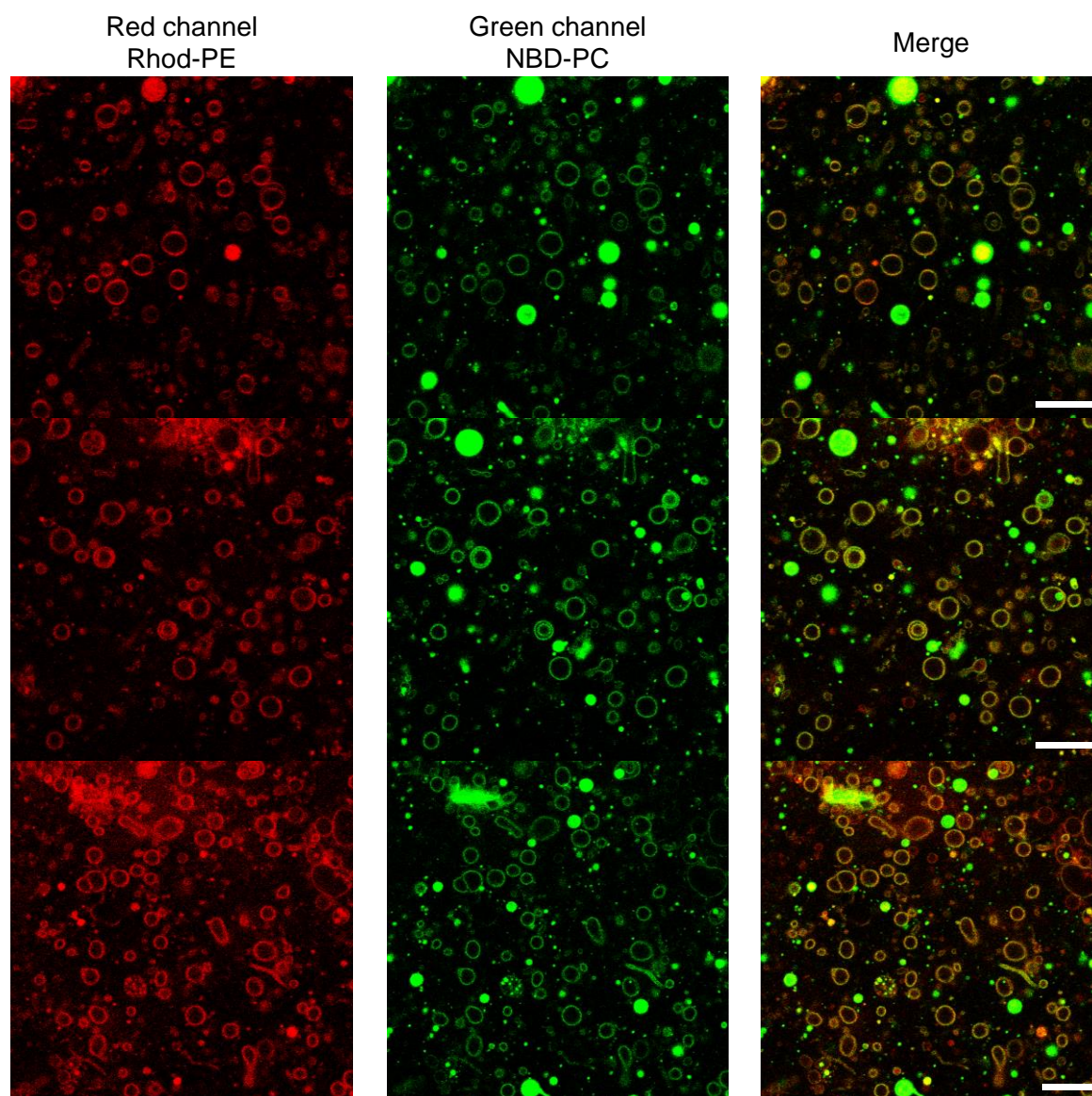
#### 968 4.16.1 Fusion of charged giant z-DSs with charged liposomes

969 Firstly, we studied the interactions of positively charged JD<sup>PC</sup>:JD<sup>cat</sup> (8:2 molar ratio) DSs  
 970 (labeled with Liss Rhod-PE, red) with negatively charged DLPC:DLPG (8:2) liposomes  
 971 (labeled with NBD-PC, green) in CLSM. Upon mixing both vesicle dispersions in a 1:1 v:v  
 972 ratio, adhesion between DSs and liposomes occurs, visualized by the distinctly different  
 973 fluorescence of the systems. It was possible to visualize the docking of the vesicles before  
 974 fusion. After a few minutes, we observe unilamellar vesicles with no additionally attached  
 975 vesicles that display fluorescence in both channels. These results demonstrate successful fusion  
 976 and incorporation of both dyes inside the generated JD-lipid hybrid vesicles (Figure S38).



977

978 **Figure S38.** Charge mediated fusion of DSs with liposomes. (a) Scheme demonstrating the  
 979 coassembly of the charged DSs and liposomes. DSs are assembled from JD<sup>PC</sup> and 20 mol% of  
 980 cationic JD<sup>cat</sup> and labeled with Liss Rhod-PE (red, 1 mol%) while liposomes are formed from  
 981 DLPC and 20 mol% of anionic DLPG and labeled with NBD-PC (green, 1 mol%). (b)  
 982 Representative CLSM images of liposomes fusing with a DS immediately after mixing (*t* = 0)  
 983 and after *t* = 10 min. Left column: Liss Rhod-PE channel (red), middle column: NBD-PC  
 984 channel (green) and right column: merged fluorescence. Scale bars are 5 μm. The vesicles in  
 985 the top and bottom rows are different ones but representative at a given time point.



986

987 **Figure S39.** CLSM overviews with separate channels after  $t = 4$  h of mixing positively charged  
 988  $\text{JD}^{\text{PC}}\text{-JD}^{\text{cat}}$  (8:2) DSs (1 mol% Liss Rhod-PE, red) and negatively charged DLPC-DLPG (8:2)  
 989 liposomes (1 mol% NBD-PC, green). Scale bars are 20  $\mu\text{m}$ .

990

991 **Table S6.** Calculation of fusion efficiency of fusion 1 ( $\text{JD}^{\text{PC}}\text{:JD}^{\text{cat}} + \text{DLPC:DLPG}$ ) and fusion  
 992 2 ( $\text{JD}^{\text{PC}}\text{:JD}^{\text{cat}} + \text{DLPC}$ ) as the ratio of fused vesicles to all theoretical possible fusion events.  
 993 The latter was calculated as the sum of fused vesicles and remaining smaller population of  
 994 unfused vesicles. Analysis was performed using CLSM images.

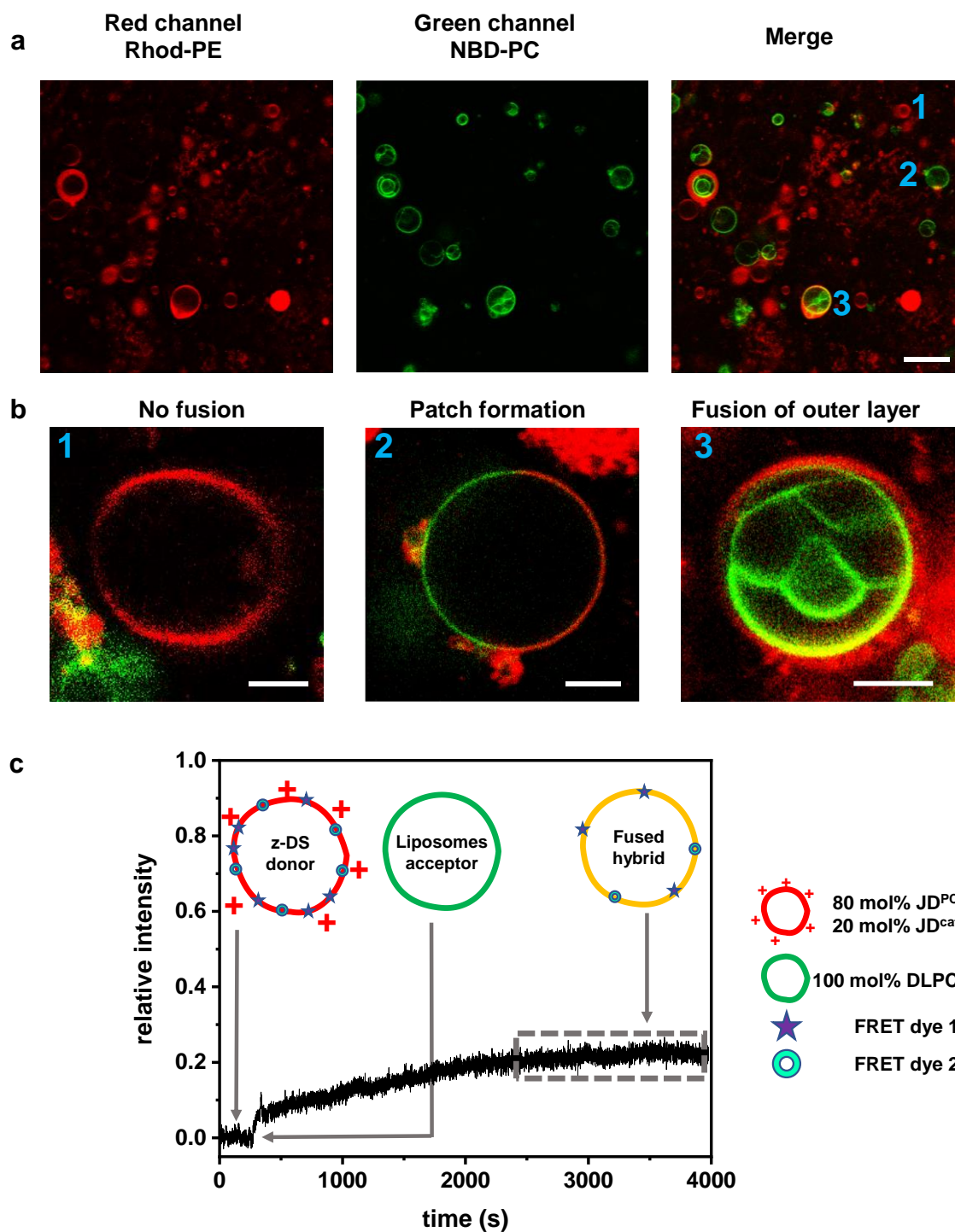
	Not fused (green)	Not fused (red)	Fused	Total vesicles	Fusion efficiency (%)
<b>Fusion 1</b>	85	25	300	410	92
<b>Fusion 2</b>	125	145	74	344	37

995

**996 4.16.2 Fusion of charged giant z-DSs with neutral liposomes**

997 We investigated whether fusion occurs if only the z-DSs had explicit charge (Figure S40).  
998 Therefore, DSs were assembled from JD<sup>PC</sup>:JD<sup>cat</sup> (8:2) (Liss Rhod-PE, red) to yield a cationic  
999 interface. These DSs were mixed with neutral DLPC liposomes (NBD-PC, green) and observed  
1000 in CLSM. At  $t = 0$ , three outcomes could be distinguished: (1) vesicles with one fluorescence  
1001 signal indicating no fusion, (2) patch formation (intermediate of fusion) and (3) vesicles with  
1002 an overlap of both fluorescence signals in the outer layer demonstrating full fusion (Figure  
1003 S40b). By analyzing 344 vesicles in several CLSM images, we calculated a fusion efficiency  
1004 of 37% (Table S6).

1005 These studies were further supported by FRET, which allows to assess the kinetics of fusion of  
1006 the whole population of vesicles in the sample. We observed an increase in fluorescence  
1007 intensity upon addition of neutral liposomes (Figure S40c) indicating fusion and dequenching.  
1008 Contrary to the previous case of the charge mediated fusion process, the plateau in the  
1009 fluorescent intensity only reached a lower relative intensity of 20%.

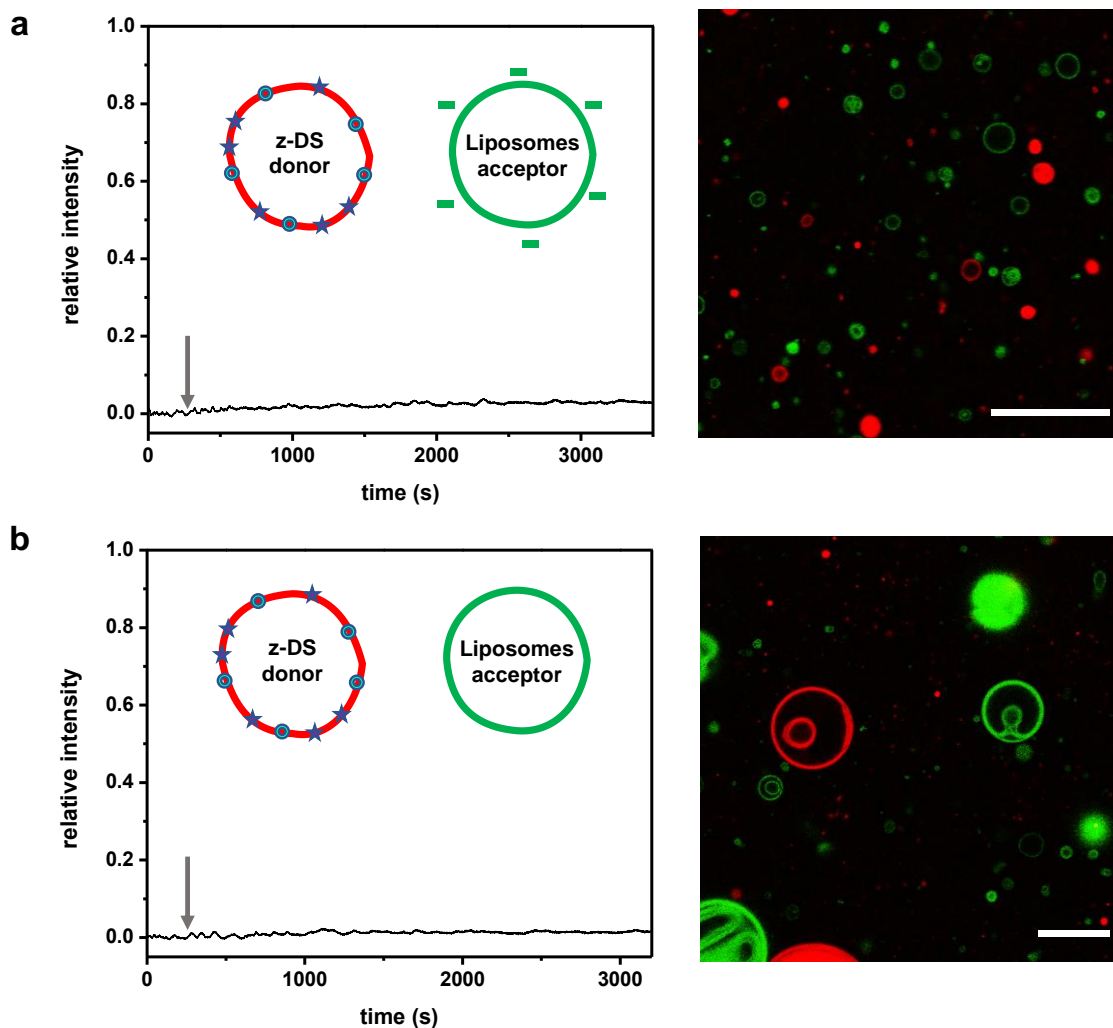


1010

1011 **Figure S40.** Charge-mediated fusion of DSs with liposomes. (a) CLSM overview after mixing  
 1012 of positively charged JD<sup>PC</sup>:JD<sup>cat</sup> (8:2) DSs (1 mol% Liss Rhod-PE, red) and neutral DLPC  
 1013 liposomes (1 mol% NBD-PC, green). (b) Selected vesicles showing (1) no fusion, (2) patch  
 1014 formation or (3) fusion of the outer layers. (c) A large population of vesicles was studied by  
 1015 FRET using fluorescence spectroscopy where the donor contains both FRET dyes. Upon  
 1016 addition of acceptor vesicles, a fluorescence increase was detected consistent with the formation  
 1017 of fused hybrids. Scale bar is 20  $\mu\text{m}$  in a and 5  $\mu\text{m}$  in b.

1018 **4.16.3 Fusion of neutral giant z-DSs with neutral or negatively charged liposomes**

1019 Lastly, we studied the behavior of a mixture of neutral z-DSs and negatively charged liposomes  
 1020 (DLPC:DLPG 8:2) (Figure S41a) or neutral z-DSs and neutral liposomes (DLPC) (Figure  
 1021 S41b). Figure 4 (FRET fluorescent) shows no increase in the fluorescence intensity upon  
 1022 addition of acceptors liposomes (negative or neutral) to the z-DSs donor vesicles. Examination  
 1023 of CSLM images further support these results as no vesicle having both colors could be  
 1024 observed. Thus, no fusion was observed if  $JD^{cat}$  was not part of the membrane of the DSs.



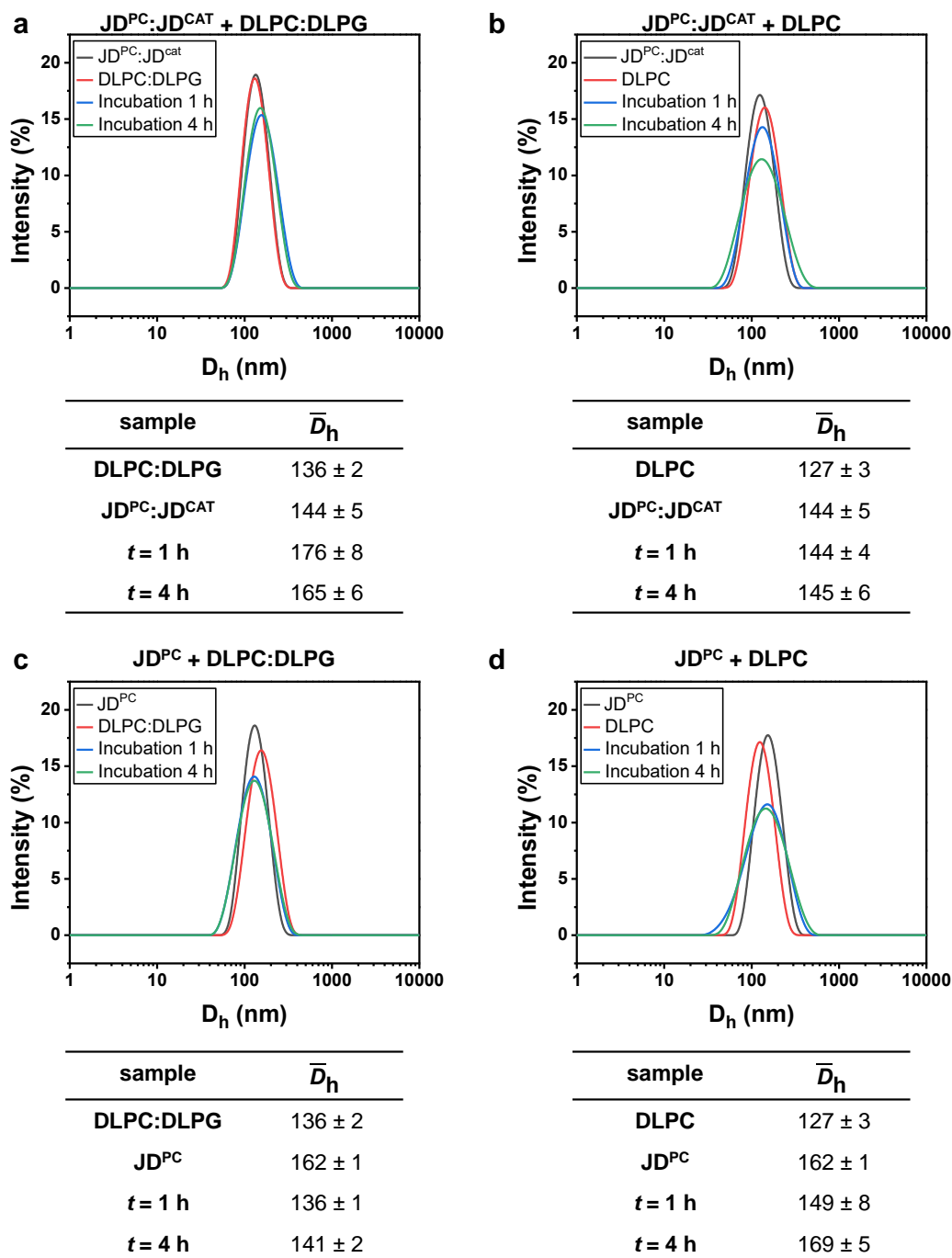
1025 **Figure S41.** Control experiments of a) neutral DSs ( $JD^{PC}$ ) and negatively charged liposomes  
 1026 (DLPC:DLPG 8:2) or b) mixing neutral  $JD^{PC}$  DSs and neutral liposomes (DLPC). DSs are  
 1027 labeled with 1 mol% Liss Rhod-PE (red) and liposomes with 1 mol% NBD-PC (green). The  
 1028 grey arrow indicates the time point at which acceptor vesicles were added. Both populations  
 1029 were studied by FRET using fluorescence spectroscopy (left) showing no significant increase  
 1030 in relative fluorescence intensity and CSLM (right) showing no overlap in the fluorescence  
 1031 signals. Scale bars are 20 μm.

1033 **4.16.4 Fusion of Small Unilamellar Vesicles (SUVs) by DLS**

1034 We also assessed the fusion of SUVs using DLS. This allows for identifying differences (if any)  
1035 with GUVs (previous section). Moreover, DLS allows for a global picture of the process. SUV  
1036 with homogeneous size were prepared using extrusion method. Briefly, vesicles were  
1037 assembled by the extrusion method to yield vesicles with a narrow size distribution of the  
1038 vesicles ( $PDI < 0.09$ ). Charged vesicles were co-assembled in an 8:2 molar ratio of uncharged  
1039 to charged species. Firstly, we determine the size distribution of each vesicle dispersion. Then,  
1040 we mixed the dispersion to assess the fusion. In all experiments we mixed the same volumes of  
1041 each type (500  $\mu\text{L}$  per dispersion). This is to favor binary fusion. DLS of the resulting  
1042 dispersions were measured after 1 h and 4 h of incubation. We compared the resulting sizes  
1043 with two limiting conditions: (a) conservation of area upon fusion and (b) conservation of  
1044 volume. In the former, the expected diameter after fusion can be estimated  
1045  $D_A = (D_{h,1}^2 + D_{h,2}^2)^{1/2}$  where  $D_A$  is the calculated diameter if membrane area is conserved,  $D_{h,1}$   
1046 and  $D_{h,2}$  denote the mean diameter of the respective vesicles prior to mixing.<sup>[22]</sup> For volume  
1047 conservation  $D_V = (D_{h,1}^3 + D_{h,2}^3)^{1/3}$  where  $D_V$  is the diameter estimated assuming volume  
1048 conservation.

1049 Only in the case of mixing cationic DSs and anionic liposomes did we observe an overall shift  
1050 of the intensity distribution to larger hydrodynamic diameter and a concomitant increase in  
1051 mean peak intensity. The resulting diameter of 176 nm after 1 h incubation is lower than the  
1052 expected  $D_A$  of 198 nm. Instead, it matches the expected  $D_V$  of 177 nm, which is in line with  
1053 previous observations of charge-mediated fusion between polymersome-liposome hybrids.<sup>[22]</sup>  
1054 Increasing the incubation time to 4 h did not lead in further increase in mean diameter,  
1055 indicating that most fusion events occurred during the first hour of incubation. Importantly, we  
1056 did not observe additional populations with larger hydrodynamic diameter, indicating that  
1057 overall mostly binary fusion events occurred.

1058 The lack of size increase between uncharged z-DSs and anionic liposomes (c), as well as  
1059 uncharged z-DSs and liposomes (d) is in agreement with the lack of fusion events that we  
1060 observed in our CLSM and FRET studies for giant vesicles. Although we detected fusion events  
1061 between cationic z-DSs and uncharged liposomes in these studies, we attribute the lack of size  
1062 increase in DLS for this sample to the lower efficiency of fusion that we observed in those  
1063 experiments (see sections 4.16.1 to 4.16.3).

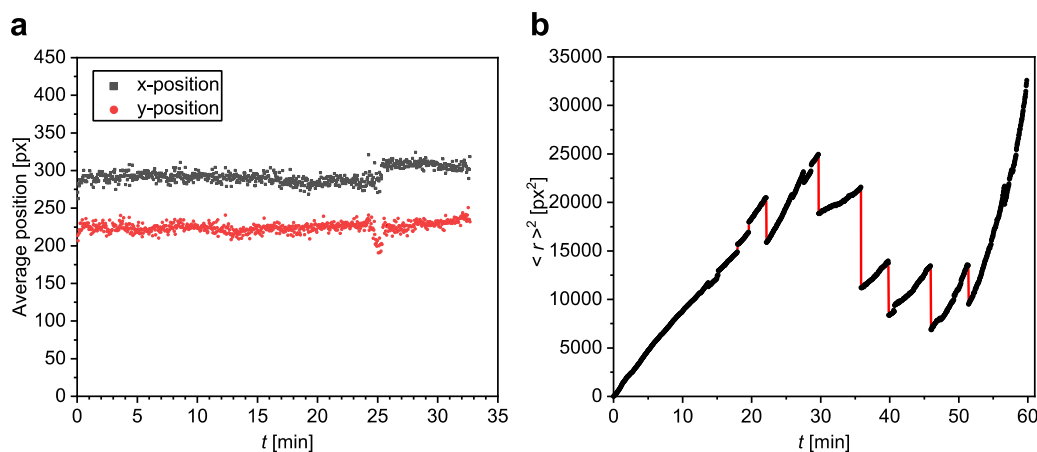


1064

1065 **Figure S42.** Fusion behavior of DSs and small liposomes studied by DLS. Vesicles were  
 1066 prepared by the extrusion method to obtain small vesicles with narrow size distributions where  
 1067  $\text{PDI} < 0.09$ . DSs (black curves) and liposomes (red curves) were measured prior to mixing and  
 1068 incubation. The mixed vesicle dispersions were measured after 1 h of incubation (blue curves)  
 1069 and subsequently after 4 h (green curves). Mixed vesicle dispersions of a) cationic DSs and  
 1070 anionic liposomes, b) cationic DSs and neutral liposomes, c) neutral DSs and anionic liposomes,  
 1071 as well as d) neutral DSs and neutral liposomes were investigated. The tables below each graph  
 1072 display the determined mean diameter  $\bar{D}_h$  that was averaged over three measurements of the  
 1073 respective samples.

1074

## 4.17 Motility of z-DSs



1075

1076

1077

1078

1079

1080

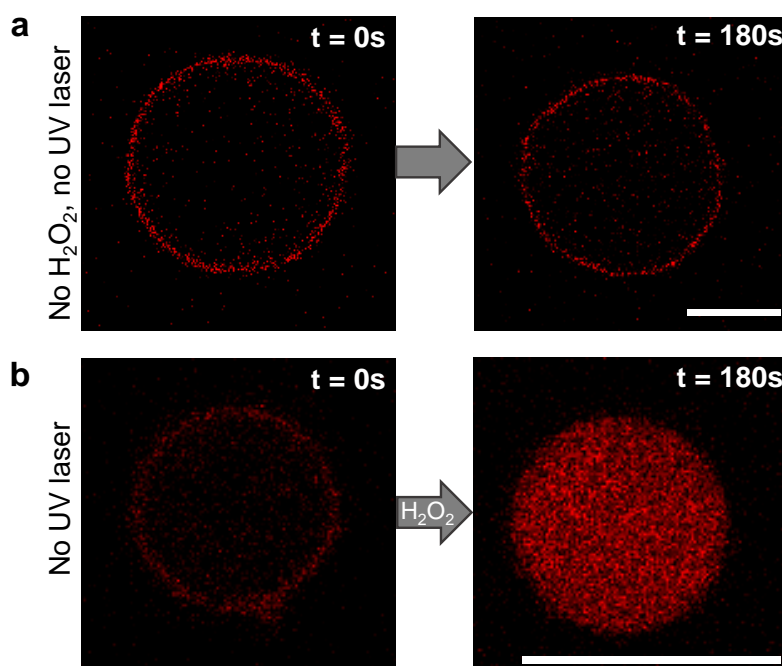
1081

1082

**Figure S43.** (a) The ensemble average position of the vesicles in the x (black) and y coordinate (red) remained unchanged, when no H<sub>2</sub>O<sub>2</sub> was present in the solution. (b) Mean square displacement  $\langle r^2 \rangle$  of catalase-filled z-DSs over time after addition of H<sub>2</sub>O<sub>2</sub> and incubation for 10 minutes. No parabolic component was observed, demonstrating that the motion is not convective. The broken segments in between (red lines) indicate the driven motion in random directions.

1083 **4.18 Biosensing of hydrogen peroxide**

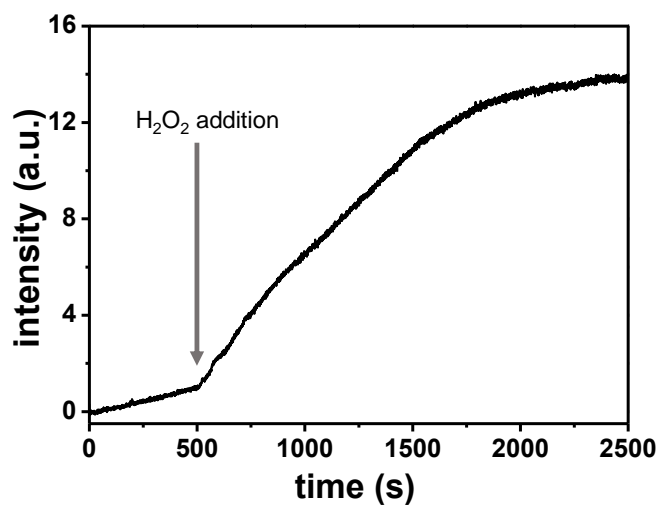
1084 z-DSs displayed red fluorescence within 180 s after H<sub>2</sub>O<sub>2</sub> addition (Figure S44) while no such  
 1085 fluorescence was detected in the same timeframe for z-DSs with no added H<sub>2</sub>O<sub>2</sub>.



1086  
 1087 **Figure S44.** Control experiments to investigate the effect of hydrogen peroxide and the red  
 1088 laser ( $\lambda = 488$  nm) on the formation of the red fluorescent DNA-E complex. (a) No fluorescence  
 1089 in the vesicle lumen was detected when no hydrogen peroxide was added in the external  
 1090 solution and no UV laser was used. (b) Red fluorescence was detected in the vesicle lumen after  
 1091 addition of hydrogen peroxide in the external solution while no UV laser was used. Scale bars  
 1092 are 10  $\mu$ m.

1093  
 1094 We further assessed the biosensing ability of the whole population of z-DSs by monitoring the  
 1095 global fluorescent intensity using a fluorometer. This allows for detection of smaller H<sub>2</sub>O<sub>2</sub>  
 1096 concentrations. Vesicles containing DNA, horseradish peroxidase and DHE in their lumen were  
 1097 prepared by electroformation in the same manner as for biosensing studies by CLSM. However,  
 1098 instead of Laurdan 1 mol% 633 Atto DOPE label was used to observe intact vesicles prior to  
 1099 measurements and prevent possible crosstalk of Laurdan in fluorescence spectroscopy. The  
 1100 resulting vesicles were purified in the same manner as described for CLSM biosensing studies.  
 1101 10  $\mu$ L of the vesicle dispersion were added to 2.5 mL of a 30  $\mu$ M DHE solution in 100 mM  
 1102 sucrose and incubated for 15 min in the dark prior to fluorescence spectroscopy measurements.  
 1103 During the initial 500 s, we observed a small continuous increase in fluorescence intensity over  
 1104 time, possibly due to slow degradation of the dye during irradiation. Upon addition of 10  $\mu$ L

1105  $\text{H}_2\text{O}_2$  (0.03 wt.%) at the 500 s mark, we observe a steep increase in fluorescence which reaches  
1106 a plateau after 2500s. Under these experimental conditions we could detect a  $\text{H}_2\text{O}_2$   
1107 concentration as low as 35  $\mu\text{M}$ .



1108  
1109 **Figure S45.** z-DSs are utilized as a biosensor. Within z-DSs we encapsulated DNA, horseradish  
1110 peroxidase (HRP) and dihydroethidium (DHE). Upon addition of membrane permeable  
1111 hydrogen peroxide (35  $\mu\text{M}$ ) at 500 s, a red colored DNA-E complex is formed within the vesicle  
1112 lumen consistent with an increase in the fluorescence intensity. The generation of red  
1113 fluorescence within the lumen was monitored using fluorescence spectroscopy.

## 1114 5. References

- 1115
- 1116 [1] G. R. Fulmer, A. J. M. Miller, N. H. Sherden, H. E. Gottlieb, A. Nudelman, B. M.  
1117 Stoltz, J. E. Bercaw, K. I. Goldberg, *Organometallics* **2010**, 29, 2176.
- 1118 [2] R. Dimova, *Annu. Rev. Biophys.* **2019**, 48, 93.
- 1119 [3] D. Nečas, P. Klapetek, *Open Phys.* **2012**, 10, 181.
- 1120 [4] E. Migliorini, P. Horn, T. Haraszti, S. V. Wegner, C. Hiepen, P. Knaus, R. P. Richter,  
1121 E. A. Cavalcanti-Adam, *Adv. Biosyst.* **2017**, 1, 1600041.
- 1122 [5] a) R. S. Gracià, N. Bezlyepkina, R. L. Knorr, R. Lipowsky, R. Dimova, *Soft Matter*  
1123 **2010**, 6, 1472; b) H. A. Faizi, C. J. Reeves, V. N. Georgiev, P. M. Vlahovska, R. Dimova,  
1124 *Soft Matter* **2020**, 16, 8996.
- 1125 [6] J. R. Henriksen, J. H. Ipsen, *Eur. Phys. J. E* **2002**, 9, 365.
- 1126 [7] a) T. Portet, R. Dimova, *Biophys. J.* **2010**, 99, 3264; b) F. S. C. Leomil, M. Zoccoler,  
1127 R. Dimova, K. A. Riske, *Bioinform. adv.* **2021**, 1, 1.
- 1128 [8] a) F. Brochard-Wyart, P. G. De Gennes, O. Sandre, *Phys. A: Stat. Mech. Appl.* **2000**,  
1129 278, 32; b) O. Sandre, L. Moreaux, F. Brochard-Wyart, *Proc. Natl. Acad. Sci. U.S.A.* **1999**,  
1130 96, 10591.
- 1131 [9] J. Mazurkiewicz, P. Tomasik, J. Zapłotny, *Food Hydrocolloids* **2001**, 15, 43.
- 1132 [10] S. Dedisch, F. Obstals, A. Los Santos Pereira, M. Bruns, F. Jakob, U. Schwaneberg, C.  
1133 Rodriguez - Emmenegger, *Advanced Materials Interfaces* **2019**, 6, 1900847.
- 1134 [11] *Perry's Chemical Engineers' Handbook*, McGraw-Hill Education, New York **2019**.
- 1135 [12] J. C. Crocker, D. G. Grier, *J. Colloid Interface Sci.* **1996**, 179, 298.
- 1136 [13] J. R. Henriksen, J. H. Ipsen, *Eur. Phys. J. E* **2004**, 14, 149.
- 1137 [14] D. S. Janni, K. M. Manheri, *Langmuir* **2013**, 29, 15182.
- 1138 [15] J. Ropponen, S. Nummelin, K. Rissanen, *Org. Lett.* **2004**, 6, 2495.
- 1139 [16] V. Percec, D. A. Wilson, P. Leowanawat, C. J. Wilson, A. D. Hughes, M. S. Kaucher,  
1140 D. A. Hammer, D. H. Levine, A. J. Kim, F. S. Bates, K. P. Davis, T. P. Lodge, M. L. Klein,  
1141 R. H. DeVane, E. Aqad, B. M. Rosen, A. O. Argintaru, M. J. Sienkowska, K. Rissanen, S.  
1142 Nummelin, J. Ropponen, *Science* **2010**, 328, 1009.
- 1143 [17] a) Y. G. Kang, J. W. Shin, S. H. Park, M.-J. Oh, H. S. Park, J.-W. Shin, S.-H. Kim,  
1144 *PLoS ONE* **2014**, 9, e93023; b) R. Fan, T. Emery, Y. Zhang, Y. Xia, J. Sun, J. Wan, *Scientific*  
1145 *Reports* **2016**, 6, 27073; c) B. Lopez-Mila, P. Alves, T. Riedel, B. Dittrich, F. Mergulhao, C.  
1146 Rodriguez-Emmenegger, *Bioinspir Biomim* **2018**, 13, 065001; d) Y. Wang, I. Pierce, P.  
1147 Gatehouse, N. Wood, D. Firmin, X. Y. Xu, *Med. Eng. Phys.* **2012**, 34, 17.
- 1148 [18] a) J. D. Hunter, *Comput Sci Eng.* **2007**, 9, 90; b) C. R. Harris, K. J. Millman, S. J. van  
1149 der Walt, R. Gommers, P. Virtanen, D. Cournapeau, E. Wieser, J. Taylor, S. Berg, N. J.  
1150 Smith, R. Kern, M. Picus, S. Hoyer, M. H. van Kerkwijk, M. Brett, A. Haldane, J. F. Del Rio,  
1151 M. Wiebe, P. Peterson, P. Gerard-Marchant, K. Sheppard, T. Reddy, W. Weckesser, H.  
1152 Abbasi, C. Gohlke, T. E. Oliphant, *Nature* **2020**, 585, 357.
- 1153 [19] C. A. Schneider, W. S. Rasband, K. W. Eliceiri, *Nat. Methods* **2012**, 9, 671.
- 1154 [20] N. Otsu, *IEEE Trans. Syst. Man Cybern.: Syst.* **1979**, 9, 62.
- 1155 [21] a) H. P. Duwe, E. Sackmann, *Phys. A: Stat. Mech. Appl* **1990**, 163, 410; b) R. Dimova,  
1156 *Adv. Colloid Interface Sci.* **2014**, 208, 225.
- 1157 [22] N. Marušič, L. Otrin, J. Rauchhaus, Z. Zhao, F. L. Kyrilis, F. Hamdi, P. L. Kastritis,  
1158 R. Dimova, I. Ivanov, K. Sundmacher, *Proc. Natl. Acad. Sci. U.S.A.* **2022**, 119, e2122468119.
- 1159